Numerical Analysis of Thermally Driven Rarefied Gas Flows inside Micro Devices

Shogo Sugimoto

2023

Contents

Chapter 1

General Introduction

1.1 Historical overview

Natural convection never occurs in continuum fluids without any external force. This fact is easily understood from the Navier-Stokes equations, which implicitly assume local equilibrium. This assumption holds sufficiently well when the ratio of the mean free path of gas molecules l to the representative length of the system under consideration L, i.e. the Knudsen number l/L, is negligibly small. Rarefied gas dynamics is a field of gas dynamics which is applicable to all Knudsen numbers and has been successfully employed in a variety of fields, including space exploration and vacuum technology.

Various types of rarefied gases flows are induced by their temperature fields. Consider, for example, a rarefied gas in a channel with a uniform temperature gradient along the side wall. When the mean free path of the gas molecules is not negligibly small compared with the channel width, one-way flow in the direction of the temperature gradient, from the cold side to the hot side, is induced, and this phenomenon is referred to as thermal transpiration flow. The origin of studies on thermal transpiration flow goes back to the work of Reynolds [1]. His device was a vessel partitioned by a porous plate with one side heated. Thermal transpiration flow is induced in each porous channel because of the temperature difference and the smallness of the pore diameter of each channel, which is estimated by modern measurement techniques to be on the order of the mean free path under the atmospheric condition, i.e. $l = 10^{-7}$ m. Subsequently, Knudsen developed a simple vacuum pump making use of thermal transpiration flow [2]. His device was a single wavy channel consisting of thin pipes and thick ones connected alternatively and the every other connection points were heated. Diameters of these pipes were on the order of 10^{-3} m and, one-way flow was induced under the pressure of 10^{-3} atm (the mean free path is approximately 10^{-4} m and the Knudsen number of the gas in his apparatus is estimated as about 10^{-1}). In the late 20th century, Muntz et al. revisited thermal transpiration flow pumps using porous membranes [3, 4]. Their papers activated subsequent studies of pumping systems using thermally driven rarefied gas flows [5–26]. Although the structure of their device was almost the same as that of Reynolds [1], they named their device "Knudsen pump" after Knudsen's work. Since then, pumps using thermally driven rarefied gas flows have been referred to as Knudsen pump. Owing to the recent development of semiconductor manufacturing technology, it is

now possible to fabricate structures on the order of micro- and nanometers. The size of the flow path width in such microdevices, i.e. Micro Electro Mechanical Systems (MEMS), is nearly the same as the mean free path of gas molecules under the atmospheric condition. MEMS have been widely used to realize micro pumps in recent years [27–48].

1.2 Thermally driven rarefied gas flows

Thermally driven rarefied gas flows relevant to the dissertation are explained briefly below.

1.2.1 Thermal creep and thermal transpiration flows

Consider a rarefied gas at rest in contact with a flat wall at rest with a uniform temperature gradient. The temperature field of the gas near the wall has a similar temperature gradient. A flow is induced along the wall in the direction of the temperature gradient. This flow is called thermal creep flow. According to Sone [49], the physical mechanism of thermal creep flow is interpreted as follows. The molecules impinging on a point of the wall come from various directions. They do not experience collisions with each other over a distance on the order of the mean free path. They arrive at the point keeping their original velocities. Therefore, the average speed of molecules impinging from the hotter region is larger than that of the molecules from the colder region. Consequently, the wall receives from them some momentum in the direction opposite to the temperature gradient of the wall. In general, impinging molecules are considered to be isotropically reflected (this is called the diffuse reflection boundary condition); the reflecting molecules do not contribute to the tangential component of the momentum transfer. Therefore, the net tangential momentum transfer from the gas to the wall is in the opposite direction to that of the temperature gradient. As the reaction, the gas receives from the wall the tangential momentum in the direction of the temperature gradient. Then, the gas is accelerated in this direction and the momentum of the impinging molecules from the low-temperature side increases while that from the high-temperature side decreases. The gas velocity at the steady-state is determined such that the tangential component of the momentum transfer vanishes.

As mentioned in Sec. 1.1, thermal transpiration flow is a rarefied gas flow in a channel or pipe when there is a temperature gradient along the side wall. Then, the driving principle can be interpreted as momentum transfer between the wall surface and the gas similar to thermal creep flow. Theoretical studies on thermal creep or thermal transpiration flows have been conducted on the basis of the linearized Boltzmann equation for the idealistic case of an infinitely long flow path [50–53].

1.2.2 Thermal edge flow

Consider a rarefied gas around a flat plate at rest with a uniform temperature. Let the plate be located on the half plane ($x_2 = 0$, $x_1 < 0$). For simplicity, we assume that the temperature of the surrounding gas is uniform far from the plate but it is different from that of the plate. Because there is no temperature gradient of the plate, thermal creep flow does not occur. The gas temperature, however, varies appreciably around the edge

of the plate ($x_1 = x_2 = 0$). Then, as in thermal creep flow described in Sec. 1.2.1, the tangential momentum transfer around the edge induces a gas flow in the x_1 direction when the surrounding gas temperature is higher than that of the plate and vice versa. This flow is called thermal edge flow. Thermal edge flow is predicted numerically first in [54] and it is also observed in experiments [55–57].

1.2.3 Flows induced by non-uniformity of accommodation coefficient

In Secs. 1.2.1 and 1.2.2, we assume that the impinging molecules reflect isotropically. The diffuse reflection is one of isotropic reflection rules. The Maxwell-type boundary condition is a generalizations of the diffuse reflection [58]; molecules are diffusely reflected at a rate of the accommodation coefficient α, and the rest, $1 - \alpha$, are reflected specularly (specular reflection), i.e. in perfect elasticity. Only the diffusely reflected molecules contribute to the momentum transfer in the tangential direction. The magnitude of thermal transpiration flow depends on α, but, it does not necessarily decrease with decrease in α [51].

In the above explanation, the accommodation coefficient α is considered to be uniform. On the other hands, there is a possibility that rarefied gas flows could be induced due to non-uniformity of α. In fact, some researchers claim that the well-known Crookes radiometer [59], the impeller rotation of which was explained by Maxwell as the consequence of the occurrence of thermal creep flow [58], could be due to a flow induced by the difference between accommodation coefficients on both sides of the impeller; the impeller is too thin to keep the temperature difference between the two sides of the impeller [60]. The next example is Hobson's accommodation pump [61–64]; a gas flows from the part with low accommodation coefficient to that with high accommodation coefficient under the highly rarefied condition, which is achieved, for example, in a cryogenic environment using liquid nitrogen. The last example is prominent and is known as Ratchet pump in MEMS community [65]. It consists of two facing surfaces with different uniform temperatures. Each surface has a zigzag structure with the variation of accommodation coefficient synchronous to the structure. It has been shown numerically that one-way flow is induced between the two surfaces.

1.3 Organization of the dissertation

The dissertation is written on the basis of the author's three published papers [66–68]. Its organization is as follows. Chapter 2 is based on [66]. We report there that devices using thermal transpiration flow, called the Knudsen pump, can be classified into two main categories, Knudsen-type pump [2] (hereafter, this type is referred to as "KP") and Reynolds-type pump [1] (hereafter, this type is referred to as "RP"), according to their driving mechanisms. We discuss the difference of mechanism between these types and compare their performances, which reveals the essential role of thermal edge flow in RP. Chapter 3 is based on [67]. This chapter presents a numerical analysis of an actual MEMS RP. Currently, the performance of MEMS pump is estimated by some empirical formulas. We perform the numerical analysis on the basis of the Boltzmann equation, which is the governing equation of rarefied gas flows. This is the first example of the orthodox theoretical prediction of performance estimation

for actual MEMS devices. Chapter 4 is based on [68]. We consider a rarefied gas between two parallel flat plates with different constant temperatures. We confirm the occurrence of one-way flow in the case of non-uniform distributions of accommodation coefficient. The dissertation reports findings that are expected to lead innovative improvements in microdevice pumping systems.

Chapter 2

Driving mechanism of thermally driven rarefied gas flow pumps [66]

2.1 Introduction

This chapter discusses the basic properties of thermally driven rarefied gas flow pumps. We claim that KP and RP should be categorized into different groups since the mechanisms of these two pumps are different, which is shown in this chapter.

KP is a single channel consisting of pipes of two (or more) different diameters, and it is heated at every other connection point. Figure 2.1 (a) is the schematic of one unit of KP. The diameters of these pipes are on the order of the mean free path of low-pressure gas molecules. The mechanism of KP is roughly explained as follows. Around each heated connection point, two thermal transpiration flows in mutually opposite directions are induced. Because of the collision of these flows, the pressure rises there. This causes two Poiseuille flows in mutually opposite directions. The occurrence of the one-way flow in the channel is understood as the composition of these thermally- and pressure-driven flows. Similar to thermal transpiration flow, Poiseuille flow has also been analyzed on the basis of the linearized Boltzmann equation. The data of the flow rates of these flows for various Knudsen numbers are now available, and the performance of KP is sometimes estimated using these data (see Sec. 2.4.1 for details). KP has also been analyzed directly on the basis of the nonlinear Boltzmann equation [5–17]. As for the experimentally studies, see e.g. [21, 23–26].

RP is a single vessel separated by a porous plate, which has numerous porous channels. One side of the porous plate is heated. The schematic of RP is depicted in Fig. 2.1 (b). At the atmospheric condition, the mean free path of the gas molecules is on the same order of pore size; the diameter of a representative porous channel is about 10^{-7} m. Thermal transpiration flow is induced in each porous channel in the direction of the temperature gradient. The diameter of the vessel, which is usually a few centimeters, is enormously larger than the mean free path. Therefore the Knudsen number based on the diameter of the vessel is about 10^{-5} at the atmospheric condition. Thermal transpiration flow due to the temperature gradient of the wall of the vessel is negligibly small because of the smallness of the Knudsen number (Kn); it is known that the magnitude of thermal transpiration flow for small Kn is proportional to Kn.

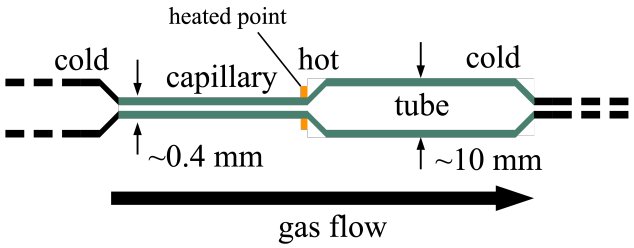

(a)

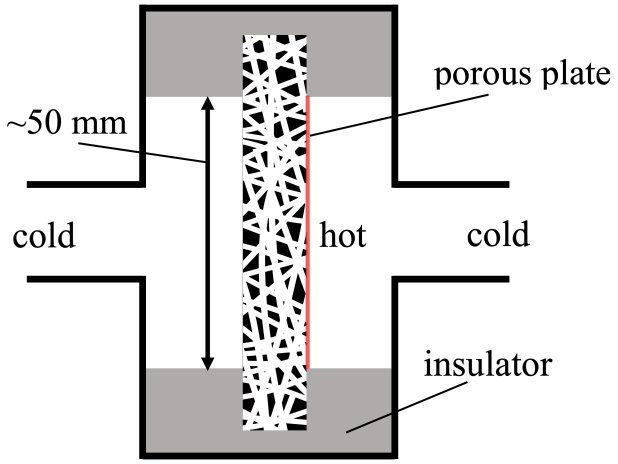

(b)

Figure 2.1: Schematic of two types of thermally driven rarefied gas flow pump. (a) KP [2] and (b) RP [1]. The wall of one unit of KP is rimmed with green. The surface of porous plate represented by the red line is heated.

2.2 Models of pumps

2.2.1 Model of KP

As mentioned previously, the structure of KP is periodic. We consider a 2D model of KP, the one unit of which is depicted in Fig. 2.2, and investigate a rarefied gas flow induced there. This model is identical to that studied in [5]. The one unit consists of two channels P and N connected with each other and is aligned in the X_1 direction. The length of the channel P and that of the channel N in the X_1 direction are denoted by L and D, respectively. The width of the channel P and that of the channel N are W and $2W$, respectively. The channel P represents the capillary in Fig. 2.1 (a), and the channel N does the tube. The one unit has two openings ($X_1 = 0,\ |X_2| < W/2$) and ($X_1 = L + D,\ |X_2| < W/2$). The distribution of the wall temperature $T_w(X_1)$ is given as a linear function of X_1 which is depicted in Fig. 2.2; as X_1 increases, T_w increases linearly in $0 < X_1 < L$ (channel P) and decreases linearly in $L < X_1 < L + D$ (channel N); $T_w(0) = T_w(L + D) = T_0$ and $T_w(L) = 3T_0$, where T_0 is a constant. There is no temperature jump along a wall of KP.

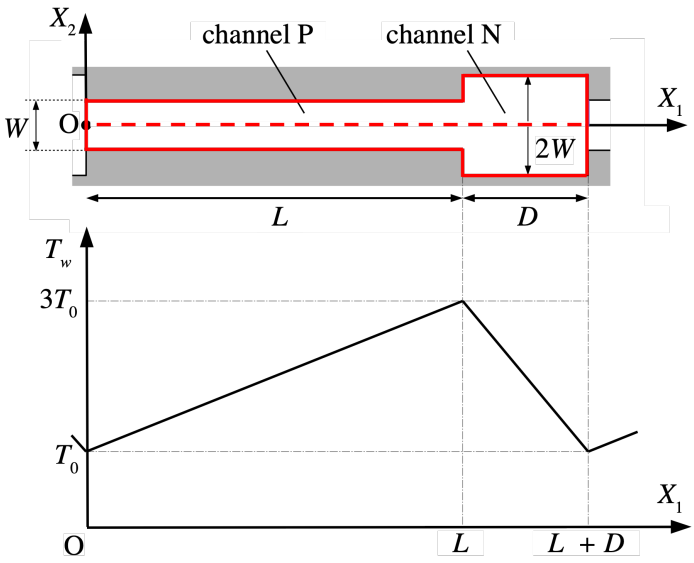

Figure 2.2: One unit of KP [5]. One unit of KP is rimmed by solid red lines and a dashed red line (symmetry axis).

2.2.2 Models of RP

When RP is produced as MEMS, the porous plate is replaced by a quasi-periodic structure made by parallely connecting parts of a relatively simple structure, each of which will be hereafter called MEMS channel. We will hereafter call the integrated structure as MEMS plate. Although the flow rate of such a RP can be increased by increasing the number of MEMS channels, the pressure difference does not increase and it is insufficient for practical use except for special cases. It seems natural to connect such RPs in cascade. Then, we consider a simple cascade RP made by inserting multiple MEMS plates at an equal spacing inside a vessel, the schematic of which is depicted in Fig. 2.3. We will hereafter refer the part of the cascade RP from a MEMS plate to one of the consecutive ones as its one unit (see Fig. 2.3).

Let us consider one unit of a cascade RP and let the number of MEMS channels in the MEMS plate be N. The empty space of the one unit can be divided into N sub empty space such that each part is respectively associated with each MEMS channel. A MEMS channel and its associated sub empty space constitute a part of the one unit, which will be hereafter called "element". Therefore, the one unit of RP consists of N elements and the corresponding part of the vessel. For $N \gg 1$, we assume that the influence of the vessel can be ignored and one unit can be treated as a periodic structure. One MEMS channel and one element are also shown in Fig. 2.3.

We consider three models of cascade RP. One element is depicted for each model together with its neighborhood in Figs. 2.4 (a) - (c). We will hereafter call the model depicted in Fig. 2.4 (m) model (m) (m = a, b, c). Models (a) and (b) are for 2D and model (c) is for 3D. Models (a) and (b) are periodic with respect to X_2 and model (c) is periodic with respect to X_3 as well. The gray color rectangles in these schematics represent solid walls. and the region surrounded by red solid lines represents one element. They are symmetric with respect to

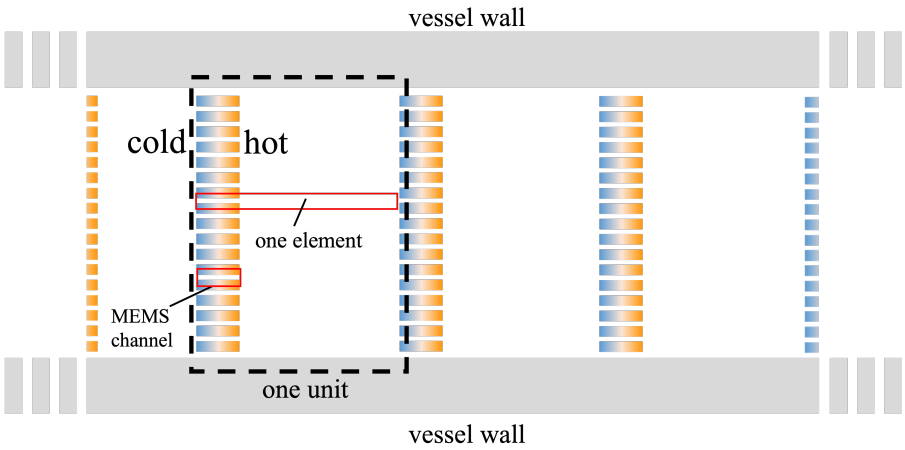

Figure 2.3: Schematic of a simple cascade RP. The black dashed rectangle represents its one unit.

the X_1 axis. One element of model (c) has two planes of symmetry, $X_2 = 0$ and $X_3 = 0$. A quarter of one element of model (c) and its neighborhood are shown in Fig. 2.4 (c).

Model (a) consists of two parts, part P ($0 < X_1 < L$) and part N ($L < X_1 < L + D$). Part P corresponds to a MEMS channel, and Part N does to the associated sub empty space. The wall temperature T_w in part P is given by

$$T_w\left(X_1\right) = \left(1 + 2\frac{X_1}{L}\right) T_0 \qquad (0 \leq X_1 \leq L)\,; \tag{2.1}$$

the temperature of the side wall at $X_1 = 0$ is T_0, and that of the side wall at $X_1 = L$ is $3T_0$. Here, T_0 is the wall temperature of the vessel. In model (a), the channel width of the MEMS channel is W and the width of the sub empty space is $2W$. In model (b), the MEMS channel consists of squares of side W and the width of the sub empty space is $2W$. Model (c) consists of rectangular bodies with a square cross section of side W, and the width and height of the sub empty space is $2W$. The wall temperature distributions in models (b) and (c) are also given by Eq. (2.1).

2.3 Basic Equation and boundary conditions

The velocity distribution function of gas molecules $f\left(t, \boldsymbol{X}, \boldsymbol{\xi}\right)$, where t is the time, $\boldsymbol{X}$ is the position vector, and $\boldsymbol{\xi}$ is the molecular velocity, is governed by the Boltzmann equation:

$$\frac{\partial f}{\partial t} + \boldsymbol{\xi} \cdot \frac{\partial f}{\partial \boldsymbol{X}} = J\left[f\right]. \tag{2.2}$$

The $J[f]$ is the collision term and is defined by

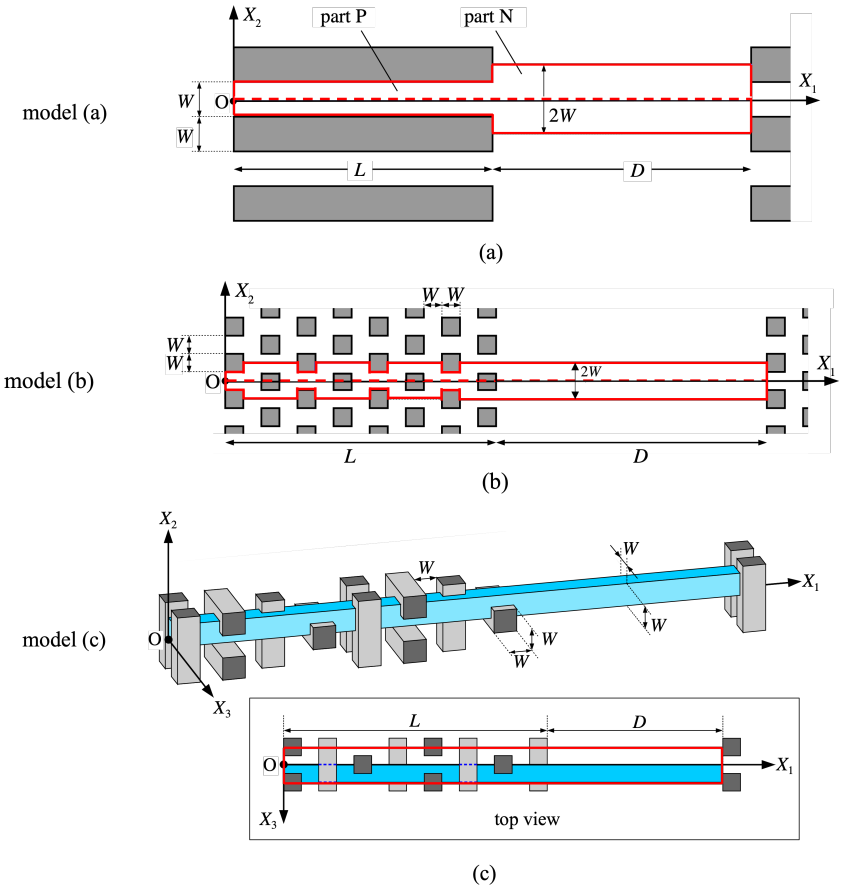

Figure 2.4: Numerical models of the cascade RP. (a) 2D model with straight channels. (b) 2D model with complex geometry. (c) 3D model with complex geometry. One element of model (a) and that of (b) are rimmed by solid red lines. A quarter of one element of model (c) together with its neighborhood is depicted; one element of model (c) is rimmed by solid red line (top view). The planes that are part of the boundaries of the element are drawn in blue. In (a) to (c), the objects drawn on the right end of one element are a part of the next unit.

$$
\begin{aligned}
J[f] = \int_{|\boldsymbol{\zeta}|<\infty,\,|\boldsymbol{\alpha}|=1} & \left[f(\boldsymbol{\xi}')\, f(\boldsymbol{\zeta}') - f(\boldsymbol{\xi})\, f(\boldsymbol{\zeta})\right] \\
& \times \left(\frac{d_m^2}{2}\,|\boldsymbol{V}\cdot\boldsymbol{k}|\right) \mathrm{d}\Omega(\boldsymbol{k})\,\mathrm{d}\boldsymbol{\zeta}, \qquad (2.3) \\
\boldsymbol{V} = \boldsymbol{\zeta} - \boldsymbol{\xi}, \quad & \boldsymbol{\xi}' = \boldsymbol{\xi} + (\boldsymbol{V}\cdot\boldsymbol{k})\,\boldsymbol{k}, \quad \boldsymbol{\zeta}' = \boldsymbol{\zeta} - (\boldsymbol{V}\cdot\boldsymbol{k})\,\boldsymbol{k},
\end{aligned}
$$

for hard sphere molecules, where d_m is the diameter of a molecule and $\mathrm{d}\Omega(\boldsymbol{k})$ is the solid angle element in the direction of the unit vector $\boldsymbol{k}$. The domain of the integration with respect to the vector $\boldsymbol{\zeta}$ (and that of integration with respect to $\boldsymbol{\xi}$, unless otherwise stated) is the whole velocity space, i.e. $\mathbb{R}^3$, and that with respect to $\boldsymbol{k}$ is all directions. We omit the external force term of the Boltzmann equation taking account to the fact that the size

of MEMS pumps is on the order of micrometers and the corresponding Froude number, inverse of which gives the magnitude of the external force, is very large at the Earth surface condition, i.e. Froude number is around 10^3.

The number density of molecules n, the flow velocity $\boldsymbol{v}$, and the temperature T of the gas are defined as the moments of f:

$$n\left(t,\,\boldsymbol{X}\right)=\int_{|\boldsymbol{\xi}|<\infty}f\left(t,\,\boldsymbol{X},\,\boldsymbol{\xi}\right)\mathrm{d}\boldsymbol{\xi}, \tag{2.4a}$$

$$n\boldsymbol{v}\left(t,\,\boldsymbol{X}\right)=\int_{|\boldsymbol{\xi}|<\infty}\boldsymbol{\xi}f\left(t,\,\boldsymbol{X},\,\boldsymbol{\xi}\right)\mathrm{d}\boldsymbol{\xi}, \tag{2.4b}$$

$$\frac{3}{2}\kappa nT\left(t,\,\boldsymbol{X}\right)=\int_{|\boldsymbol{\xi}|<\infty}\frac{m}{2}\left|\boldsymbol{\xi}-\boldsymbol{v}\right|^2 f\left(t,\,\boldsymbol{X},\,\boldsymbol{\xi}\right)\mathrm{d}\boldsymbol{\xi}, \tag{2.4c}$$

where κ is the Boltzmann constant, and m is the mass of a molecule. The pressure p of the gas is defined by

$$p=\kappa nT. \tag{2.5}$$

In analyses of the Boltzmann equation for flows around solid bodies, the velocity distribution of reflecting molecules at solid walls is needed. For example, the Maxwell-type boundary condition at a solid wall [58] gives the velocity distribution of reflecting molecules. Solid walls considered here are at rest and the Maxwell-type boundary condition is expressed as

$$\begin{aligned} f\left(\boldsymbol{X}_w,\,\boldsymbol{\xi}\cdot\boldsymbol{n}_w>0\right)=&\left(1-\alpha\right)f\left(\boldsymbol{\xi}-2\left(\boldsymbol{\xi}\cdot\boldsymbol{n}_w\right)\boldsymbol{n}_w\right)\\ &+\alpha\frac{\sigma_w}{\left(2\pi\kappa T_w/m\right)^{3/2}}\exp\left(-\frac{\left|\boldsymbol{\xi}\right|^2}{2\kappa T_w/m}\right), \end{aligned} \tag{2.6a}$$

$$\sigma_w\left(\boldsymbol{X}_w,\,T_w\right)=-\left(\frac{2\pi m}{\kappa T_w}\right)^{1/2}\int_{\boldsymbol{\zeta}\cdot\boldsymbol{n}_{\boldsymbol{w}}<0}\left(\boldsymbol{\zeta}\cdot\boldsymbol{n}_w\right)f\left(\boldsymbol{X}_w,\,\boldsymbol{\zeta}\right)\mathrm{d}\boldsymbol{\zeta}, \tag{2.6b}$$

$$f_e\left(\boldsymbol{\xi}\right)=\frac{\sigma_w}{\left(2\pi\kappa T_w/m\right)^{3/2}}\exp\left(-\frac{\left|\boldsymbol{\xi}\right|^2}{2\kappa T_w/m}\right), \tag{2.6c}$$

where $\boldsymbol{X}_w$ is the position of a solid wall; T_w, α, and $\boldsymbol{n}_{\boldsymbol{w}}$, respectively, are the wall temperature, the accommodation coefficient, and the unit normal vector of the wall pointing toward the gas region at $\boldsymbol{X}=\boldsymbol{X}_w$. Owing to Eq. (2.6b), the basic property of solid wall that there is no mass flow through it, i.e. $\boldsymbol{v}\cdot\boldsymbol{n}_{\boldsymbol{w}}=0$, is automatically satisfied. The Maxwell-type boundary condition for $\alpha=1$ and that for $\alpha=0$ correspond to the diffuse reflection and the specular reflection, respectively. In the case of the specular reflection, the velocity distribution of the reflecting molecule is determined only by the velocity distribution of the impinging molecule. In the case of the diffuse reflection, the velocity distribution of the reflecting molecules is given as the corresponding part of the Maxwell distribution for $T=T_w$ and $\boldsymbol{v}=0$, and the information of the impinging molecules is given through σ_w.

On a plane of symmetry, we can use Eq. (2.6a) with $\alpha=0$, i.e. the specular reflection. When f has a periodicity with interval H in the X_1 direction, the following periodic condition

holds:

$$f\left(t,\, X_1,\, X_2,\, X_3,\, \xi_1,\, \xi_2,\, \xi_3\right) = f\left(t,\, X_1 + H,\, X_2,\, X_3,\, \xi_1,\, \xi_2,\, \xi_3\right). \tag{2.7}$$

Besides Maxwell-type boundary condition including the specular reflection condition, the periodic condition [Eq. (2.7)] will be also employed in the numerical computation.

2.3.1 Numerical method

We solve the Boltzmann equation [Eq. (2.2)] numerically by the DSMC method [69]. The DSMC method pursues the motion of many particles, each of which represents a fixed number of real molecules with a common velocity. Their motions are computed for every time step Δt in two steps. The first step, the free flow step, changes only the position of each particle according to its translational motion, and it corresponds to Eq. (2.2) without $J[f]$. The second step, the collision step, changes only the velocities of some of the particles and this step corresponds to Eq. (2.2) without $\boldsymbol{\xi} \cdot \dfrac{\partial f}{\partial \boldsymbol{X}}$. For this step, the computational domain is divided into small cells. The velocities of particles in each cell are changed in the following way. Let N be the number of particles in a cell. There are $N(N-1)/2$ particle pairs. Each pair of particles is selected as a collision pair with a probability corresponding to $J[f]$, which depends on the magnitude of their relative speed, the time step Δt, and d_m^2. The velocities of the particles of selected pairs are stochastically changed according to the law of binary collision (hard-spheres). Those of non-selected pair are left unchanged. Although the computational cost of the collision step is proportional to N^2, it can be reduced to order N by using the so called null collision method [70] or no time counter method [69], which is utilized in this study. The boundary condition is treated in the first step; the computation of the specular reflection of particles is literal and obvious. The diffuse reflection boundary condition is treated as an isotropic scattering; the direction $\boldsymbol{s}$ of the velocity of a reflecting particle is randomly chosen from the domain of $\boldsymbol{n_w} \cdot \boldsymbol{s} > 0$ and its speed is stochastically determined according to the probability distribution corresponding to f_w of Eq. (2.6a). In the case of the Maxwell-type boundary condition, an impinging particle is reflected whether diffusely or specularly, and the accommodation coefficient α there gives the probability of the diffuse reflection. For the details of the computation of DSMC, see e.g. [69].

It is proved mathematically that numerical solution of DSMC converges to solution of the Boltzmann equation in the limit of infinitely large number of particles and vanishingly small time step and cell size [71]. In actual computations, however, we are urged to use limited number of particles (and time step and cell size are not infinitesimally small). Results of such computations are inevitably accompanied by appreciable magnitude of statistical fluctuations. In the case of steady problem, time average of many snapshots is represented as the final result. This procedure is for the reduction of statistical fluctuations. It is empirically justified, although it is out of the above mentioned rigorous mathematical proof. DSMC computation should be done with the time step smaller than the local mean free time, and the cell size smaller than the local mean free path. These restrictions become severe for small Knudsen numbers. Furthermore, in this case, the distribution function is very close to the local Maxwell distribution, and the computation needs more accuracy to capture the small deviation.

DSMC computation for hard sphere molecules requires the explicit size of d_m, which is given in the following way. We first specified the value of the Knudsen number of the system under consideration $\mathrm{Kn} = l_0/W$, where l_0 is the mean free path of gas molecules at the reference equilibrium state and W is the reference length of the system. The mean free path ℓ_0 at the equilibrium state at rest with the number density n_0 and the temperature T_0 is given by

$$\ell_0 = \frac{1}{\sqrt{2}\pi n_0 d_m^2}, \tag{2.8}$$

for hard sphere molecules; the mean free path for hard sphere molecular is independent of the temperature T_0. On the other hand, viscosity μ at $n = n_0$ and $T = T_0$ is given by:

$$\mu = \frac{\sqrt{\pi}}{2}\Gamma_1 p_0 \left(\frac{2\kappa T_0}{m}\right)^{-1/2} l_0, \tag{2.9}$$

where p_0 is

$$p_0 = \kappa n_0 T_0, \tag{2.10}$$

and Γ_1 is a constant about 1.27 (see e.g. [49]). Incidentally, for BGK equation, $\Gamma_1 = 1$. The size of d_m is determined from Eqs. (2.8) and (2.9).

The reference time t_0 is defined by

$$t_0 = \frac{W}{(2\kappa T_0/m)^{1/2}}. \tag{2.11}$$

The uniform equilibrium state at rest

$$f(t=0) = \frac{n_0}{(2\pi\kappa T_0/m)^{2/3}} \exp\left(-\frac{|\boldsymbol{\xi}|^2}{2\kappa T_0/m}\right), \tag{2.12}$$

with the number density n_0 and the temperature T_0 is commonly employed as the initial condition of DSMC in all chapters.

Let V_0 be the volume of the entire computational domain. There are $V_0 n_0$ molecules at $t = 0$. When these molecules are represented by N_0 particles, each particle represent $\Delta = V n_0/N_0$ molecules. Each macroscopic quantity is computed in each cell. The cell system for the computation of macroscopic quantities is not necessarily the same as the cell system used for the collision step, but the same cell system is used in this study. Consider N particles in a cell of volume V. Let the velocities of these particles be $\boldsymbol{\xi}^{(k)}$ ($k = 1, 2, ..., N$). Then, the number density n, the flow velocity $\boldsymbol{v}$, and the temperature T at a representative point of the cell are given by

$$n = \frac{N\Delta}{V}, \tag{2.13a}$$

$$\boldsymbol{v} = \frac{1}{N}\sum_{k=1}^{N} \boldsymbol{\xi}^{(k)}, \tag{2.13b}$$

$$\frac{3}{2}\kappa T = \frac{1}{N}\sum_{k=1}^{N} \left|\boldsymbol{\xi}^{(k)} - \boldsymbol{v}\right|^2. \tag{2.13c}$$

The mass flux $mn\boldsymbol{v}$ is computed from Eqs. (2.13a) and (2.13b).

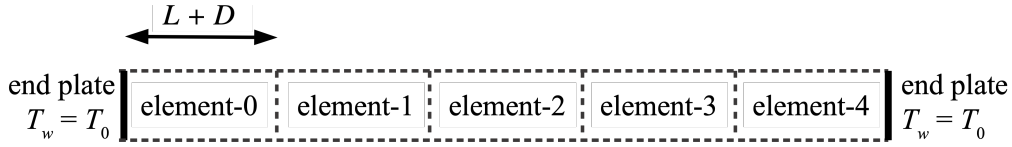

Figure 2.5: System of numerical model used to investigate maximum compression ratio. Five elements are cascade-connected in X_1 directions.

2.4 Problem setting

The maximum flow rate q_{max} and the maximum compression ratio γ_{max} are the key indicators of pump performance. In [5], q_{max} of a KP is determined by the DSMC computation for one unit with periodic boundary condition in the X_1 direction [see Fig. 2.2]. The γ_{max} of the KP is determined by the DSMC computation for a cascade pump with multi-units, the both ends of which are sealed by solid walls. For each unit, average local Knudsen number $\mathrm{Kn}_{\mathrm{loc}}$ and compression ratio are obtained. By carrying out for various initial data, the data of γ_{max} for wide range of $\mathrm{Kn}_{\mathrm{loc}}$ are obtained. The curve $\gamma_{max}\,(\mathrm{Kn}_{\mathrm{loc}})$ for 5-units and that for 10-units have a common part, which is considered to be a part of a universal function independent of the number of unit. It is expected that the domain of definition of the universal function spreads as the number of units increases. The data of $\gamma_{max}\,(\mathrm{Kn}_{\mathrm{loc}})$ so obtained are expected to be employed in the estimate of compression ratio of the corresponding KP with arbitrary number of units.

We compute q_{max} and γ_{max} for RP in the same way as in [5] and compare its performance with that of KP. In order to obtain the data of q_{max}, the computation is carried out for one element with periodic condition in the X_1 direction in addition to the X_2 direction (and in the X_3 direction in model (c)). The data of γ_{max} are obtained for model (a). Its computations are performed for five elements connected in cascade. The boundary condition at both ends are the diffuse reflection which corresponds to sealing walls [see Fig. 2.5]. The symmetries of models (a) - (b) with respect to X_2, and X_3 for (c), are also taken into account.

2.4.1 Rough estimate of q_{max} of KP

The direction and magnitude of one-way flows generated in a KP depend on various parameters, such as the ratio of the lengths of the pipes and the magnitude of temperature gradients. As mentioned previously, thermal transpiration and Poiseuille flows have been studied on the basis of the linearized Boltzmann equation and its model equations. Owing to these studies, the numerical data of the mass flux for various Knudsen numbers are now available for both flows. Here we introduce a rough estimate of the q_{max} of KP making use of these data. Although these data are for flows induced between two parallel plates of infinite length, they are employed for a channel of finite length. Consider the model shape of KP shown in Fig. 2.2. Suppose that the narrow and wide channels are periodically connected. For the sake of the application of the linearized theory, the temperature of the hot section is expressed as $T_0 + \Delta T$ instead of $3T_0$. The rough estimate is based on the following scenario. From the periodic condition, both ends of the unit are at the same pressure. The direction of the temperature gradient is opposite in the narrow and wide channels, and thermal transpi-

ration flow occurs in the direction toward the heated point in each. The pressure around the heated point increases due to the collision of the two thermal transpiration flows in mutually opposite directions. Then, in each channel, two Poiseuille flows in the mutually opposite directions are generated. If the pressure difference between two consecutive connecting points Δp are known, these Poiseuille flows are uniquely determined. A one-way flow is assumed to be realized as the combination of the above four flows. The Δp is determined from the continuity of mass flow rate. Note that the above scenario is based on the assumption that the flow is one-dimensional, $L/W \gg 1$, and ΔT is small. For 2D channels, the mass flow rate Q per unit length in X_3 direction for a very long channel of width d is given by [72–74].

$$\begin{aligned}\frac{Q}{\rho_0 c_0 d} &= \Delta p Q_P + \Delta T Q_T \\ &= \left(\frac{d}{p_0}\frac{\mathrm{d}p}{\mathrm{d}X_1}\right) Q_P\left(\frac{\ell_0}{d}\right) + \left(\frac{d}{T_0}\frac{\mathrm{d}T}{\mathrm{d}X_1}\right) Q_T\left(\frac{\ell_0}{d}\right),\end{aligned} \tag{2.14}$$

where p and T are consider to be functions of X_1 and ρ_0 and c_0 are, respectively, the reference density and the thermal speed of the molecule defined by

$$\rho_0 = m n_0, \tag{2.15}$$

$$c_0 = \left(2\kappa T_0/m\right)^{1/2}. \tag{2.16}$$

As mentioned previously, Q_P and Q_T are non-dimensional functions corresponding to the Poiseuille flow and the thermal transpiration flow, respectively [53, 75]. Then, the mass flow rate Q in the P part, i.e. $d = W$ (see Fig. 2.2) is given by

$$\begin{aligned}\frac{Q}{\rho_0 c_0 W} &= \frac{W}{p_0}\frac{\Delta p}{L} Q_P\left(\frac{\ell_0}{W}\right) + \frac{W}{T_0}\frac{\Delta T}{L} Q_T\left(\frac{\ell_0}{W}\right), \\ \Delta p &= p(L) - p(0), \quad \Delta T = T(L) - T(0).\end{aligned} \tag{2.17}$$

The Q in the N part (see Fig. 2.2),

$$\frac{Q}{\rho_0 c_0 W} = -4\frac{W}{p_0}\frac{\Delta p}{D} Q_P\left(\frac{\ell_0}{2W}\right) - 4\frac{W}{T_0}\frac{\Delta T}{D} Q_T\left(\frac{\ell_0}{2W}\right), \tag{2.18}$$

due to $d = 2W$ and periodic conditions $p(L + D) = p(0)$ and $T(L + D) = T(0)$. Equating Q in Eqs. (2.17) and that in (2.18), we can determine Δp or eliminate it. Finally, we have

$$\begin{aligned}\frac{Q}{\rho_0 c_0 W} &= \frac{r_T - r_P}{1 + (D/4L)\, r_P}\frac{W}{L}\frac{\Delta T}{T_0} Q_T\left(\frac{\ell_0}{2W}\right), \\ r_T &= \frac{Q_T(\ell_0/W)}{Q_T(\ell_0/2W)}, \quad r_P = \frac{Q_P(\ell_0/W)}{Q_P(\ell_0/2W)}.\end{aligned}$$

The maximum mass flux $q_{\max}$ is given by

$$q_{\max} = Q/S_{\max},$$

where $S_{\max} = 2W$ in the model of the present KP. Then, we obtain

$$\frac{q_{\max}}{\rho_0 c_0} = \frac{1}{2}\frac{r_T - r_P}{1 + (D/4L)\, r_P}\frac{W}{L}\frac{\Delta T}{T_0} Q_T\left(\frac{\ell_0}{2W}\right). \tag{2.19}$$

The data for Q_p and Q_T are obtained for infinitely long channels and its temperature gradient is very small. Whereas, the length of the channels of KP is finite and the temperature difference ΔT is not so small. Furthermore, the sudden change in the cross-sectional area is not taken into account. Therefore, the above estimate should be used with caution.

2.5 Results

2.5.1 Computational parameter and post-processing

The computational parameters of the standard DSMC computations in the present study are summarized as follows. The cell size is $(\Delta X_1,\, \Delta X_2) = (0.25W, 0.125W)$ for the KP model depicted in Fig. 2.2 and the RP models (a) and (b) depicted in Fig. 2.4, and $(\Delta X_1,\, \Delta X_2,\, \Delta X_3) = (0.5W, 0.25W, 0.25W)$ for model (c) depicted there. The number of particles per cell is 2000. The time-step Δt is $0.001 t_0$ [see Eq. (2.11)]. Since the mean collision time t_m is given by

$$t_m = \frac{l_0}{(2\kappa T_0/m)^{1/2}},$$

the time step Δt is expressed as

$$\Delta t = 0.001\frac{t_m}{\mathrm{Kn}}.$$

As mentioned earlier, the time step Δt must satisfy the condition $\Delta t < t_m$. This condition is satisfied since all the computations in the present study are for $\mathrm{Kn} > 0.01$.

The flow filed is judged to be at the steady state in the following way. In each time step j, a volume-averaged of mass flow rate $q\,(j)$ are computed. Its time average for a_0 successive time steps are monitored as $\tilde{q}\,(n)$, $(n = 0,\, 1,\, 2, ...)$, and we calculate $\tilde{q}_{ave}\,(m)$ as the average of b_0 successive $\tilde{q}\,(n)$, i.e.

$$\tilde{q}\,(n) = \frac{1}{a_0}\sum_{j=0}^{a_0-1} q\,(a_0\,(n-1) + j)\,, \tag{2.20}$$

$$\tilde{q}_{ave}\,(m) = \frac{1}{b_0}\sum_{k=0}^{b_0-1} \tilde{q}\,(b_0\,(m-1) + k)\,. \tag{2.21}$$

When the deviations of $|\tilde{q}\,(b_0\,(m_0 - 1) + k) - \tilde{q}_{ave}\,(m_0)|$, $(k = 0,\, 1,\, ...,\, b_0 - 1)$ are within 5% of $|\tilde{q}_{ave}|$, the steady state is judged to be achieved and $q_{ave}\,(m_0)$ is adopted as the final result q_{max}. For computations of q_{max}, we use $(a_0,\, b_0) = (10000,\, 10)$. This means that the values of q_{max} are obtained as the time-average of 10^5 successive snapshots. The distribution of the cross-sectional averages of the temperature and the pressure, $\bar{T}\,(X_1)$ and $\bar{p}\,(X_1)$, are computed in the same way.

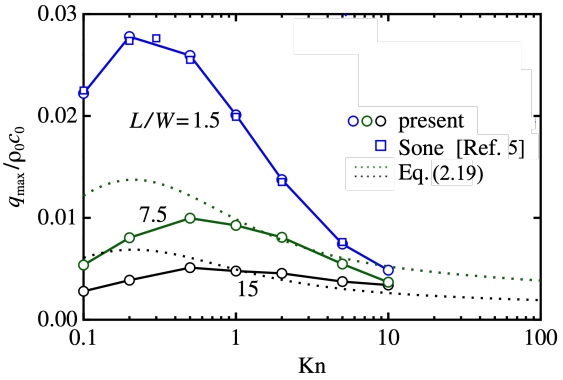

Figure 2.6: Maximum non-dimensional mass flux $q_{\max}/\rho_0 c_0$ versus the Knudsen number. For KP (Fig. 2.2) with $D/L = 1/3$. The dotted line is the rough estimate [Eq. (2.19)] with the data for the BGK equation [73].

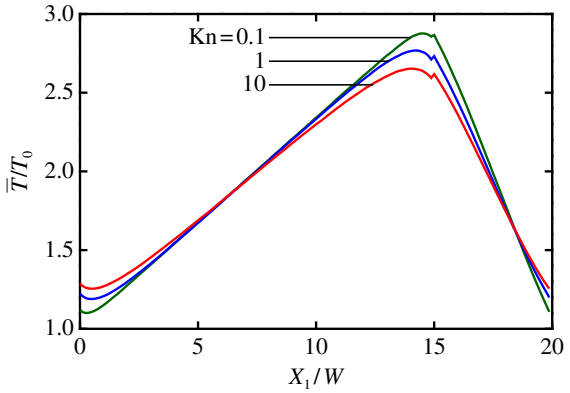

Figure 2.7: Distribution of the cross-sectional averages of the temperature $\bar{T}(X_1)$ of the KP depicted in Fig. 2.2 ($D/L = 1/3$ and $L/W = 15$.)

2.5.2 Maximum mass flux and mechanism of KP

We present the results of the KP depicted in Fig. 2.2 for $L/W = 1.5$, 7.5, and 15 ($D/L = 1/3$). The q_{max} versus Kn is plotted in Fig. 2.6; the results of [5] for $L/W = 1.5$ is also shown. The curves obtained by the rough estimate Eq. (2.19) for $L/W = 7.5$ and 15 are also shown for comparison. The q_{max} takes a maximum value at an intermediate Knudsen number (say, $\mathrm{Kn}_{\mathrm{peak}}$; i.e. $\mathrm{Kn}_{\mathrm{peak}} \sim 1$). The magnitude of one-way flow decreases as the aspect ratio L/W increases; the temperature gradient decreases accordingly. The rough estimate seems to give accurate prediction for large Kn. Figure 2.7 shows the distribution of the cross-sectional average of the temperature. The temperature distribution does not depend much on Kn. The distribution of the cross-sectional average of pressure $\bar{p}(X_1)$ is shown in Fig. 2.8. These results seem to be in accordance with the assumption of the rough estimate. Figure 2.9 shows the velocity vector of the gas for $L/W = 7.5$; the temperature field is also shown for reference. For $\mathrm{Kn} = 0.1$, a vortex-like flow is generated in the ditch, which shows the breakdown of the assumption of the rough estimate. For $\mathrm{Kn} = 10$, the flow filed looks more one-dimensional.

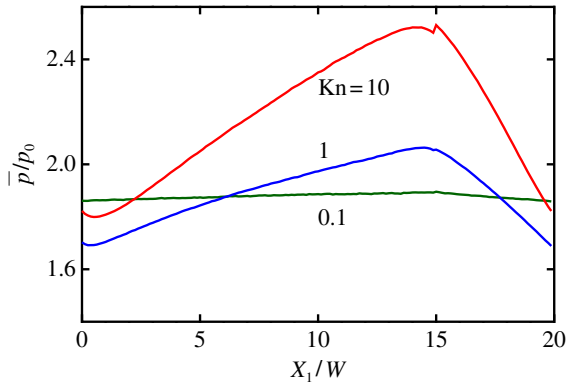

Figure 2.8: Distribution of the cross-sectional averages of the pressure $\bar{p}\,(X_1)$ of the KP depicted in Fig. 2.2 ($D/L = 1/3$ and $L/W = 15$.)

In the actual construction of a pump, the accommodation coefficient of the wall depends on the materials. The previous results are for the diffuse reflection. The results for $\alpha = 0.5$, 0.9, and 1 are shown in Fig. 2.10 ($D/L = 1/3$ and $L/W = 1.5$). It is seen from the figure that the influence of the accommodation coefficient α is appreciable for Kn < 1.

2.5.3 Results of RP

Figure 2.11 shows the variation of $q_{\max}/\rho_0 c_0$ versus Kn ($D/L = 2$, and the aspect ratio $L/W = 1.5$, 15, and 75). The $q_{\max}/\rho_0 c_0$ takes the maximum value at an intermediate value of Kn similar to the case of KP. The $\mathrm{Kn}_{\mathrm{peak}}$ increases remarkably as L/W does, which is in contrast to the case of KP. The magnitude of q_{max} is similar in magnitude to that of KP [Fig. 2.6]. Incidentally, the range of the parameter L/W is from 10 to 100 in recent MEMS RP [76]. Figure 2.12 shows the temperature field and the flow velocity vector field of RP at the steady state for Kn $= 1$, [model (a) $L/W = 15$]. The flow is meandering in the gas region and it seems to be accelerated incrementally inside the channel. The distributions of $\bar{p}\,(X_1)$ and $\bar{T}\,(X_1)$ for Kn $= 1, 10$, and 100 are shown in Fig. 2.13 and Fig. 2.14, respectively.

Next, we shows the results of the model (a) for $D/L = 20$. The value of the aspect ratio is $L/W = 15$. Figure 2.15 shows the results of $q_{\max}/\rho_0 c_0$ versus Kn, the results of $D/L = 2$ is also shown for comparison. As shown in the figure, $\mathrm{Kn}_{\mathrm{peak}}$ for $D/L = 20$ is larger than that for $D/L = 2$ and the peak value of $q_{\max}$ for $D/L = 20$ is larger than that for $D/L = 2$. Figures 2.16 and 2.17 show the distribution of the temperature $\bar{T}\,(X_1)$ and the pressure $\bar{p}\,(X_1)$ for Kn $= 1, 10$, and 100. As Kn increases, the temperature change around the hot end ($X_1/W \sim 15$) becomes more abrupt and the pressure increase there becomes more marked. This tendency is relieved as D/L increases [cf. Figs. 2.14 and 2.16].

2.5.3.1 Mechanism of RPs

As explained previously, no thermal transpiration flow is induced in the empty region. If there is only thermal transpiration flow induced in the MEMS channel, the flow rate should increase with increasing Kn [53], which is not in accordance with the numerical results. The numerical results show that the temperature change and the pressure increase around the hot

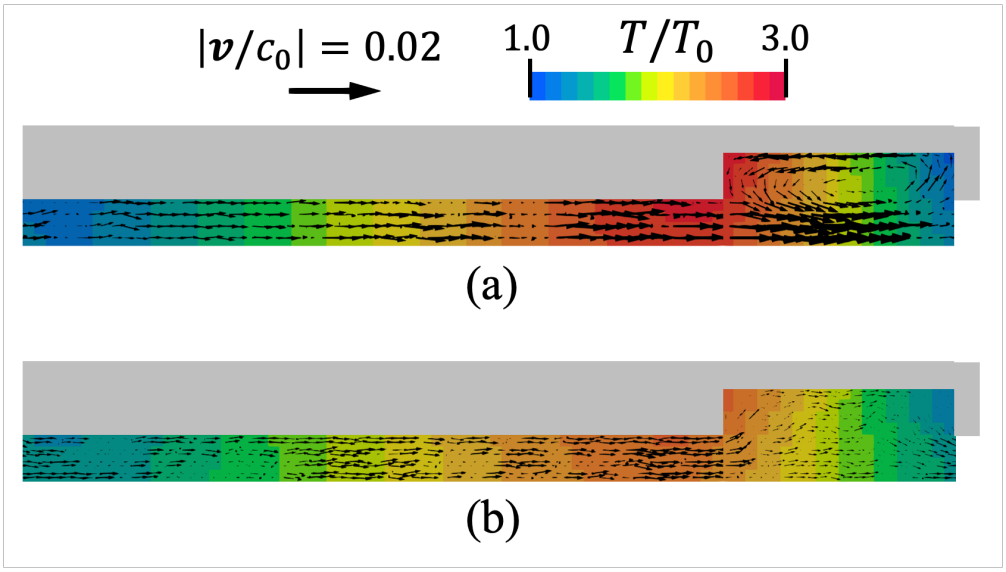

Figure 2.9: The velocity vector field and the temperature field of the KP (Fig. 2.2 for $D/L = 1/3$ and $L/W = 7.5$) at steady state for (a) : Kn $= 0.1$ and (b) : 10. The gray part represents the solid wall.

end becomes more marked as Kn increases. This tendency is relieved by the increase of D/L. This implies the occurrence of a flow in the opposite direction to the thermal transpiration flow and its magnitude increases as the temperature change around the hot end becomes more abrupt. As the mean free path (or Kn) decreases or D/L increases, the influence of molecular collision, which relieves the abrupt change of the temperature, increases. Thermal edge flow is considered as a candidate of the flow in the opposite direction; the magnitude of the thermal edge flow increases with that of the temperature change [see Sec. 1.2.2]. For this reason, we claim that the mechanism of KP is different from that of RP, i.e. the counter flow in KP is different from that of RP.

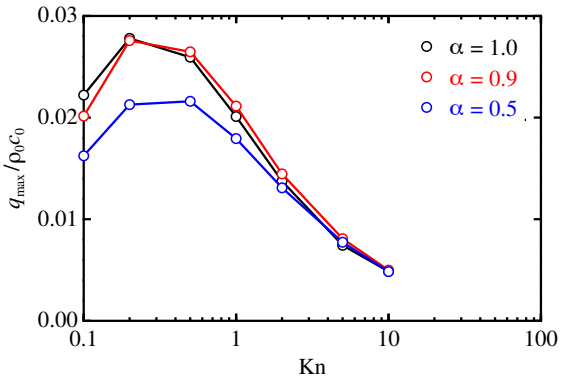

Figure 2.10: Effect of the accommodation coefficient. Non-dimensional maximum mass flux $q_{\max}/\rho_0 c_0$ versus Kn.

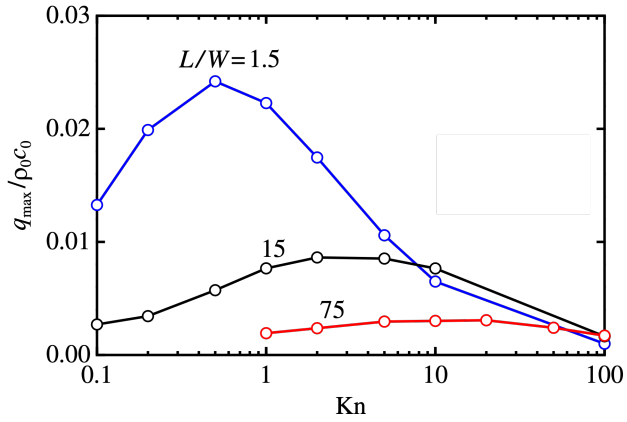

Figure 2.11: Maximum non-dimensional mass flux $q_{\max}/\rho_0 c_0$ versus Kn $= \ell_0/W$. RP [Fig. 2.4(a)] with $D/L = 2$.

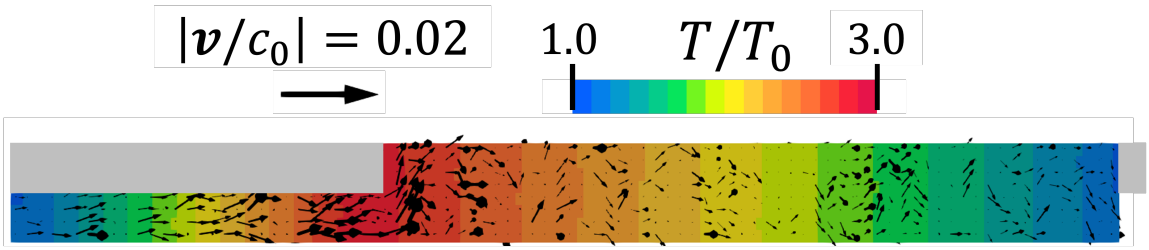

Figure 2.12: Temperature field and flow velocity vector field of RP at steady state for Kn $= 1$ [model (a) $L/W = 15$]. The gray part represents the solid wall.

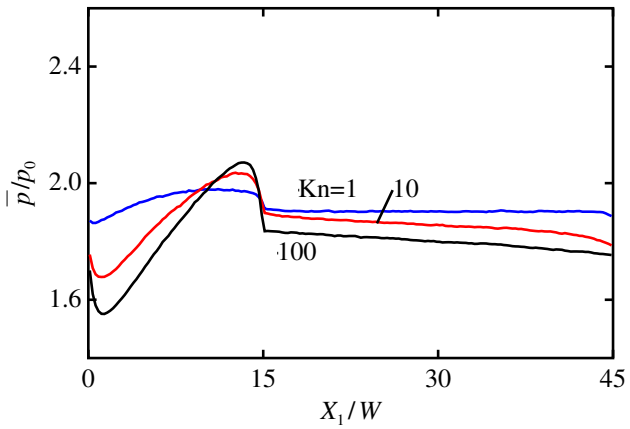

Figure 2.13: Distribution of the pressure $\bar{p}\,(X_1)$ averaged over the cross-sectional area of RP in Fig. 2.4(a) (Kn $= 1, 10$, and 100; $D/L = 2$) for $L/W = 15$.

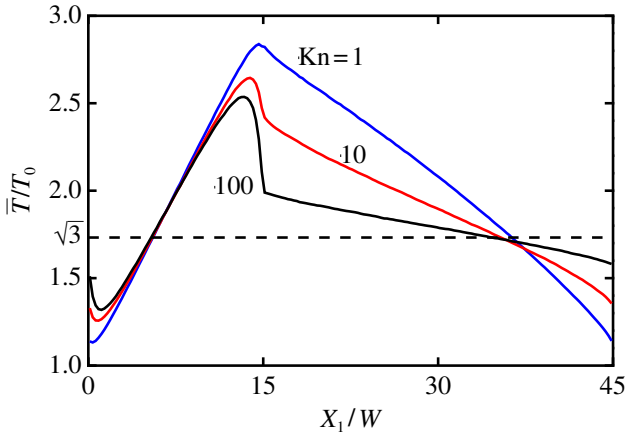

Figure 2.14: Distribution of the temperature $\bar{T}(X_1)$ averaged over the cross-sectional area of RP given in Fig. 2.4(a) (Kn $= 1, 10$, and 100; $D/L = 2$). The steady-state for $L/W = 15$.

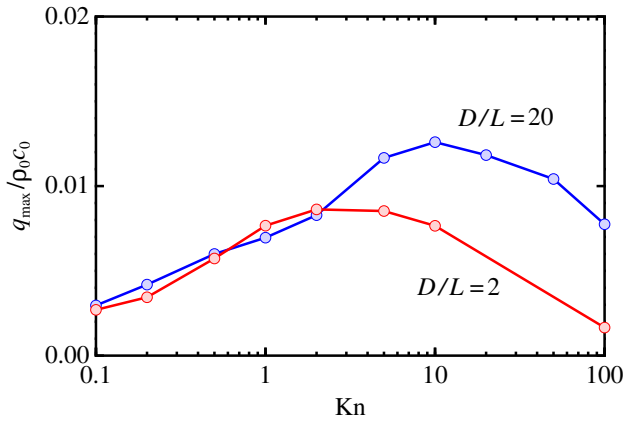

Figure 2.15: The effect of D/L for RP [Fig. 2.4(a)]. Non-dimensional maximum mass flux $q_{\max}/\rho_0 c_0$ versus the Knudsen number Kn. The case for $L/W = 15$. The results for $D/L = 20$ (blue) is compared with that for $D/L = 2$ [red, shown in Fig. 2.11].

2.5.3.2 Effect of accommodation coefficient

Figure 2.18 shows $q_{\max}/\rho_0 c_0$ versus Kn for the case of $\alpha = 0.5$, 0.9, and 1, model (a) with $D/L = 2$, $L/W = 15$. The $q_{\max}$ does not depend much on α for wide range of Kn. This tendency differs appreciably from that of KP [Fig. 2.10]. Further discussion requires to the information of dependance of thermal edge flow on α, which is not studied in the dissertation.

2.5.3.3 Effect of channel shape

A part of the experiments of RP makes use of polymer or inorganic membranes. The pore shape in these membranes is not a simple straight channel as shown in Fig. 2.4 (a). We show the numerical results for models (b) and (c) ($L/W = 15$; $D/L = 2$ and $\alpha = 1$). The distributions of cross-sectional average of the temperature $\bar{T}(X_1)$ and that of pressure $\bar{p}(X_1)$

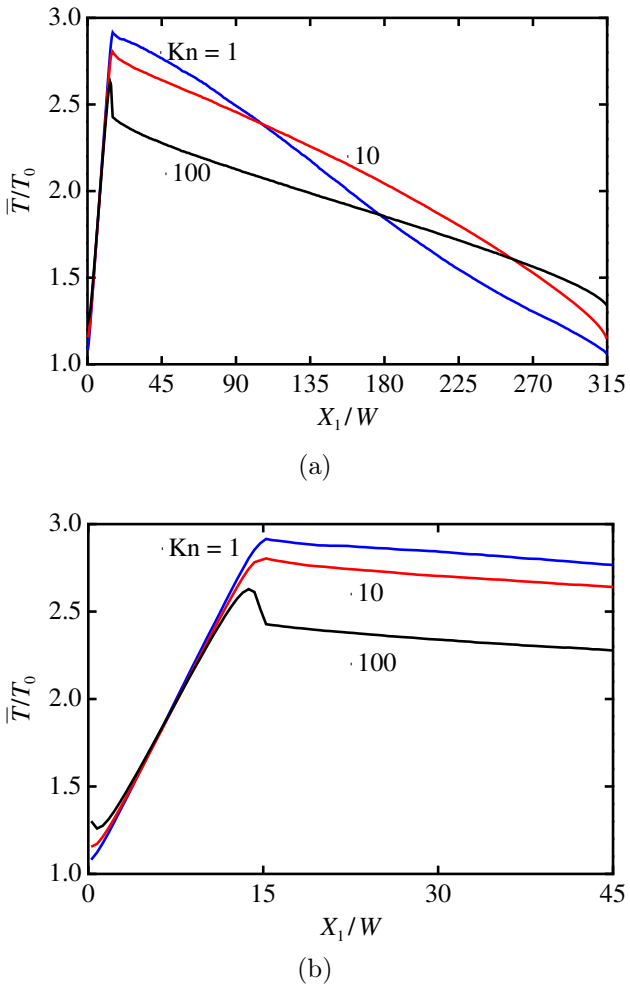

Figure 2.16: The cross-sectional average of the temperature $\bar{T}(X_1)$ for $D/L = 20$ ($L/W = 15$) ; (a) the overall view ($0 < X_1/W < 315$) and (b) close up view around the channel ($0 < X_1/W < 45$).

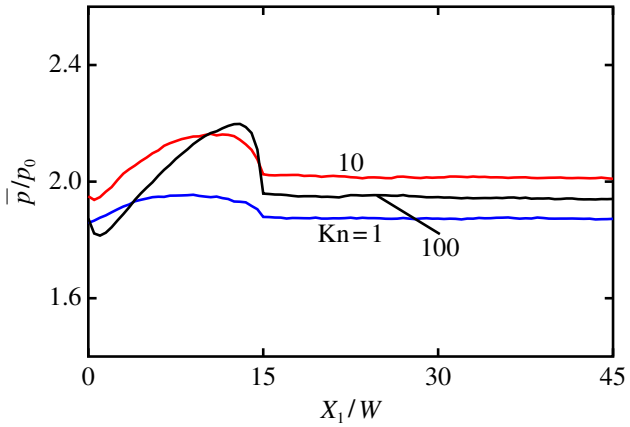

Figure 2.17: The cross-sectional average of the the pressure $\bar{p}(X_1)$ for $D/L = 20$ ($L/W = 15$). Only the distribution near the P part ($0 < X_1/W < 45$) is shown.

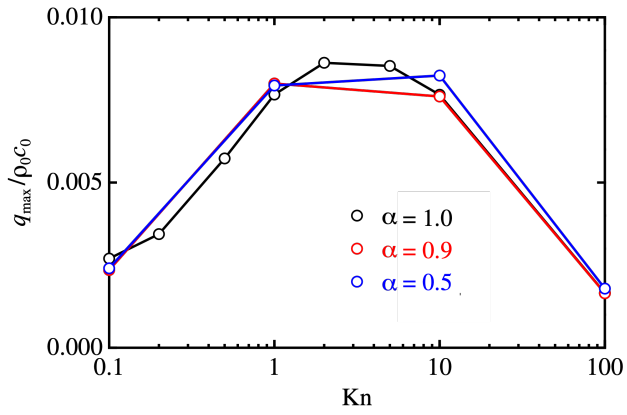

Figure 2.18: Effect of the accommodation coefficient. Non-dimensional maximum mass flux $q_{\max}/\rho_0 c_0$ versus Kn. $\alpha = 0.5$ and 0.9. The corresponding values already shown in Fig. 2.11 are also plotted as $\alpha = 1$. RP [Fig. 2.4(a)] with $D/L = 2,\ L/W = 15$.

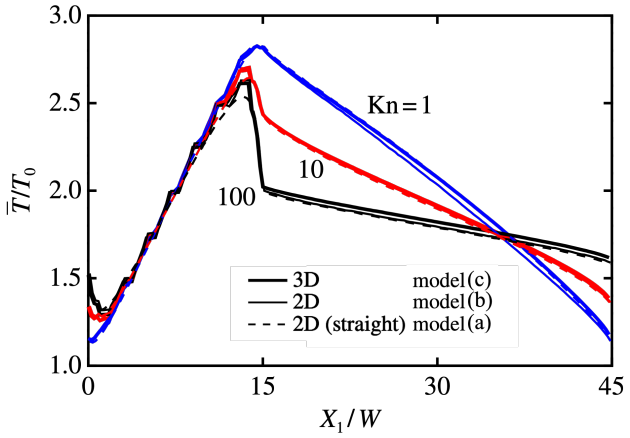

(a)

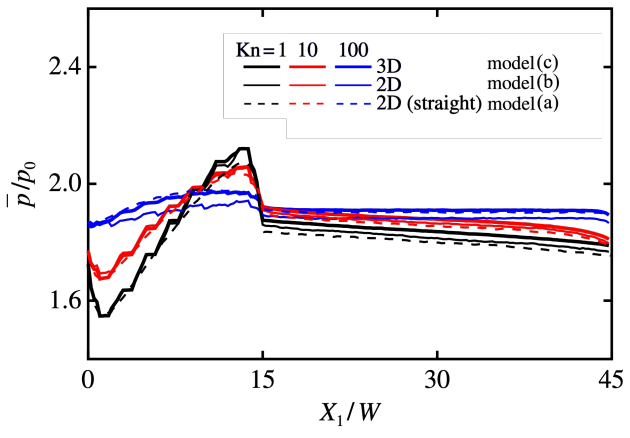

(b)

Figure 2.19: (a) The distribution of $\bar{T}(X_1)$ and (b) the distribution of $\bar{p}(X_1)$. ($L/W = 15$, $D/L = 2$).

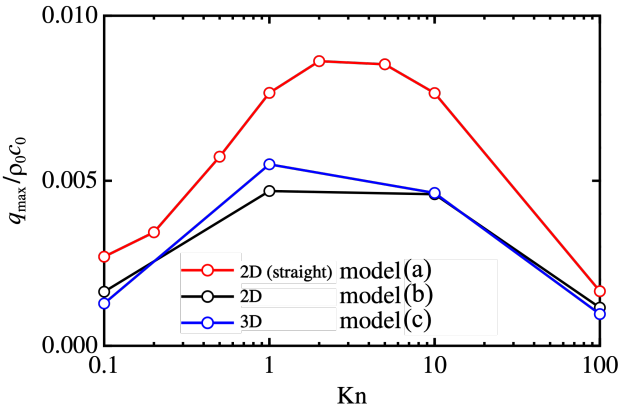

Figure 2.20: Non-dimensional maximum mass flux $q_{\max}/\rho_0 c_0$ versus Knudsen number Kn ($L/W = 15$ and $D/L = 2$).

are shown in Fig. 2.19. The temperature and pressure do not depend on the pore shape. However, the dependence of q_{max} on the pore shape is appreciable as shown in Fig. 2.20. These results suggest that the simple straight-through channels is preferable.

2.5.4 Maximum compression ratio

We analyze the pressure ratio and local Kn for each unit according to [5]. The numerical computations for the maximum compression ratio analysis are carried out with a small number of particles (200 per cell) because of the limited computational resources. Figure 2.21 shows the time evolution of $\bar{T}(X_1)$ and that of $\bar{p}(X_1)$ (five elements of model (a) for $L/W = 15$, $D/L = 2$, and Kn = 1). While the temperature field arrive at the steady state at around $t/t_0 \sim 1000$, the time variation of pressure is very slow. The mass flux in the X_1 direction $q(t, \boldsymbol{X})$ should be theoretically vanish at the steady state. We define $q(t)$ as the volume average of $q(t, \boldsymbol{X})$, here t is defined as $t = j\Delta t$ (j is the time step of the computation). The $|q(t)/\rho_0 c_0| < 2 \times 10^{-3}$ at $t/t_0 = 6000$ and $|q(t)/\rho_0 c_0| < 2 \times 10^{-4}$ at $t/t_0 = 12000$ are confirmed.

We want to obtain the compression ratio and the local Knudsen number at the steady state for each element $i = 0$, 1, 2, 3, and 4. At each time step, we defined the following quantities. The $q_i(t)$ is the volume average of the mass flux in the X_1 direction of element i. The $\langle p \rangle_i(t)$ is the volume average of the pressure over the sub empty space of element i. From these quantities, we define $\gamma_i(t)$ and $q_i(t)$ is defined by

$$q_i(t) = \frac{\langle q \rangle_i(t) + \langle q \rangle_{i-1}(t)}{2}, \tag{2.22}$$

$$\gamma_i(t) = \frac{\langle p \rangle_i(t) - \langle p \rangle_{i-1}(t)}{\left(\langle p \rangle_i(t) + \langle p \rangle_{i-1}(t)\right)/2}, \tag{2.23}$$

where $i = 1$, 2, 3, and 4.

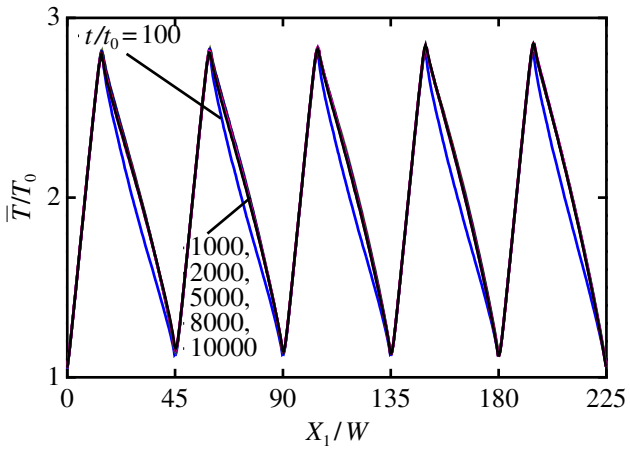

(a)

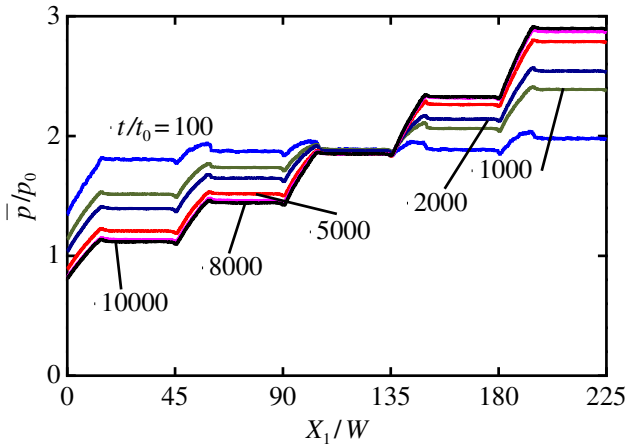

(b)

Figure 2.21: Time evolution of (a) $\bar{T}$ and (b) that of $\bar{p}$ ($L/W = 15$, $D/L = 2$, and Kn $= 1$). Five elements of model (a) are connected in series as shown in Fig. 2.5(a).

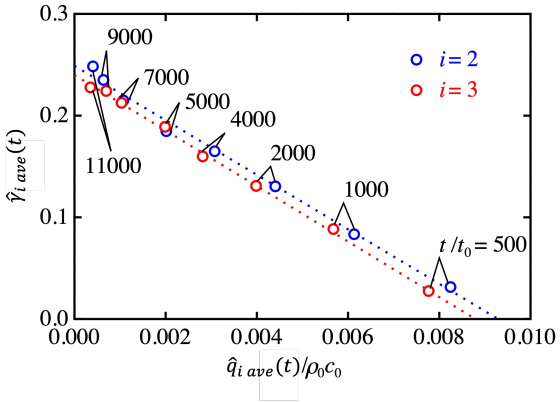

Figure 2.22: The compression ratio $\gamma_i(t)$ vs the non-dimensional mass flux $\widehat{q}_i(t)/\rho_0 c_0$ for element-i ($i = 2$ and 3). $L/W = 15$, $D/L = 2$, and Kn $= 1$. The dotted lines indicate the lines obtained by the least square approximation.

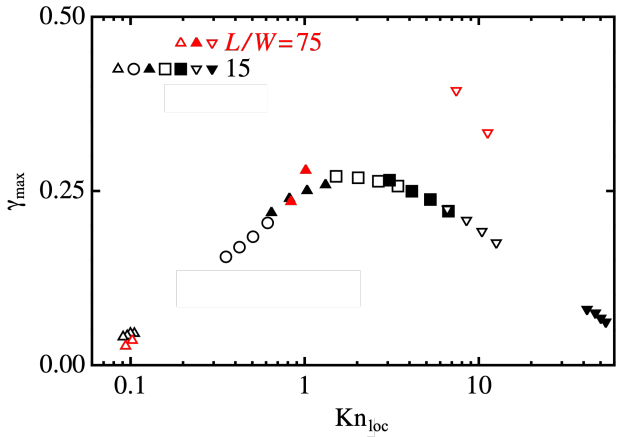

Figure 2.23: Compression ratio $\gamma_{\max}$ versus the local Knudsen number Kn_i for RP shown in Fig. 2.4(a). $L/W = 75$ (red) and 15 (black). $D/L = 2$. Symbols express the Knudsen number Kn for the initial uniform state: △: 0.1, ○: 0.5, ▲: 1, □: 2.5, ■: 5, ▽:10, and ▼: 50.

In each time step j, γ_i and q_i are computed. As done for q in Eqs. (2.20) and (2.21), we define $\tilde{\gamma}_i(n)$, $\tilde{q}_i(n)$, $\tilde{\gamma}_{iave}(m)$, and $\tilde{q}_{iave}(m)$:

$$\hat{\gamma}_i(n) = \frac{1}{a_0}\sum_{j=0}^{a_0-1}\gamma_i(a_0(n-1)+j), \tag{2.24}$$

$$\hat{q}_i(n) = \frac{1}{a_0}\sum_{j=0}^{a_0-1} q_i(a_0(n-1)+j), \tag{2.25}$$

$$\hat{\gamma}_{iave}(m) = \frac{1}{b_0}\sum_{k=0}^{b_0-1}\hat{\gamma}_i(b_0(m-1)+k), \tag{2.26}$$

$$\hat{q}_{iave}(m) = \frac{1}{b_0}\sum_{k=0}^{b_0-1}\hat{q}_i(b_0(m-1)+k). \tag{2.27}$$

Here, we use $(a_0, b_0) = (50000, 10)$. The plots of $(\hat{q}_{iave}/\rho_0 c_0, \hat{\gamma}_{iave})$ thus obtained is shown in Fig. 2.22 for $i = 2$ and 3 and $m = 1$, 2, 4, 8, 10, 14, 18, and 22 ($t/t_0 = 500$, 1000, 2000, 4000, 5000, 7000, 9000, and 11000). The points $(\hat{q}_{iave}/\rho_0 c_0, \hat{\gamma}_{iave})$ for each i are almost on the same straight line; since the same tendency is confirmed for $i = 1$ and 4, the plots of $(\hat{q}_{iave}/\rho_0 c_0, \hat{\gamma}_{iave})$ for $i = 1$ and 4 are omitted in the figure. The compression ratio at the point of $\hat{q}_{i\,ave} = 0$ inferred from this straight line is the maximum compression ratio $\gamma_{\max}$ for the element. We define the averaged local Knudsen number for the element i at the steady state by

$$\mathrm{Kn}_{\mathrm{loc}}^{(\mathrm{i})}(\mathrm{t}) = \frac{\ell_i(t)}{W}, \tag{2.28}$$

where ℓ_i is the averaged local mean free path defined by

$$\ell_i(t) = \ell_0 \frac{p_0}{T_0}\frac{\langle T\rangle_i(t)}{\langle p\rangle_i(t)}, \tag{2.29}$$

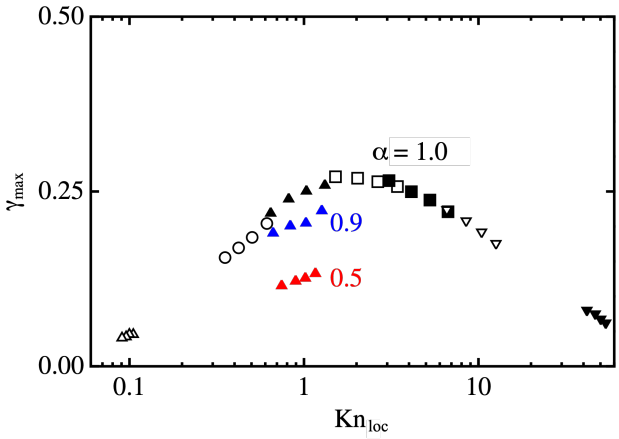

Figure 2.24: Effect of the accommodation coefficient on the compression ratio. Compression ratio $\gamma_{\max}$ versus the local Knudsen number Kn_i for $\alpha = 0.5$ and 0.9. The data for $\alpha = 1$ already given in Fig. 2.23 are plotted for comparison. $L/W = 15$ and $D/L = 2$.

cf. the definition of the mean free path for hard sphere molecules Eq. (2.8).

As done for $\hat{q}_{iave}$ and $\hat{\gamma}_{iave}$, we define $\hat{\mathrm{Kn}}_{\mathrm{loc}}(n)$ and $\hat{\mathrm{Kn}}_{\mathrm{loc}\,ave}(m)$:

$$\hat{\mathrm{Kn}}_{\mathrm{loc}}^{(i)}(n) = \frac{1}{a_0}\sum_{j=0}^{a_0-1} \mathrm{Kn}_{\mathrm{loc}}^{(\mathrm{i})}(a_0(n-1)+j),$$

$$\hat{\mathrm{Kn}}^{(i)}{}_{\mathrm{loc}\,ave}(m) = \frac{1}{b_0}\sum_{k=0}^{b_0-1} \hat{\mathrm{Kn}}_{\mathrm{loc}}^{(i)}(b_0(m-1)+k).$$

Since $\hat{\mathrm{Kn}}_{\mathrm{loc}\,ave}^{(i)}$ is nearly constant at $t/t_0 > 10000$, the last 500000 average is adopted as the local Knudsen number of each element $\mathrm{Kn}_{\mathrm{loc}}{}^{(i)}$at the steady state.

In addition to the computation for $L/W = 15$ (Kn = 0.1, 0.5, 1, 2.5, 5, 10, and 50), the computation for $L/W = 75$ (Kn = 0.1, 1, and 10) are also carried out. The results $\gamma_{max}\left(\mathrm{Kn}_{\mathrm{loc}}{}^{(i)}\right)$ are also plotted in Fig. 2.23. In the figure, the results for $L/W = 15$ are shown in black and those for $L/W = 75$ are done in red; different symbols are used to identify the initial Knudsen number Kn value: △: 0.1, ○: 0.5, ▲: 1, □: 2.5, ■: 5, ▽:10, and ▼: 50. Only the data for $i = 1$ and 4 are plotted for $L/W = 75$ since the time developments for $i = 2$ and 3 are too slow. The influence of L/W on γ_{max} is small for small Kn, but it is appreciable for large Kn. Although the plots for $L/W = 15$ seems to lie on a curve, it is not regarded as the universal curve because the computation for larger elements is not carried out. Nevertheless, the dependence of γ_{max} on $\mathrm{Kn}_{\mathrm{loc}}{}^{(\mathrm{i})}$ seems to be appreciable, which is in contrast to the case of KP [5].

The effect of the accommodation coefficient α is confirmed for the case of $L/W = 15$. The maximum compression ratio values $\gamma_{\max}$ for $\alpha = 0.5$ and 0.9 are compared with that for $\alpha = 1$ in Fig. 2.24. The effect of accommodation coefficients on γ_{max} is appreciable, which is in contrast to q_{max}.

2.6 Concluding remarks

In KP, thermal transpiration flows in mutually opposite directions are induced around the heated connection point and collide there. This causes a pressure increase and results in two pressure-driven flows in mutually opposite directions. The one-way flow in KP can be understood as the combination of these flows, although the flow field is far from the one-dimensional in certain cases for small Kn. The rough estimate for KP in Sec. 2.4.1 should be used with caution. In RP, on the other hand, thermal transpiration flow is absent in the empty region. Instead of the thermal transpiration flow, thermal edge flow is induced in the empty region as the flow in the opposite direction. Then, the pressure-driven flow is generated in the channel as the consequence of the collision between these flows. The thermal edge flow should not be regarded as the thermal transpiration flow, and the rough estimate in Sec. 2.4.1 should not be used for RP.

The analysis of RP models [Figs. 2.4 (a)-(c)] indicate that a simpler channel structure is preferred for increasing the flow rate. The effect of the accommodation coefficient is found to be small for the flow rate but appreciable for the compression ratio. The larger the accommodation coefficient, the larger the pressure difference obtained. These results can be employed as the design guidelines when producing RP as MEMS. Recent MEMS pumps have smaller L/W and higher flow rates. The present numerical results confirm this tendency.

Chapter 3

Numerical analysis of actual Reynolds-type pump [67]

3.1 Introduction

Chapter 2 provides basic properties of RP including the driving mechanism. Most of pumps currently produced as MEMS consist of many ($\simeq 10^4$) micro channels of repeating structures [3, 4, 19, 20, 27–48]; as seen Fig. 2.4 in Chapter 2, such MEMS pumps are categorized into RP. Numerical analysis of flows in such micro apparatus, however, has not yet been carried out because of high computational cost. The rough estimate for KP is not applicable to RP. As in Chapter 2, RP can be computed with periodic boundary conditions if the effect of the apparatus edge is neglected; if one element is symmetric, the computational domain can be further reduced. In [76], a practical RP is built and experimental data on its performance is available. Here we carry out the numerical analysis of rarefied gas flow induced in the RP of [76] and compare the numerical results with the experimental data.

3.2 Numerical settings

3.2.1 Design of pump

Figure 3.1 shows an overall view of the MEMS pump actually fabricated and experimented in [76]. The pump's dimensions are on the order of micrometers: e.g., $D = 2\,\mu$m and $H = 120\,\mu$m, respectively. Figure 3.2 shows the part of the internal channel structure. The flow paths are arranged in parallel in a series of holes in a Si chip. The red part is a heater. The blue part is a cooler, which maintains a constant temperature. A green channel wall connects the heater and the cooler. See [76] for detailed structure and materials.

In analyzing the gas flows in RPs, we need the Boltzmann equation to describe the gas flows in micro-channels. The extensive computational resource required by the Boltzmann equation lets researchers use 1D or 2D models in the previous works [5, 6, 77–80]. However, the periodic structure and the small aspect ratios of the channel shown in Fig. 3.1 enable us to analyze the gas flows in three dimensions using the pump's actual sizes by the well-known DSMC method [69]. We have only to consider the gas flows in a element indicated

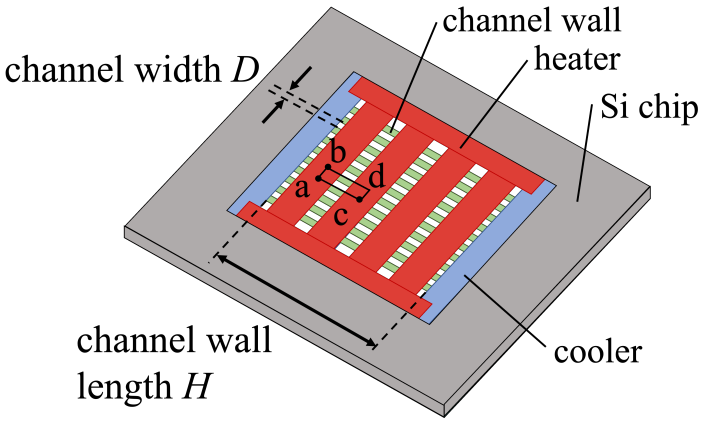

Figure 3.1: Schematic of an actual MEMS RP [76]. The pump is made on Si chip and has heater, channel wall, and cooler. Channels penetrate the Si chip.

by the rectangle abcd in Fig. 3.1. We will carry out the numerical analysis not only for the experimental condition, i.e., under atmospheric pressure; we will consider a more comprehensive range of the Knudsen number. In the present chapter, we use the spacing between the channel walls as the reference length D. The dimensions of the components in Fig. 3.2 are described by the ratio to the reference length D, and the ratios are those of the actual device fabricated in [76]. The temperature of the cooler and the heater are, respectively, uniform at T_0 and T_h. The temperature of the channel wall T_w has a linear temperature distribution in the X_1 direction, where X_1 is the spatial coordinate parallel to the channel wall in the direction from the cooler part to the heater part. The X_2 axis is normal to the channel wall, and thus X_3 becomes the direction transverse the channel wall. The origin is indicated by O in the figure. This structure is assumed to spread periodically in the X_2 and X_3 directions.

3.2.2 Plan of computation

The maximum flow rate q_{max} and the maximum compression ratio γ_{max} are numerically analyzed. For the maximum flow rate q_{max}, as in Chapter 2, the calculation is performed for one element with periodic conditions in the X_1 direction. For the maximum compression ratio γ_{max}, only one element is used in this calculation because of the limitation of the computational cost. Air reservoirs are connected to the element in order to keep the sealed wall away from the element. Baffle plates are inserted to keep the temperature in reservoirs at a constant T_0.

3.2.2.1 Computation for mass flow rate

The maximum flow rate is computed by using the model shown in Fig. 3.3. This model adds a gas region at the pump's outlet. By this region, we can connect the pump's inlet to the outlet of the gas region by the periodic condition [cf. Eqs. (2.7)]. A gas region has a length of $15D$ in the X_1 direction.

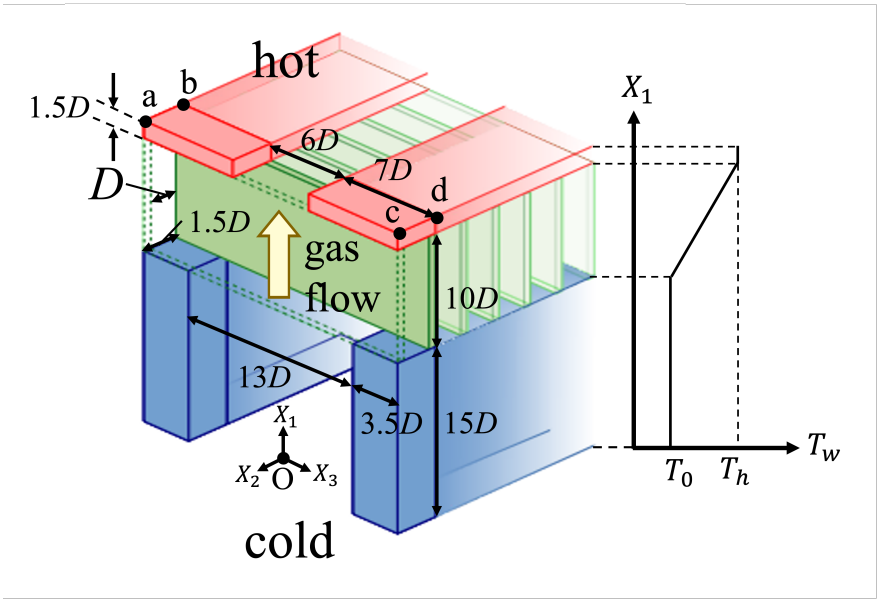

Figure 3.2: The part of the internal channel structure. Blue cuboids indicate the cooler parts. Red cuboids indicate the heater parts. Green cuboids indicate the channel walls. The channel walls have a temperature gradient in the X_1 direction.

Approximately 10000 elements (100×100) align side-by-side in the device fabricated by An et al. in [76]. There is a 100 times difference in the channel width between the inside and outside of the device. This leads to uniform behavior of the gas among these elements (see Ref. [13]) because only a part of the external flow structure affects each internal flow structure. In view of this fact, we neglect the effect of the outer region. In this case, we can apply the periodic boundary condition between the inlet and outlet of the element, making it possible to carry out detailed 3D analysis in each element.

3.2.2.2 Computation for compression ratio

The maximum compression ratio is computed by using the model shown in Fig. 3.4. Air reservoir tanks, tank-L, and tank-R are connected to both ends of the pump in the X_1 direction. The length of the air reservoir in the X_1 direction is $30D$. Each end of the air reservoir in the X_1 direction is the diffuse wall [cf. Eq. (2.6a) for $\alpha = 1$] with a uniform temperature T_0. We also insert the baffle regions between the pump and the air reservoir. If the air reservoir is connected directly to the pump, the temperature inside the reservoir will rise due to the hot particles moving from the heater. The purpose of these baffles is to keep the temperature in the air reservoir constant around T_0.

3.3 Parameters of DSMC

The calculation method is the DSMC method introduced in Sec. 2.3.1. As mentioned there, the results of the DSMC method are statistical results with a range of fluctuation. In order to make quantitative comparisons with actual experimental results, this chapter introduces

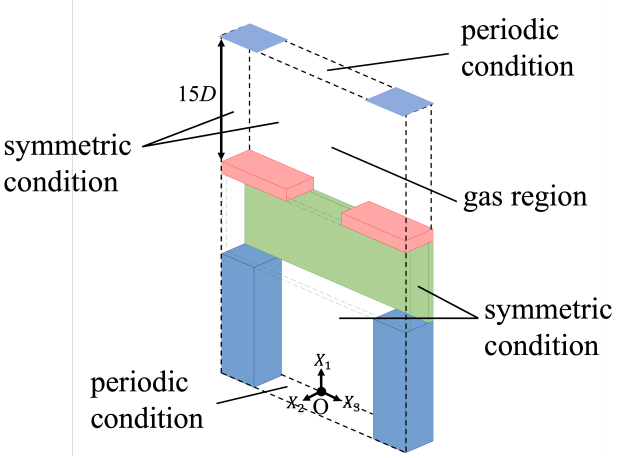

Figure 3.3: Structure of the maximum flow rate model.

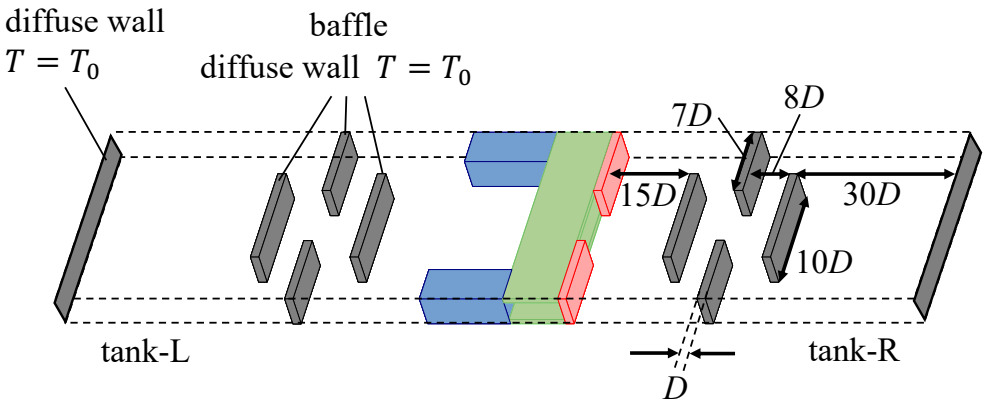

Figure 3.4: Structure of the model to obtain the pressure difference. The colors of the parts correspond to those in Fig. 3.2. Newly added parts for pressure analysis are colored in gray.

3σ with standard errors as error bars. The time step is $\Delta t = 0.001 t_0$. The cell size of the three-dimensional model is $(\mathrm{d}X_1, \mathrm{d}X_2, \mathrm{d}X_3)=(0.25D, 0.125D, 0.25D)$. Each cell contains 2000 simulation particles for the maximum flow analysis and 20 particles for the maximum compression ratio analysis.

3.4 Results

3.4.1 The maximum flow rate

3.4.1.1 The three-dimensional flow fields

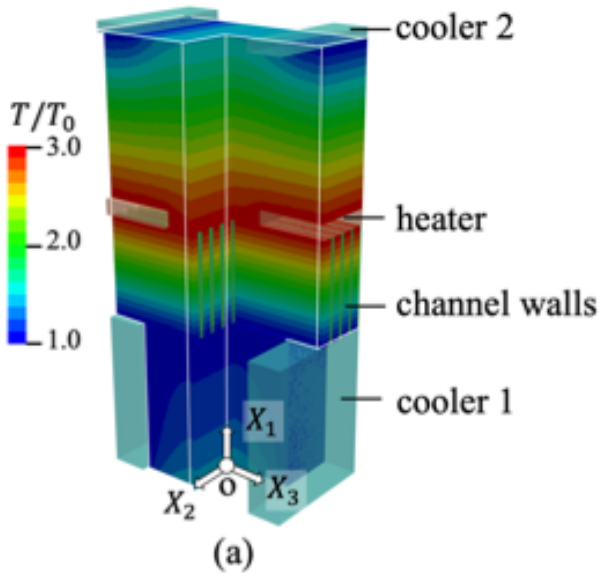

(a)

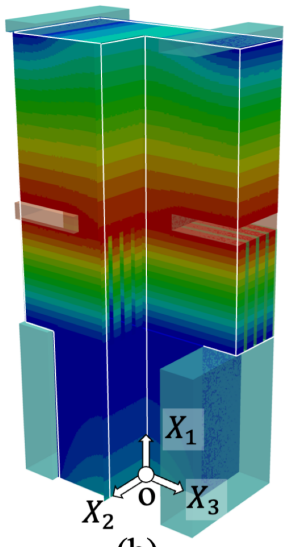

(b)

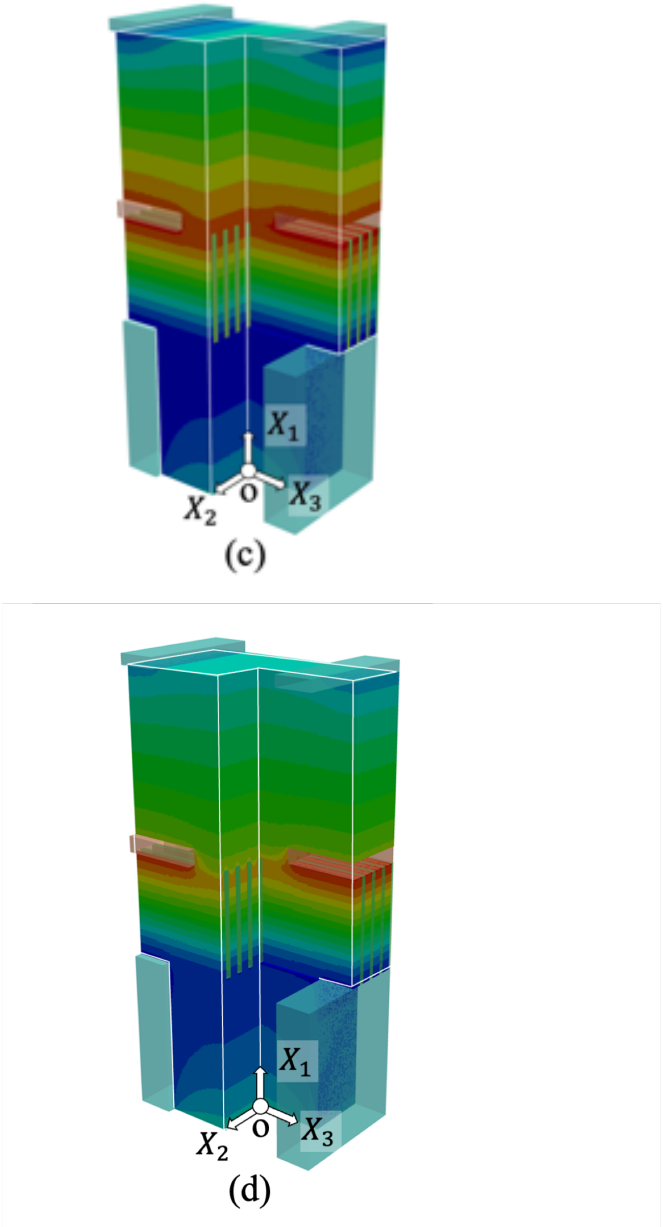

Figure 3.5: Non-dimensional temperature field of the steady-state. (a) Kn = 0.03, (b) Kn = 0.1, (c) Kn = 1, and (d) Kn = 10. $\Delta T/T_0 = 2.0$

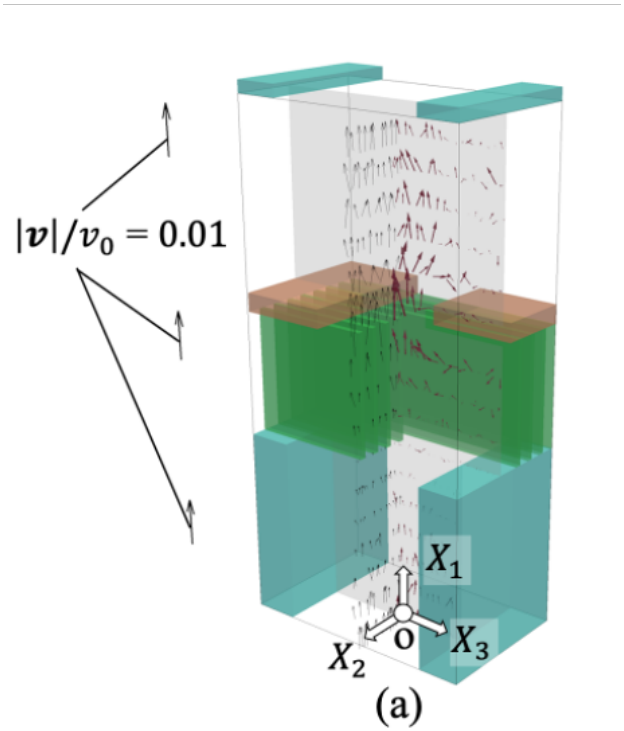
$|\boldsymbol{v}|/v_0 = 0.01$
X_1
O
X_3
X_2
(a)

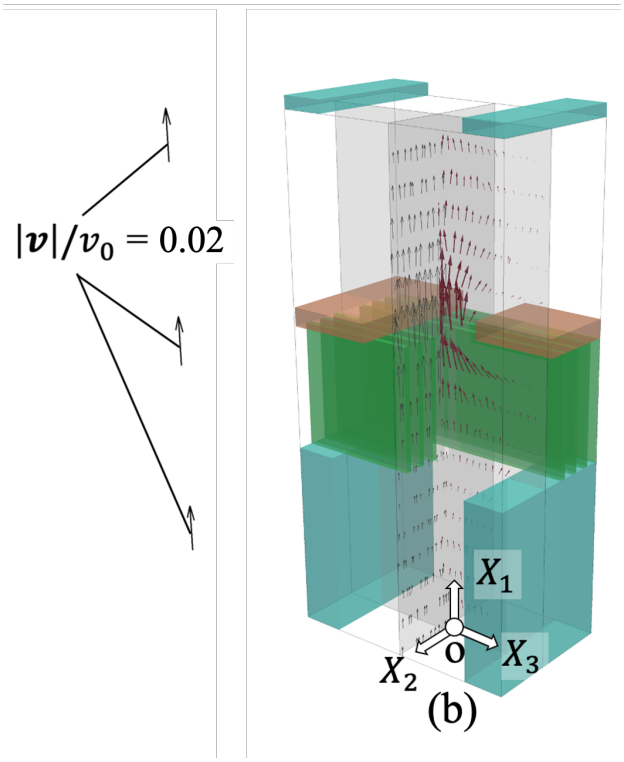
$|\boldsymbol{v}|/v_0 = 0.02$
X_1
O
X_3
X_2
(b)

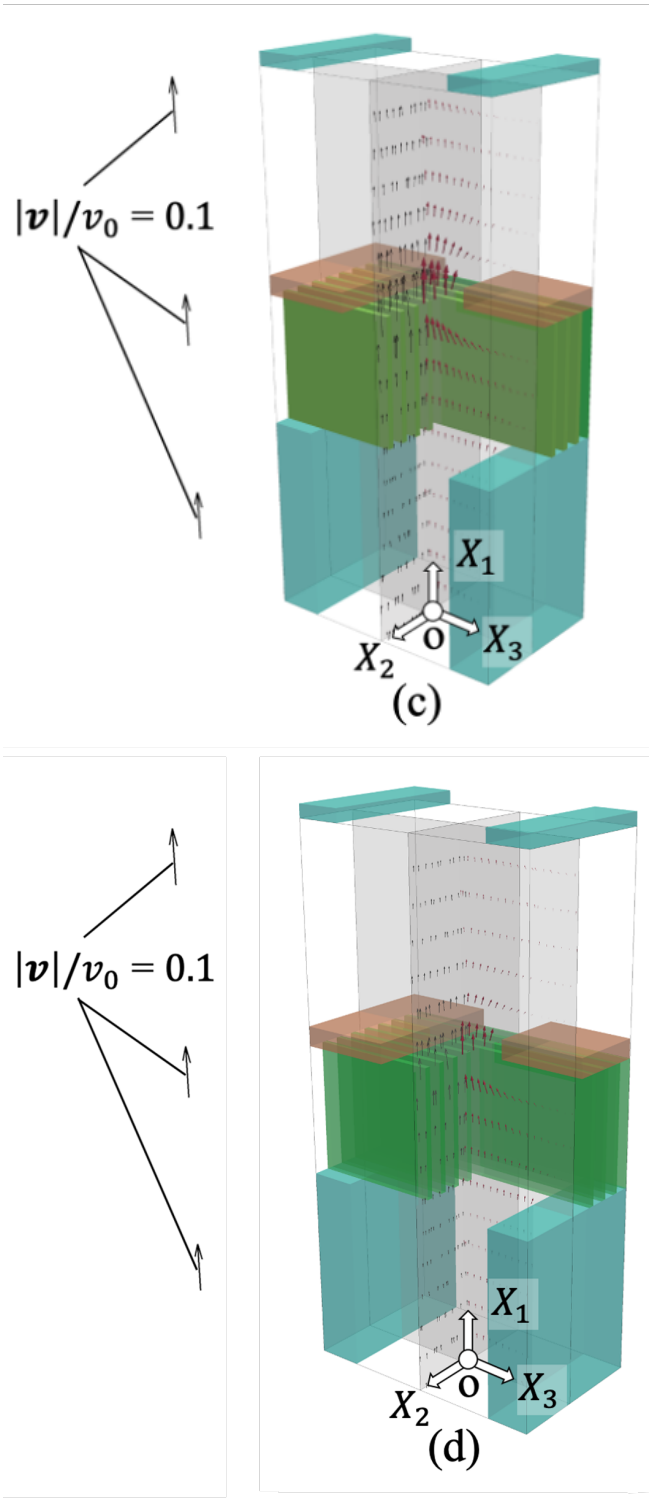

Figure 3.6: Non-dimensional velocity field of the steady-state. (a) Kn = 0.03, (b) Kn = 0.1, (c) Kn = 1, and (d) Kn = 10. $\Delta T/T_0 = 2.0$.

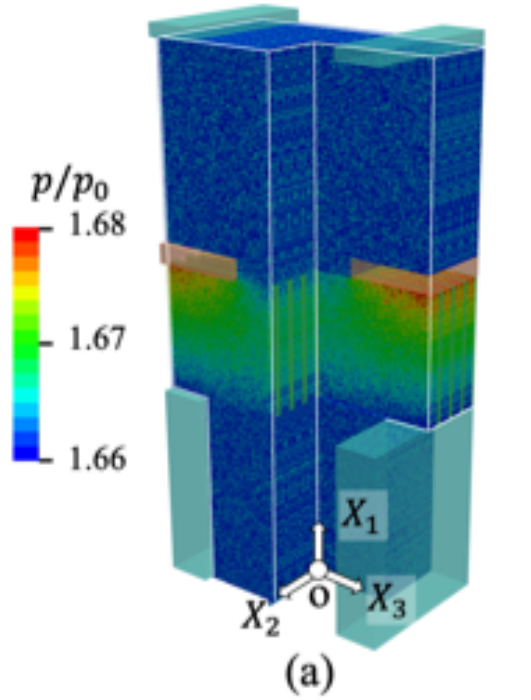

(a)

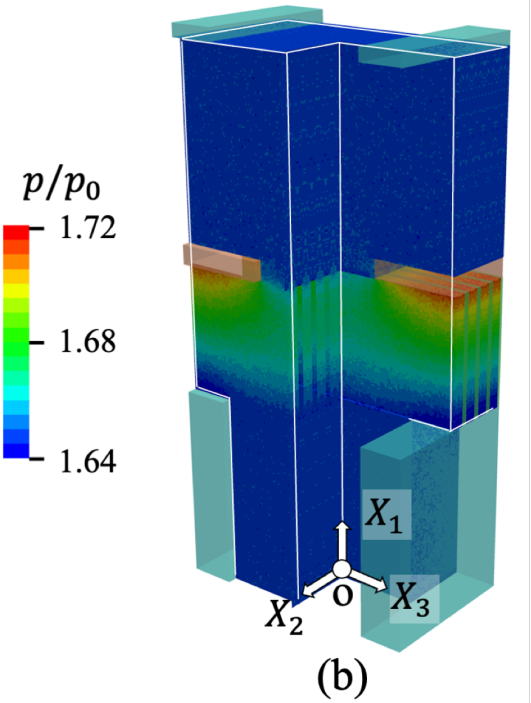

(b)

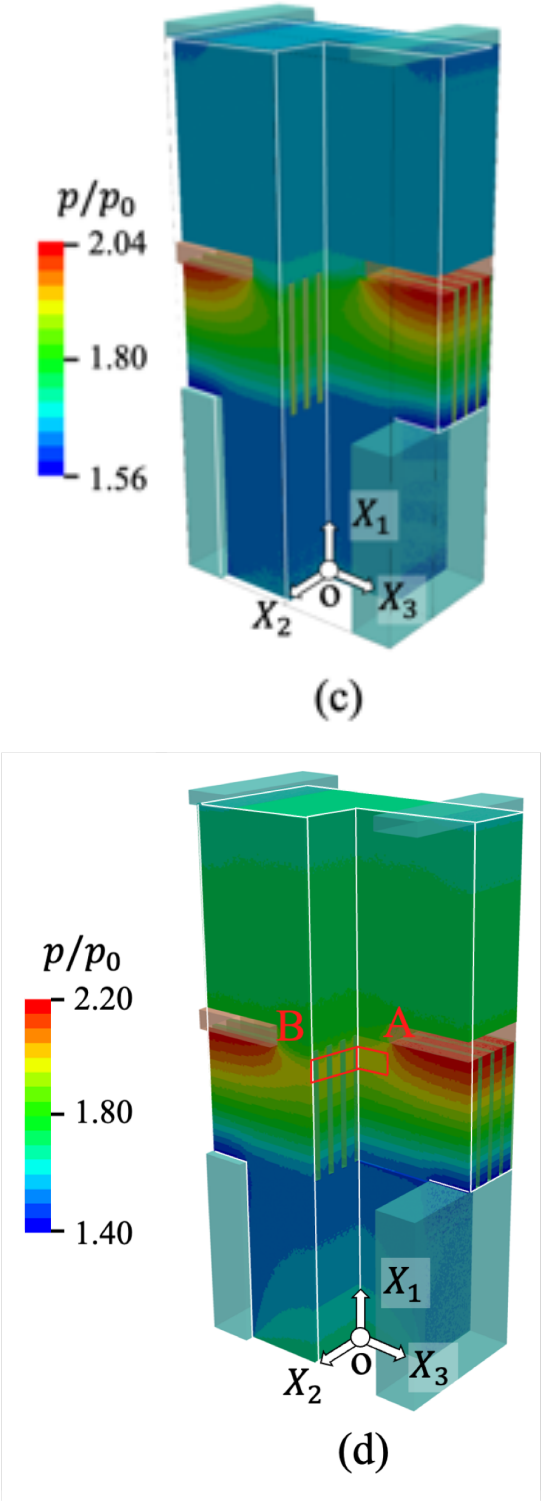

Figure 3.7: Non-dimensional pressure field of the steady-state. (a) Kn = 0.03, (b) Kn = 0.1, (c) Kn = 1, and (d) Kn = 10. $\Delta T/T_0 = 2.0$.

For the maximum flow rate analysis, a gas domain is established in one element, and a periodic condition is imposed on the direction in which the flow occurs [Fig. 3.3]. The initial condition is a stationary equilibrium state. The steady-state is defined as the state when the time variation of the macroscopic field becomes smaller than the fluctuation of DSMC.

Figures 3.5-3.7 show the three-dimensional fields of temperature, velocity, and pressure at the steady-state for the numerical model shown in Fig. 3.3, respectively. To grasp the flow field intuitively, we connected several of the numerical models in the X_2 direction. The panel (a) of each figures is the results for Kn = 0.03, (b) for Kn = 0.1, (c) for Kn = 1, and (d) for Kn = 10. The non-dimensional time t/t_0 used for averaging is 300 for Kn = 0.03 and that for the others is 100. That is, the macroscopic quantities in each cell are computed in the same way as in Eqs. (2.20) and (2.21), where (a_0, b_0) is (10000, 30) for Kn = 0.03 and (10000, 10) for the others. In addition, for all panels, the non-dimensional temperature difference

$$\Delta T/T_0 = (T_h - T_0)/T_0$$

is 2.0. These figures also include the structural elements of the pump; that is, the blue cuboids are the coolers (cf. Fig. 3.3). The green ones are the channel walls, and the reds are the heaters. The cooler appears again at the top because we set periodic condition here. The axes X_i and the origin O also appear on the bottom of the figure for reference.

The colors in the gas part in Figs. 3.5 and 3.7 indicate the values T/T_0 or p/p_0 on the corresponding cross-sections. The $X_3 < 0$ (i.e., left in the figure) part of the X_1X_3 cross-section shows the value at the median plane between the channel walls, while the $X_3 > 0$ (right in the figure) part does at the surface of the channel walls. The part $X_3 = 0$ corresponds to the X_1X_2 cross-section through the origin.

Figure 3.5 shows that the gas temperature varies approximately only in the X_1 direction. The temperature is uniformly low between the cooler parts 1, and it increases linearly in the narrow space between the channel walls up to the value at the heater position. The temperature decreases in the gas region above the heater in the figure due to the cooler parts 2. The temperature of the gas in the channel is close to that of the channel walls. For the cases of Kn = 1 and 10, however, the increase in gas temperature around the heater is suppressed. Thus the temperature difference between the heater and the gas increases for these Knudsen numbers. The significant temperature jump for high Kn is quite natural in the rarefied gas since the gas molecules near the heater come from a broader region where the temperature is small. This temperature field is considered to induce thermal edge flow at the channel end, as described in Chapter 2.

In Fig. 3.6, the velocity field is visualized as the velocity vector projected onto the X_1X_2 and X_1X_3 cross-section at $X_3 = 0$ and $X_2 = 0$, respectively. For the sake of simplicity and visibility, we show only the front half of each cross-section. Figure 3.6 shows that the gas generally flows in the positive direction of the X_1 axis, confirming that the flow direction is determined by thermal transpiration flow in the narrow part between the channel walls. The flow velocity accelerates in the region where the channel cross-section is narrow with the heater. Note that the same arrow size means the different sizes of the velocities in each figure. For example, the velocity at Kn = 0.03 is approximately 1/10 of that at Kn = 1. As the flow velocity becomes small, the ratio of fluctuation to velocity, which is inevitable in

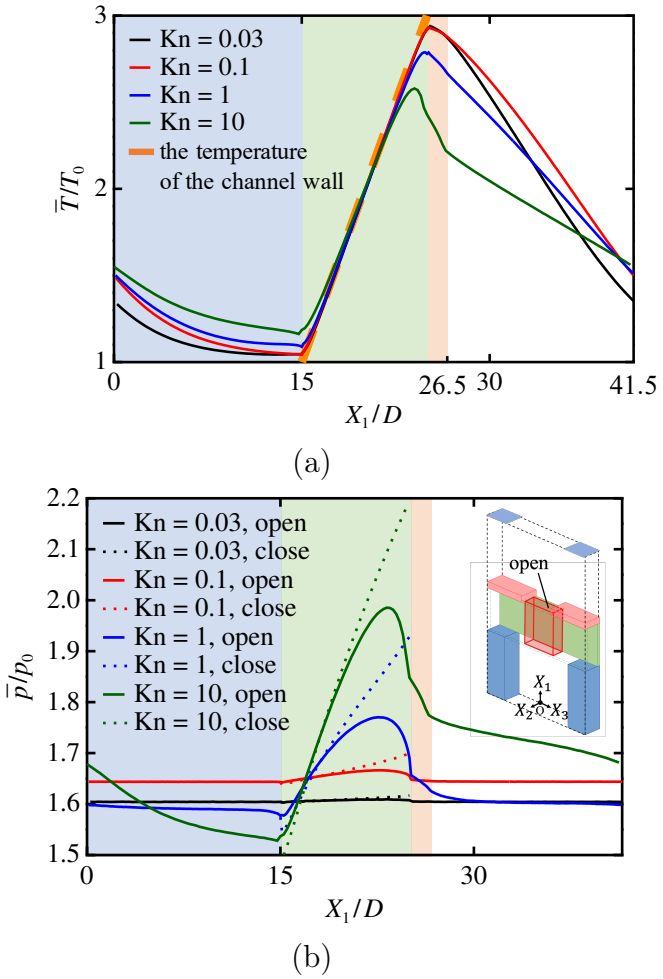

Figure 3.8: (a) Non-dimensional distributions of the cross-sectional average of the temperature and (b) that of the pressure in X_1 direction for the case of Kn = 0.03, 0.1, and 1, and $\Delta T/T_0 = 2.0$. Blue area indicates the cooler parts. Green area indicates flow channel parts. Red area indicates heater parts. In panel (a), the "open" means the average over the part where the flow is not interrupted. The "close" means that over the rest of the flow channel.

the DSMC method, becomes large. This is why the non-dimensional time used for averaging is 300 for Kn = 0.03 and that for the others is 100.

Figure 3.7 shows the distribution of the pressure in the gas. It can be seen that the pressure increases in the part of the channel where the heater obstructs the flow. This result suggests the existence of the local pressure-driven flow, which can not be considered in the one-dimensional analysis (Ref. [76]). We observe a discontinuity of the pressure in the right half ($X_3 > 0$) of the figures [e.g., area A in panel (d)]. This discontinuity is caused by the corner singularity at the edge of the channel walls. In the X_1X_2 cross-section, the pressure distribution is continuous (see the contour at $X_3 = 0$). Therefore, the pressure distribution discontinues at the edge [e.g., area B in panel (d)]. As the Knudsen number decreases, the overall pressure change becomes smaller, but the distribution trend is consistent for all Knudsen numbers.

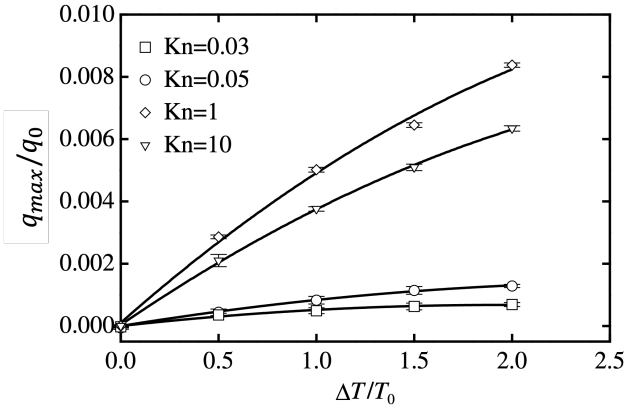

Figure 3.9: Non-dimensional mass flux q_{max}/q_0 vs non-dimensional temperature difference $\Delta T/T_0$ for Kn = 0.03, 0.05, 1, and 10. The solid lines indicate quadratic regression curves.

Figure 3.8 shows the average distribution of temperature $\bar{T}/T_0$ and pressure $\bar{p}/p_0$ for the case of Kn = 0.03, 0.1, 1, and 10. The gas temperature $\bar{T}/T_0$ [panel (a)] increases linearly along the channel walls at $15 < X_1/D < 25$. For Kn ≤ 1, the gas temperature is close to that of the channel wall (orange dashed line). The temperature decreases in the gas region $26.5 < X_1/D < 41.5$. The temperature becomes close to that of the cooler in the cooler region $0 < X_1/D < 15$ and is close to uniform at $X_1/D \approx 15$. Panel (b) shows the distribution of the average pressure $\bar{p}/p_0$. Two different parts of the cross-section are adopted here: the cross-section used in the data indicated by "open" is limited to the part without the heater [$0 < |X_3/D| < 3$, see the red box in the panel (b)], and "close" uses the other region: that is, the region plugged by the heater. The difference of the two averaged pressures become large only in the region between the channel walls ($15 < X_1/D < 25$). The pressure in the "close" region takes a large value before the heater, confirming the pressure increase seen in the three-dimensional figure (Fig. 3.7). The pressure drops, however, suddenly at the hole between the heater ($X_1/D \approx 25$). The large pressure drop inevitably induces a large flow velocity in the X_1 direction.

3.4.1.2 Effect of various parameters on the maximum flow rate

As in Chapter 2, maximum mass flux in the X_1 direction, q_{max}, is calculated. Here, we take the same approach as in Eqs. (2.20) and (2.21), where $(a_0, b_0) = (10000, 10)$. Figure 3.9 shows the results of the mass flux through the pump. Here, $q_0 = mn_0c_0$. In addition to Kn = 0.03, we calculate the steady-state flow rate for Kn = 0.05, 1, 10 to investigate the flow rate under more dilute conditions. For each Knudsen number, we carried out the computation for five temperature difference ratios $\Delta T/T_0 = 0.0,\ 0.5,\ 1.0,\ 1.5,$ and 2.0. The range of $\pm 3\sigma$ is indicated by the error bars, where σ is the standard error value estimated from the data. This represents the range of results for the DSMC method and is introduced in this chapter for quantitative evaluation. There is no flow rate within the fluctuation when the temperature difference vanishes. For all Knudsen numbers, the flow rate increases with increasing $\Delta T/T_0$. It does not, however, appear to be changing almost linearly. In Fig. 3.9, we add a quadratic regression curve to the figure.

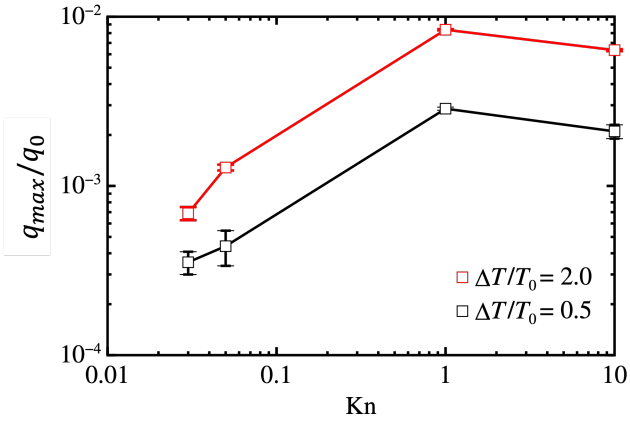

Figure 3.10: Non-dimensional mass flux q_{max}/q_0 vs Knudsen number for $\Delta T/T_0 = 0.5$ and 2.0.

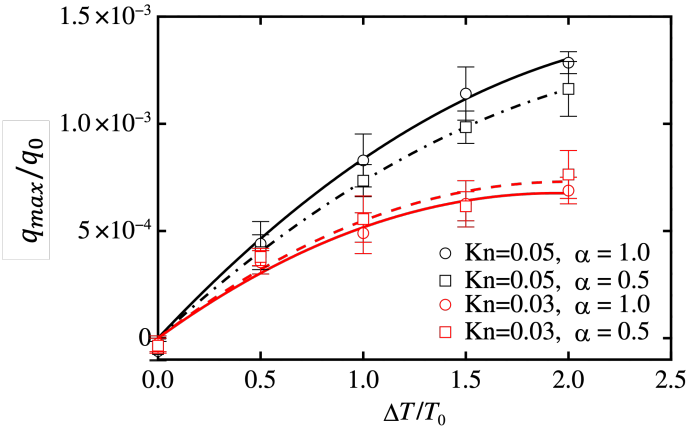

Figure 3.11: Non-dimensional mass flux q_{max}/q_0 vs non-dimensional temperature difference (Kn = 0.03 and 0.05, $\alpha = 0.5$ and 1.0).

We show the relationship between the Knudsen number and the maximum flow rate with each $\Delta T/T_0$ in Fig. 3.10. We have the maximum value of the flow rate for all temperature differences around Kn = 1. Chapter 2 reports that there is some Knudsen number at which the flow rate peaks in RP, and the present model has the same tendency.

We investigate the effect of accommodation coefficients on the maximum flow rate. We analyze the steady-state flow rates for Kn = 0.03 and 0.05 with $\alpha = 0.5$. Figure 3.11 shows the result of q_{max}/q_0 vs. $\Delta T/T_0$ with $\alpha = 0.5$ and 1.0. The effect of the accommodation coefficient on the maximum mass flow rate is not very large even for a large variation of the accommodation coefficient. These results, showing no effect of the accommodation coefficient on the flow rate, are consistent with the properties of RP obtained in Sec. 2.5.3.2.

3.4.2 The compression ratio

Initial conditions are given as static equilibrium. The time variation of the pressure distribution is calculated, and the maximum compression ratio obtained for one element is analyzed.

We present the results for the compression ratio of the pump described in Sec. 3.2.2.2. Firstly we show an example of the steady-state pressure distribution, $\bar{p}_{\text{final}}(X_1)$ [defined in Eq. (3.2) below] for $\text{Kn} = 0.03, \Delta T/T_0 = 2.0$ with $\alpha = 1.0$ in Fig. 3.12. The pressure gradient occurs only at the channel part, and the pressure is uniform at the tank-L side and the tank-R side. Therefore, we can define the average pressure on the low-temperature side $\langle\bar{p}\rangle_{\text{low}}$ and that on the high-temperature side $\langle\bar{p}\rangle_{\text{high}}$ by

$$\langle\bar{p}\rangle_{\text{low}} = \frac{1}{30D}\int_{\text{tank-L}} \bar{p}_{\text{final}}(X_1)\,\mathrm{d}X_1,$$
$$\langle\bar{p}\rangle_{\text{high}} = \frac{1}{30D}\int_{\text{tank-R}} \bar{p}_{\text{final}}(X_1)\,\mathrm{d}X_1.$$

The compression ratio $\gamma_{\max}$ is defined by

$$\gamma_{\max} = \frac{\langle\bar{p}\rangle_{\text{high}} - \langle\bar{p}\rangle_{\text{low}}}{\langle p\rangle}, \tag{3.1}$$
$$\langle p\rangle = \frac{\langle\bar{p}\rangle_{\text{high}} + \langle\bar{p}\rangle_{\text{low}}}{2}.$$

Long computation times are required to obtain the compression ratio results. We show an example of the approach to the steady-state from the uniform initial state in the numerical model shown in Fig. 3.4. Figure 3.13 is the distribution of the pressure $\bar{p}$ averaged over the cross-section. The distributions at $t/t_0 = 500$, 1500, 3000, 6000, and 8000 for the case of $\text{Kn} = 0.03$ and $\Delta T/T_0 = 2$ are shown in the figure. In these figures, we plot the time average of $\bar{p}$

$$\frac{1}{500t_0}\int_{t-500t_0}^{t} \bar{p}(\tau,\, X_1)\,\mathrm{d}\tau.$$

The process takes a long time. Since we do not observe the difference of the distribution of $\bar{p}$ between $t/t_0 = 6000$ and 8000, we define

$$t_e = 8000t_0,$$

as the time t_e required to establish the steady-state. At the steady-state, there is a pressure difference between $X_1/D = -60$ and $X_1/D = 90$. The steady profile $\bar{p}_{\text{final}}$ is calculated by a long time average. That is,

$$\bar{p}_{\text{final}}(X_1) = \frac{1}{1500t_0}\int_{t_e-1500t_0}^{t_e} \bar{p}(\tau,\, X_1)\,\mathrm{d}\tau. \tag{3.2}$$

We calculate $\bar{p}_{\text{final}}$ for $\text{Kn} = 0.03$ and 0.05 for two accommodation coefficients $\alpha = 0.5$ and 1. The calculation for each pair of (Kn, α) is done for several values of the temperature difference ratio $\Delta T/T_0$.

Figure 3.14 shows $\gamma_{\max}$ vs. $\Delta T/T_0$ for each pair of (Kn, α). In contrast to the maximum flow rate shown in Fig. 3.11, the compression ratio depends much on the accommodation coefficient: the compression ratio decreases to around $50\,\% \sim 70\,\%$ by changing α from 1 to 0.5. These results that there is accommodation coefficient effect on the compression ratio are consistent with the properties of RP obtained in Sec. 2.5.4.

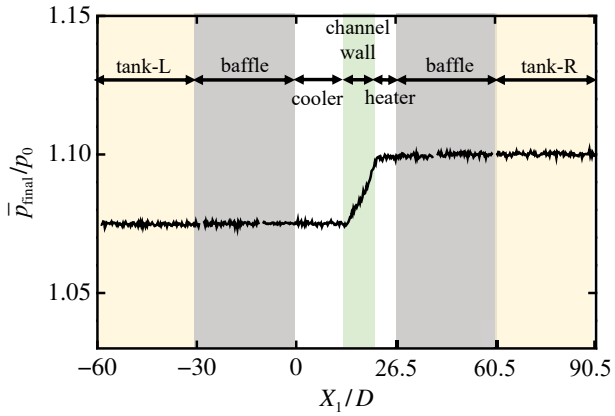

Figure 3.12: $\bar{p}_{\mathrm{final}}(X_1)$ of the case Kn = 0.03 and $\Delta T/T_0 = 2.0$. Discontinuous areas of graph are baffle areas.

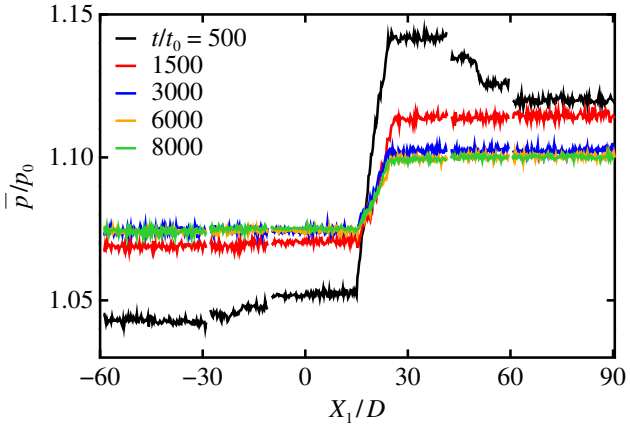

Figure 3.13: Time evolution of $\bar{p}$ for the case of Kn = 0.03 and $\Delta T/T_0 = 2$.

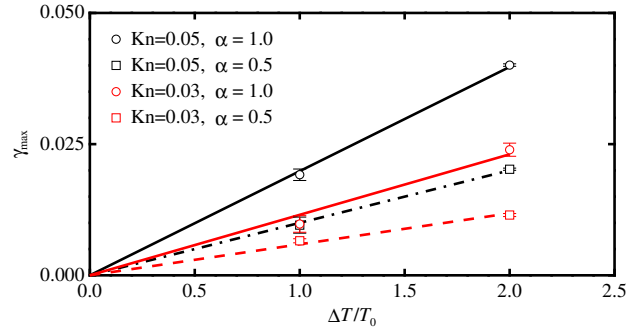

Figure 3.14: Maximum compression ratio γ_{max} (Kn = 0.03 and 0.05, $\alpha = 0.5$ and 1.0).

Table 3.1: The coefficients (C_1, C_2) of quadratic regression curves for Kn = 0.03, 0.05, 1, and 10.

Kn	C_1	C_2
0.03	$6.96 \times 10^{-4} \pm 3.35 \times 10^{-5}$	$-1.7 \times 10^{-4} \pm 5.8 \times 10^{-5}$
0.05	$1.02 \times 10^{-3} \pm 3.68 \times 10^{-5}$	$-1.8 \times 10^{-4} \pm 6.3 \times 10^{-5}$
1	$5.73 \times 10^{-3} \pm 2.14 \times 10^{-4}$	$-8.0 \times 10^{-4} \pm 3.7 \times 10^{-4}$
10	$4.35 \times 10^{-3} \pm 6.10 \times 10^{-5}$	$-6.0 \times 10^{-4} \pm 1.0 \times 10^{-4}$

Table 3.2: Estimated value of volumetric flow rate under the experimental condition: Kn = 0.03.

Kn	volumetric flow rate [sccm/mm^2]
0.03	3.02 ± 0.20

3.5 Discussion

3.5.1 Comparison with experimental results

This section explains the experimental results of the volumetric flow rate and the pressure difference obtained by the pump in [76] by our numerical results obtained in Secs. 3.4.1.2 and 3.4.2. Since the temperature difference under the experimental conditions is too small to compute directly, an approximate curve is calculated. As shown in Fig. 3.9, the relationship between q_{max}/q_0 and the non-dimensional temperature difference $\Delta T/T_0$ looks quadratic. The coefficients C_1 and C_2 of the expression

$$q_{max}/q_0 = C_1 \left(\Delta T/T_0\right) + C_2 \left(\Delta T/T_0\right)^2,$$

are shown in Tab. 3.1. Here, we assume that $q_{max}/q_0 = 0$ at $\Delta T/T_0 = 0$. In addition, the flow rate is assumed to be independent of the accommodation coefficient. Note that q_{max}/q_0 does not depend on the accommodation coefficient α. Thus we can estimate the value of the volumetric flow rate of air at the atmospheric pressure from q_{max} at $\Delta T/T_0 \approx 0.167$, which is the condition considered in [76]. The results are compared with the experimental results by multiplying the results obtained for a single channel by the number of channels assumed from the total area of the pump . In this case, the effect of the end of the pump is neglected.. The estimated results are shown in Tab. 3.2. Using the data for the viscosity coefficient viscosity μ [Eq. (2.9)] at the atmospheric pressure (see, e.g., NIST database [81]), Kn for experiment condition is determined to be 0.03.

Since the experiment in [76] by An et al. reports that the flow rate is 2.9 [sccm/mm^2], the value of Kn = 0.03, which is estimated using the hard-sphere model, is plausible and explains the result within an error.

The experimental result for the pressure difference is also explained by the Knudsen number Kn = 0.03. Using the result of Fig. 3.14 and assuming that the maximum compression ratio $\gamma_{\max} = 0$ when $\Delta T = 0$, we calculate the relationship between ΔT and $\gamma_{\max}$ for each

Table 3.3: Maximum pressure difference $\Delta p_{\max}$ under the experimental condition: Kn = 0.03.

Kn	α	$\Delta p_{\max}$ (kPa)
0.03	1.0	0.1947
0.03	0.5	0.09977

pair of (Kn, α) using the least-squares method. By substituting the experimental condition $\Delta T/T_0 = 0.167$ into the relationship, the maximum pressure difference $\Delta p_{\max}$ obtained under atmospheric pressure is calculated. Tab. 3.3 shows the results. The maximum pressure difference obtained in the experiment by An et al. is 0.137 (kPa) in [76]. This value of pressure difference is possible in the range of the accommodation coefficient

$$0.5 \leq \alpha \leq 1,$$

for Kn = 0.03.

Finally, for reference, we compare other experimental results reported in [76] and numerical results. The experimental condition for comparison is $\Delta T/T_0 = 0.25$, assuming that the results of CFD analysis under ambient pressure by An et al. are equally applicable for several Kn numbers. The regression curves for Kn = 0.05 and 1, and 10 are calculated by the least squares method in the same way as for Kn = 0.03 calculated earlier. From the obtained regression curves, the flow rate at dimensionless temperature difference $\Delta T/T_0 = 0.25$ at each Kn number is estimated. These estimated values are compared with the experimentally reported flow rates [sccm] in Fig. 3.15. The Kn number for the experimental conditions is estimated from the conversion of pressure ratios. This suggests that the results of our analysis and the experimental results are estimated to be in the neighborhood of a single curve. This may suggest that the numerical calculations of maximum flow in this study seem to reproduce the experimental results; however, there are still many remaining points to be considered. For example, the experiments are performed in air, a mixture of diatomic molecular gases, while the numerical analysis uses the hard sphere molecular gas. Neither theoretical compensation nor experimental results have yet confirmed that the behavior of both gases is identical in this case. The number of channels in the experimental apparatus is estimated to be about 2.4×10^4, but in fact there will be some influence of the outer surface of the apparatus, which is neglected in our estimation.

In summary, although there are still many points to be considered, this study is a first step toward future comparative studies with more detailed experimental results.

3.5.2 Validity of cell size

In Chapter 2, only the mean values are used to investigate the basic properties, while in Chapter 3, in order to make a quantitative comparison, a study on cell size is conducted to take into account the variability of the DSMC results. The Knudsen numbers we compute are small and the flows they produce are slow. Such cases are difficult to deal with using the DSMC method. Therefore, it is necessary to keep the cell size as small as possible and

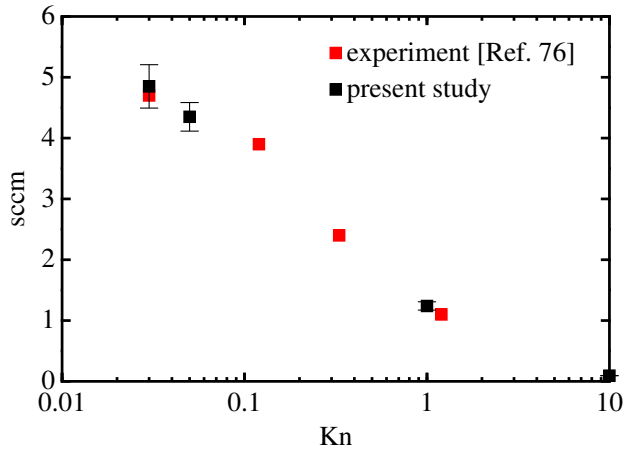

Figure 3.15: Comparison of numerical analysis and experimental results in [76].

Table 3.4: Steady-state dimensionless flow rate for two cell sizes. The case of Kn = 0.03, $\Delta T/T_0 = 2$ and $\alpha = 1$.

dX_1/D	dX_2/D	dX_3/D	$(q_{max}/q_0 \pm 3\sigma) \times 10^4$
0.25	0.125	0.25	6.89 ± 0.62
0.25	0.0625	0.25	7.19 ± 0.40

the number of particles as large as possible within the range that can be calculated with the current computer resources. The validity of the cell size used in the DSMC calculation (cf. Sec. 3.3)

$$(dX_1,\, dX_2,\, dX_3) = (0.25D,\, 0.125D,\, 0.25D)$$

is tested with the maximum flow rate (Sec. 3.4.1.2). For example, the case where dX_2 is halved is performed for the case of Kn = 0.03, $\Delta T/T_0 = 2$, and $\alpha = 1$. The number of particles per cell is 2000. We summarize q/q_0 at steady-state and the three times standard deviation $\pm 3\sigma$ of the data in Tab. 3.4. One may find a slight increase of q_{max}/q_0 for small dX_2, but its variation is of the order of 3σ of the fluctuation of the DSMC result, which does not disturb the discussion in the following section. In addition to this case, we also checked the results of changing the cell size in the same way and confirmed that the solutions overlap when error bars are included. Therefore, the size of the cell would be enough for the present purpose. To clarify the effect of the cell size, one must use a more intensive number of simulation particles.

We add a note on the effect of the molecular model. We also calculated the maximum flow rates of the pump with N_2 using the variable hard-sphere (VHS) model [69]. However, the differences from the corresponding results of the hard-sphere model are within the fluctuation of the DSMC procedure.

3.6 Concluding remarks

A three-dimensional numerical model is constructed to calculate the practical MEMS RP that is manufactured and tested in [76]. The direct numerical calculation reveals the distribution of internal macroscopic quantities. These results provide many findings, such as flow obstruction caused by the heater, which will be helpful for future design improvements.

The maximum flow rate obtained by the pump is estimated under the same conditions as in the experiment, and the results are consistent with the reported experimental results. When the maximum flow rate is analyzed, the effect of accommodation coefficient is not pronounced. On the other hand, the effect of accommodation coefficient appears in the maximum pressure ratio. These results are also consistent with the properties of RP obtained in Chapter 2. The pressure difference is compared with the experimental results. From the results of the computations with different accommodation coefficients, it is possible to estimate the accommodation coefficients of the experimental apparatus. The results are consistent with the value of the general accommodation coefficient.

The calculations performed here are not a complete reproduction of the experiment. In fact, the gas is calculated with a hard sphere model, whereas the actual air is a mixture of diatomic molecular gases. The temperature distribution on the wall obtained in [76] is also obtained by CFD analysis at the atmospheric pressure. It is assumed that this temperature distribution does not change regardless of Kn. However, at least the results of this study do not significantly differ from the experimental results and are a prosperous first step in analyzing the performance of an actual pump by numerical simulation.

Chapter 4

New driving principle of thermally driven micro devices [68]

4.1 Introduction

In Chapters 2 and 3, we carried out the DSMC computations of rarefied gas flows in RP and KP on the basis of the Boltzmann equation. These pumps require temperature gradients along solid bodies and the resulting thermal transpiration flows act their driving force. These temperature gradients are maintained by supplying steady heat flows through solid boundaries from the outside. Various proposals have been made to improve the efficiency of thermally driven rarefied gas flow pumps [57, 65, 82]. Thermal edge flow pumps [55, 57] has attracted interests because of its high efficiency and performance since it has constant temperature solid bodies and it does not accompany with heat flows in solid bodies, which is considered as the main factor of energy loss. However, its staggered structure is not easy to produce as MEMS at present. Ratchet pump mentioned in Sec. 1.2.3 has also attracted attentions recently as a MEMS pumping device [65, 82]. It consists of two plates of different constant temperatures and each plate has zigzag structure with vertical and oblique surfaces. It is confirmed by DSMC computation that the variation of accommodation coefficient synchronous to the surface angle variation induces flows around the corners of the zigzag plates, resulting in a one-way flow. It is, however, difficult to make zigzag molphorogy as MEMS. For this reason, experimental validation of such Ratchet MEMS pump has not yet been made so far. In this chapter, we propose a new MEMS pump utilizing one-way flows induced between two parallel "flat" plates by non-uniformity of accommodation coefficient.

4.2 Plan of computation

Consider a rarefied gas between two parallel infinite plates A and B with different uniform temperatures [Fig. 4.1]. Let the plate A be located at $X_2 = D$ and let the plate B be done at $X_2 = 0$, where X_i $(i = 1, 2, 3)$ are the Cartesian space coordinates, and let the temperature of the plate A and that of the plate B be denoted by T_0 and T_1, respectively. When the accommodation coefficient α of plate A and that of B are uniform, no mass flow is induced between the plates and the problem is reduced to the heat conduction. We

show the occurrence of one-way flow between them by the non-uniformity of accommodation coefficient of each plate. We assume that the distribution of accommodation coefficient is periodic with respect to the X_1 direction. We consider the variation of α with the period $2L$. The value of α is α_L for the half period and α_R for the rest of the period where α_L and α_R are constants. We investigate the following two cases:

(Case 1) While the above mentioned distribution of the accommodation coefficient is applied to the plate B, the uniform distribution $\alpha = 1$ is done to the plate A (diffuse reflection) [see Fig. 4.1(a)].

(Case 2) The above mentioned distribution of the accommodation coefficient is applied to the plate A and the plate B but there is a difference in phase between these periodic distributions; the phase difference is denoted by H [see Fig. 4.1(b)].

In Case 1, because of the symmetry, a one-way flow in the X_1 direction is not expected to occur, but it is not clear what kind of flow field is induced. Therefore, we investigate the flow field that is induced there. In Case 2, when symmetry is broken due to the phase difference H, there is a possibility that one-way flow occurs. The analysis of the flow field in this case is the main interest of this study.

Knudsen number l_o/D, dimensionless temperature difference between the plate A and B $\Delta T/T_0 = (T_1 - T_0)/T_0$, accommodation coefficients of the plate (α_L, α_R), the aspect ratio of the domain L/D, and the dimensionless phase difference H/L are the parameters that characterize the problem. l_o is the mean free path of the hard sphere model corresponding to the mean density.

4.3 Numerical settings

In Case 1, the symmetry is used to compute in the blue region shown in Fig. 4.1. The computational domain is $0 < X_1 < L$ and $0 < X_2 < D$. For plate A, the accommodation coefficients are uniform; $\alpha = 1$. For plate B, $0 < X_1 < L/2$ is α_L and $L/2 < X_1 < L$ is α_R. In Case 2, Case 2 is periodic, so the blue area shown in Fig. 4.1 is calculated given the periodic condition. The computational domain is $0 < X_1 < 2L$ and $0 < X_2 < D$. For plate A, $0 < X_1 < L$ is α_L and $L < X_1 < 2L$ is α_R. For plate B, when $H < L$, $0 < X_1 < L - H$ and $2L - H < X_1 < 2L$ are α_L and $L - H < X_1 < 2L - H$ is α_R. When $L < H$, $0 < X_1 < 2L - H$ and $3L - H < X_1 < 2L$ are α_R and $2L - H < X_1 < 3L - H$ is α_L. We show here the parameters of the DSMC method mentioned in Sec. 2.3.1. The time step is $\Delta t = 0.001 t_0$. The cell size is $(\mathrm{d}X_1, \mathrm{d}X_2) = (0.01D, 0.01D)$. Each cell contains 2000 simulation particles.

4.4 Results and discussions

4.4.1 Case1

4.4.1.1 Array of rolls

To explain the occurrence of the gas flow, we present the steady-state for Kn = 0.1, $\Delta T/T_0 = 2.0$, $(\alpha_L, \alpha_R) = (0.5, 1.0)$, and $L/D = 1.0$. Figure 4.2 shows the time evolution of the temperature field from the initial state. The black rectangle in the upper of the figure

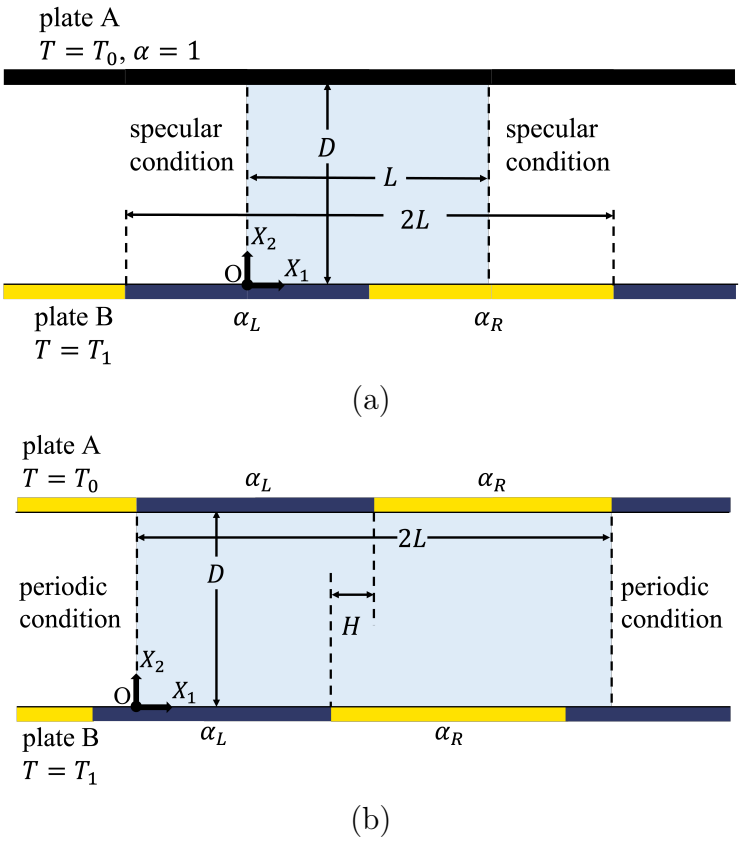

Figure 4.1: Schematic of the geometry. (a) : Case 1. Only the plate B has periodic distribution of accommodation coefficient. The navy rectangle represents α_L area, and the yellow rectangle represents α_R area. The black rectangle indicates the diffuse reflection condition. (b) : Case 2. Both plates have periodic distribution of accommodation coefficient. This case has a new parameter : the phase difference of the discontinuity point H. The meaning of the colored rectangle is the same as in (a); note that the two flat plates have different constant temperatures, the temperature of plate A is T_0 and that of plate B is T_1.

represents plate A, the navy rectangle in the lower of the figure represents the plate B with the accommodation coefficient $\alpha = \alpha_L$, and the yellow rectangle represents the plate B with $\alpha = \alpha_R$. The figure is colored according to the gas temperature, with the figure colored red for temperatures closer to $T/T_0 = 3.0$ and blue for temperatures closer to $T/T_0 = 1.0$. The temperature field evolves from the initial stationary equilibrium state, Eq. (2.12). At the initial state [Fig. 4.2(a)], the temperature of the gas is the same as the temperature of plate A, T_0, and as time passes, the energy of the plate B is transferred into the gas, and nonuniform temperature distribution is formed [Figs. 4.2(b), (c), (d)]. A steady-state arises at a dimensionless time $t/t_0 = 10$ [Figs. 4.2(e), (f)]. At the steady-state, the temperature of the gas near the part of higher accommodation coefficient α_R (indicated by the yellow rectangle) is closer to the temperature of the plate B, $T_1/T_0 = 3.0$, than that near the part of lower accommodation coefficient α_L (the navy rectangle).

The distributions of the macroscopic quantities at the steady-state are shown in Fig. 4.3. Panel (a) shows the temperature distribution of the gas with the arrows showing the flow

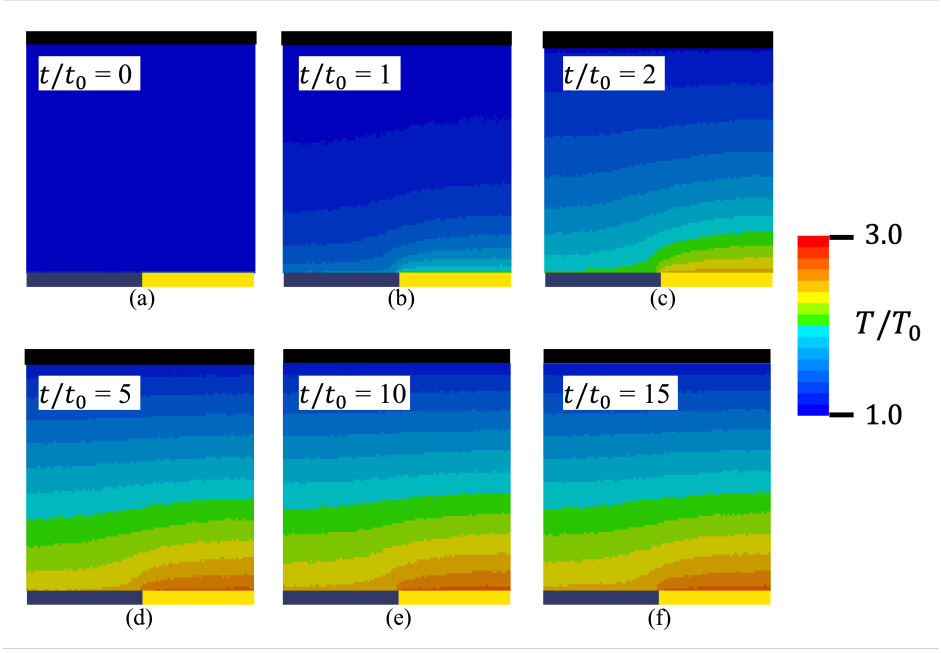

Figure 4.2: Time evolution of the temperature field. Non-dimensional time t/t_0 = (a) 0, (b) 1, (c) 2, (d) 5, (e) 10, and (f) 15. The case for Kn = 0.1, $\Delta T/T_0 = 2.0$, $(\alpha_L, \alpha_R) = (0.5, 1.0)$, and $L/D = 1.0$. See Fig. 4.1 for the meaning of the colored rectangles.

velocity vectors, (b) shows the pressure, and (c) shows the number density, respectively. The dimensionless time used for the time-average is $10 \leq t/t_0 \leq 110$.

From Fig. 4.3(a), a roll flow occurs in the domain. The flow speed is large at the discontinuity point of accommodation coefficient, where the gaseous temperature varies in the X_1 direction. The direction of the flow is the same as that of thermal transpiration flow (from cold gas side to hot gas side). This flow produces a counterclockwise vortical flow over the entire region in the figure. Fig. 4.3(b) shows the gas pressure distribution in colors. The distribution shows low pressure in the lower left of the computational domain and high pressure in the lower right. Figure 4.3(c) shows the number density distribution of the gas. The number density increased in the vicinity of the plate A. As the accommodation coefficient changes, the number density also changes in the direction along the flat B.

The analysis is performed by varying Knudsen number. Fig. 4.4 shows the results of the steady-state temperature and velocity fields averaged over $100t_0$ for Kn = 0.05, 0.125, 0.2, 0.5, 1, and 10. The color-coding of the temperature distribution and the magnitude criterion of the velocity vectors are the same for all cases. As Knudsen number decreases, the gaseous temperature variation along with plate B increases. As Knudsen number increases, the temperature variation along the wall decreases and almost vanishes at Kn = 10. The flow velocity at Kn = 10 is too small and it is almost invisible in the figure.

A 10-fold magnification of the velocity vector for Kn = 10 is shown in Fig. 4.5. As can be seen, the roll flow is almost non-existent and is buried in the fluctuation of the DSMC method. Therefore, to evaluate the existence of single roll flow, it is necessary an indicator to evaluate the magnitude of the flow generated in Case 1. The properties required of the

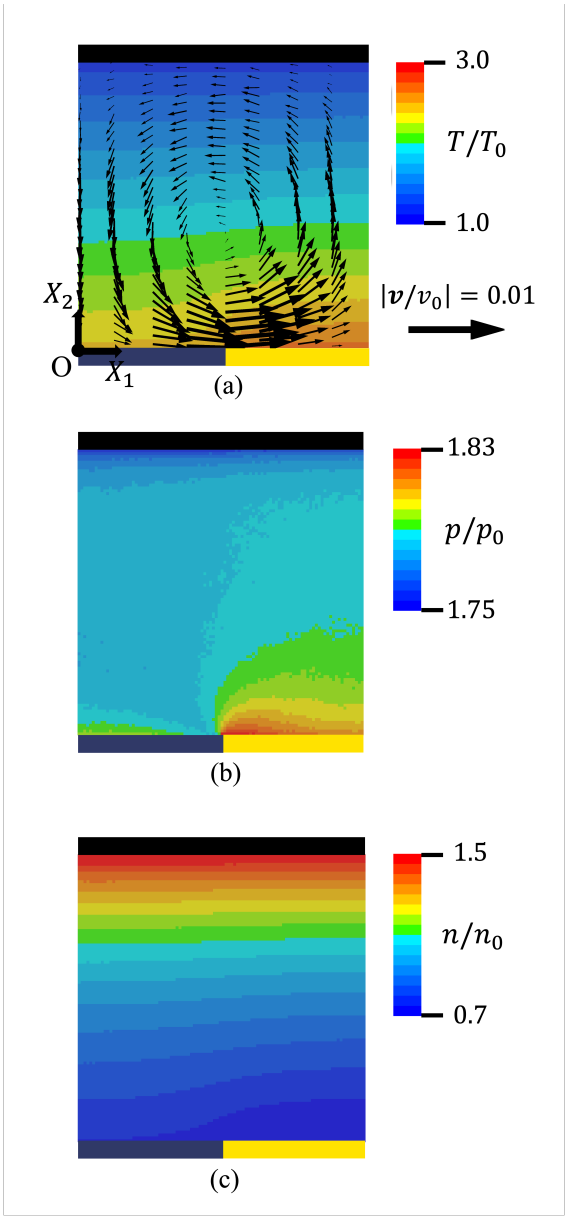

Figure 4.3: Distribution of (a) temperature and flow velocity, (b) pressure, and (c) number density, at steady-state. In panel (a), the flow velocity at each point is indicated by the black arrows starting there. The reference size is shown at the lower right corner of the panel. The case for Kn $= 0.1$, $\Delta T/T_0 = 2.0$, $(\alpha_L, \alpha_R) = (0.5, 1.0)$, and $L/D = 1.0$.

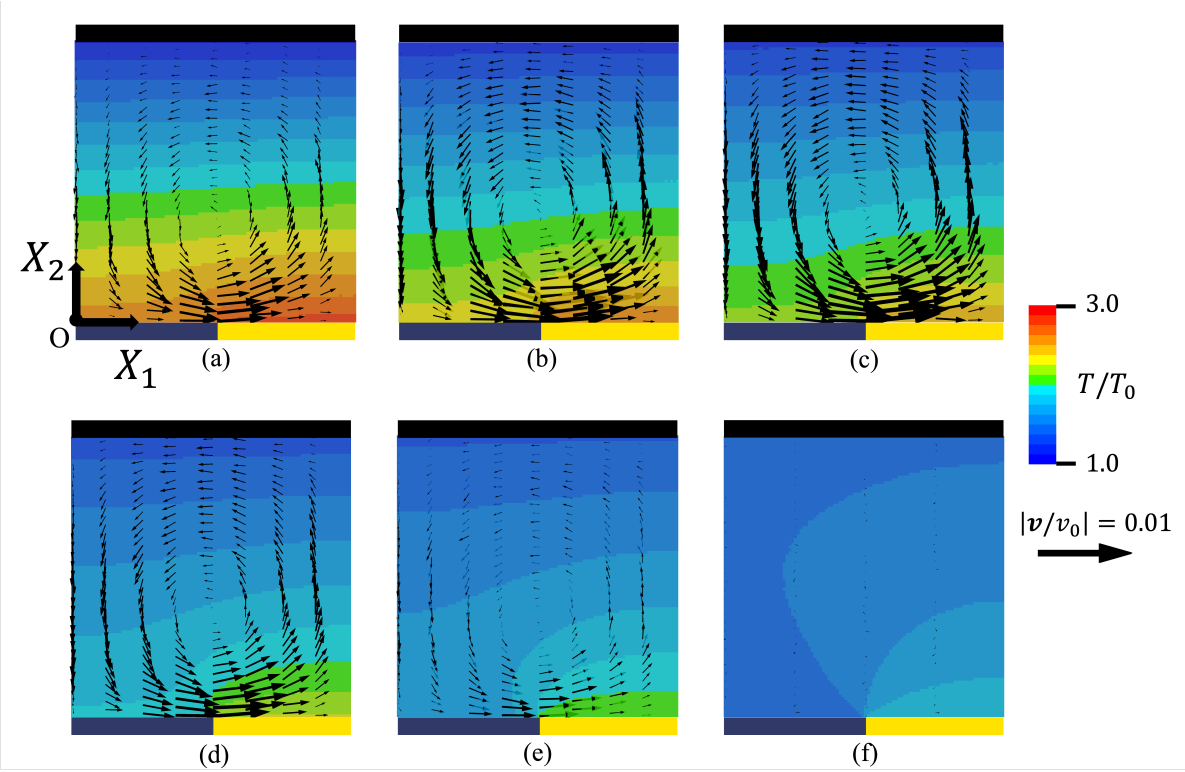

Figure 4.4: Temperature and velocity fields at steady-state for various Knudsen numbers. The Knudsen number Kn = (a) 0.05, (b) 0.125, (c) 0.2, (d) 0.5, (e) 1, and (f) 10. The case for $\Delta T/T_0 = 2.0$, $(\alpha_L, \alpha_R) = (0.5.\, 1.0)$, and $L/D = 1.0$.

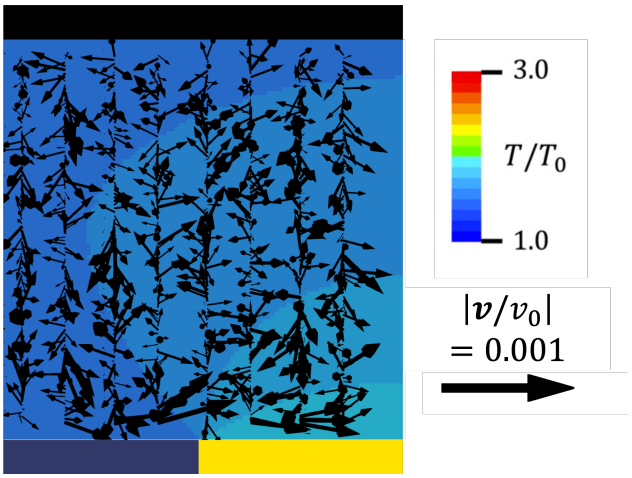

Figure 4.5: Temperature and velocity fields at steady-state for Kn = 10. The results shown in this figure are the same as in Fig. 4.4 (f), but with the velocity vector scaled up 10 times.

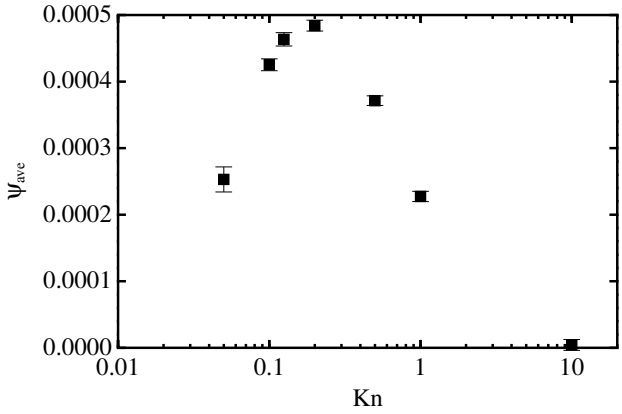

Figure 4.6: The domain average of the stream function ψ_{ave} vs Knudsen numbers. $\Delta T/T_0 = 2.0$, $(\alpha_L,\, \alpha_R) = (0.5.\, 1.0)$, and $L/D = 1.0$.

indicators used here are that it should be able to determine the direction of the roll, that it should disappear when no roll flow is observed, and that it should have many average times in order to reduce DSMC fluctuations. Thus, in this study, we use the domain average of the flow function as the indicator.

The average value of the stream function ψ is defined by

$$\begin{aligned}\psi\left(X_1, X_2\right) =& \int_0^{X_1} \frac{n\boldsymbol{v}\cdot\boldsymbol{n}\left(x,0\right)}{n_0 v_0 D}\mathrm{d}x + \int_0^{X_2} \frac{n\boldsymbol{v}\cdot\boldsymbol{n}\left(X_1,y\right)}{n_0 v_0 D}\mathrm{d}y \\ =& \frac{1}{n_0 v_0 D}\int_0^{X_2} n v_1\left(X_1,\, y\right)\mathrm{d}y. \end{aligned} \tag{4.1}$$

Here, $\boldsymbol{n}$ is the normal unit vector pointing to the right of the path of the integral. That is, $\boldsymbol{n}\left(x,\, 0\right) = (0, -1)$ and $\boldsymbol{n}\left(X_1,\, y\right) = (1,\, 0)$. The last equality comes from $\boldsymbol{v}\cdot\boldsymbol{n_w} = 0$ and $\boldsymbol{n}\left(x,\, 0\right) = -\boldsymbol{n}_w$ $(0 < x < L)$. Clearly the value of ψ increases along with X_2 where the flow is rightward $(v_1 > 0)$ and decreases vise versa. In the case of the counterclockwise roll flow shown in Fig. 4.3, the value of $\psi\left(X_1, X_2\right)$ first increases with X_2 and takes positive values since $\psi = 0$ on $X_2 = 0$. Then it decreases and vanishes as $X_2 \to D$. Thus, the average value

$$\psi_{ave} = \frac{1}{LD}\int_{0<X_1<L,\, 0<X_2<D} \psi\left(X_1, X_2\right)\mathrm{d}dX_1\mathrm{d}dX_2 \tag{4.2}$$

become positive. Note that the vanishing of this value is not equivalent to the absence of flow. The calculation method for each point is as follows.

To investigate the effect of the Knudsen number, we plot ψ_{ave} for Kn = 0.05, 0.1, 0.125, 0.2, 0.5, 1, and 10. Figure 4.6 shows the results. It can be seen that the stream function peaks around Kn ~ 0.2. The error bars are the standard error σ multiplied by 3 for the ten data points and indicate the range of $\pm 3\sigma$ from the mean value.

Here, we attempt a physical interpretation of how non-uniformity of accommodation coefficient induces the flow. First, in the present case, the temperature of the flat plate is uniform, but the accommodation coefficients are different at locations. Now we are considering a flat

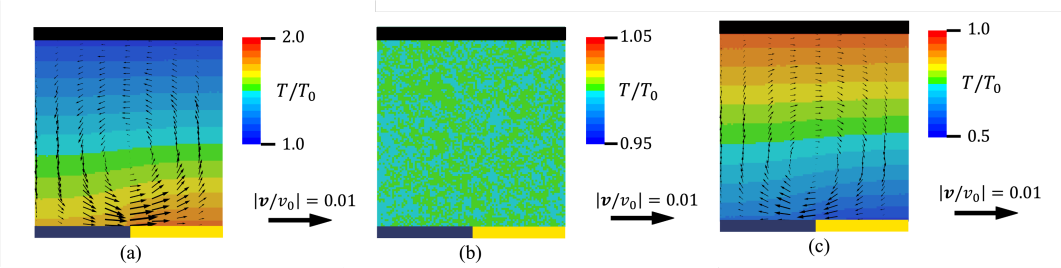

Figure 4.7: Temperature and velocity fields at steady-state for various temperature differences. (a) $\Delta T/T_0 = 1.0$, (b) $\Delta T/T_0 = 0.0$, and (c) $\Delta T/T_0 = -0.5$. The case for Kn $= 0.1$, $(\alpha_L, \alpha_R) = (0.5, 1.0)$, and $L/D = 1.0$.

plate at a high temperature, molecules reflected at locations with high accommodation coefficients will be reflected faster, on average, than those with low accommodation coefficients. Therefore, when molecules reflected from the wall collide again with other gas molecules near the flat plate, the temperature of the gas near the location where the accommodation coefficient is high becomes hotter than that near the location where the accommodation coefficient is low. Thus, when gas molecules near the wall are directly incident on the wall, they enter as high-speed molecules from the side with high accommodation coefficients and low-speed molecules from the side with low accommodation coefficients. Similar to the physical interpretation of thermal creep flow mentioned in Sec. 1.2.1, flow occurs from the low accommodation coefficient side to the high accommodation coefficient side at this time. In this mechanism, the critical point is that molecules reflected from the wall surface collide with other molecules in the neighborhood of the wall surface, and then re-enter the wall surface directly. Therefore, if Kn is too low, the temperature of the gas becomes uniform near the wall surface and there is no velocity difference between the incident molecules. On the other hand, if Kn is too large, collisions between molecules do not occur, and molecules reflected from the low-temperature side wall enter the other wall directly. In such cases, flow by the previous mechanism does not occur. Figure 4.6 shows that the flow peak appears near Kn ~ 0.2 when the plate spacing is taken as the representative length. This is also observed in Fig. 4.4, where the flow velocity vector is large at Kn $= 0.125$ and 0.2.

4.4.1.2 Effect of the temperature difference between the flat plates

We investigate the effect of the non-dimensional temperature difference between the two plates $\Delta T/T_0$. Figure 4.7 shows the steady-state temperature and velocity fields for $\Delta T/T_0 =$ 1.0, 0.0, and -0.5. Figure 4.8 shows the relationship between ψ_{ave} and temperature difference $\Delta T/T_0$. Compared to Fig. 4.3(a), the flow becomes weak as $\Delta T/T_0$ decreases and disappears. When the temperature of the plate B becomes lower, the vortical flow reappears, but its direction becomes clockwise.

4.4.1.3 Effect of the accommodation coefficient difference

We investigate the effect of accommodation coefficient (α_L, α_R). The results are shown in Figs. 4.9 and 4.10. Figure 4.9 shows the temperature and velocity fields at steady-state

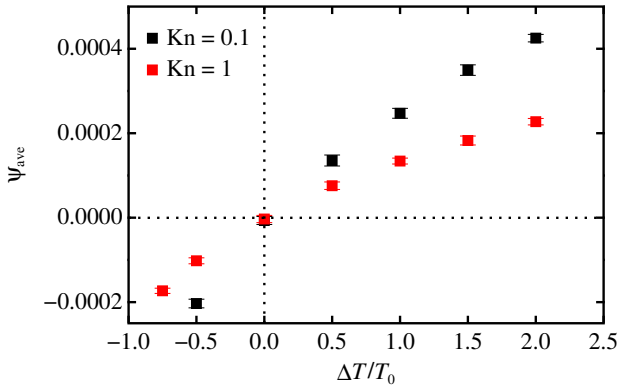

Figure 4.8: The domain average of the stream function vs $\Delta T/T_0$ for Kn $= 0.1$ and 1.0, $(\alpha_L, \alpha_R) = (0.5, 1.0)$, and $L/D = 1.0$.

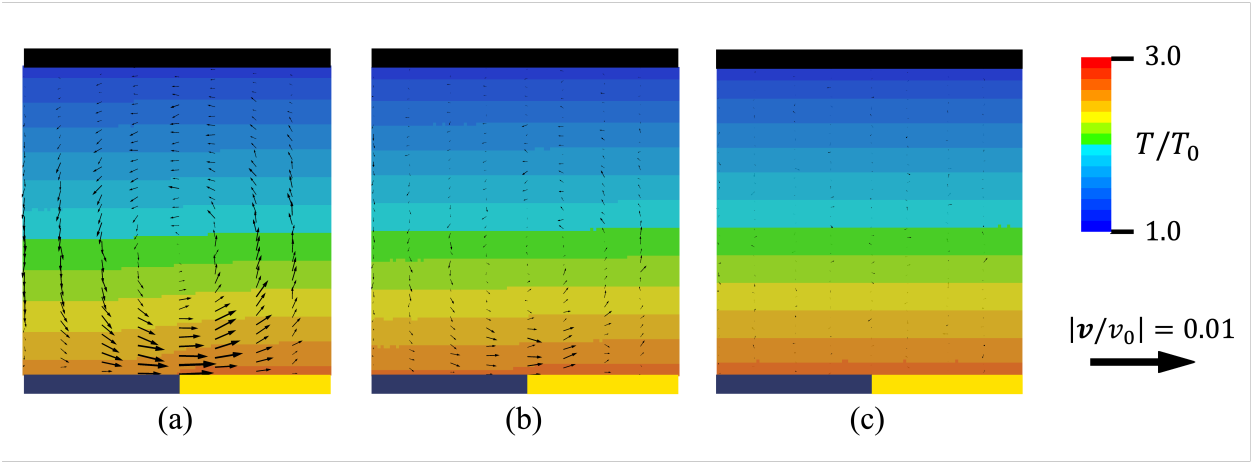

Figure 4.9: Temperature and velocity fields at steady-state for various accommodation coefficients. (a) $(\alpha_L, \alpha_R) = (0.75, 1.0)$, (b) $(\alpha_L, \alpha_R) = (0.9, 1.0)$, and (c) $(\alpha_L, \alpha_R) = (1.0, 1.0)$. The case for Kn $= 0.1$, $\Delta T/T_0 = 2.0$, and $L/D = 1.0$.

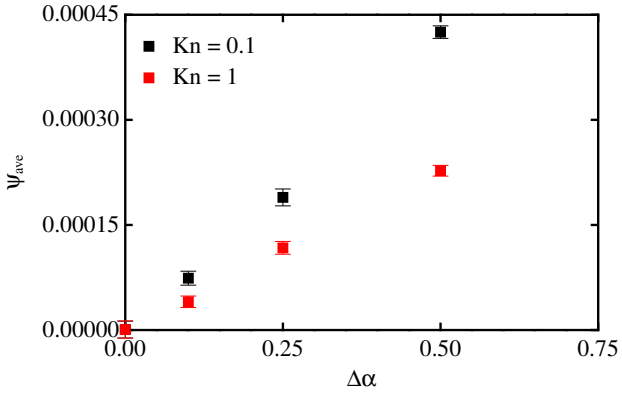

Figure 4.10: The domain average of the stream function vs $\Delta\alpha = \alpha_R - \alpha_L$ for Kn $=$ 0.1 and 1.0, $\Delta T/T_0 = 2.0$, and $L/D = 1.0$.

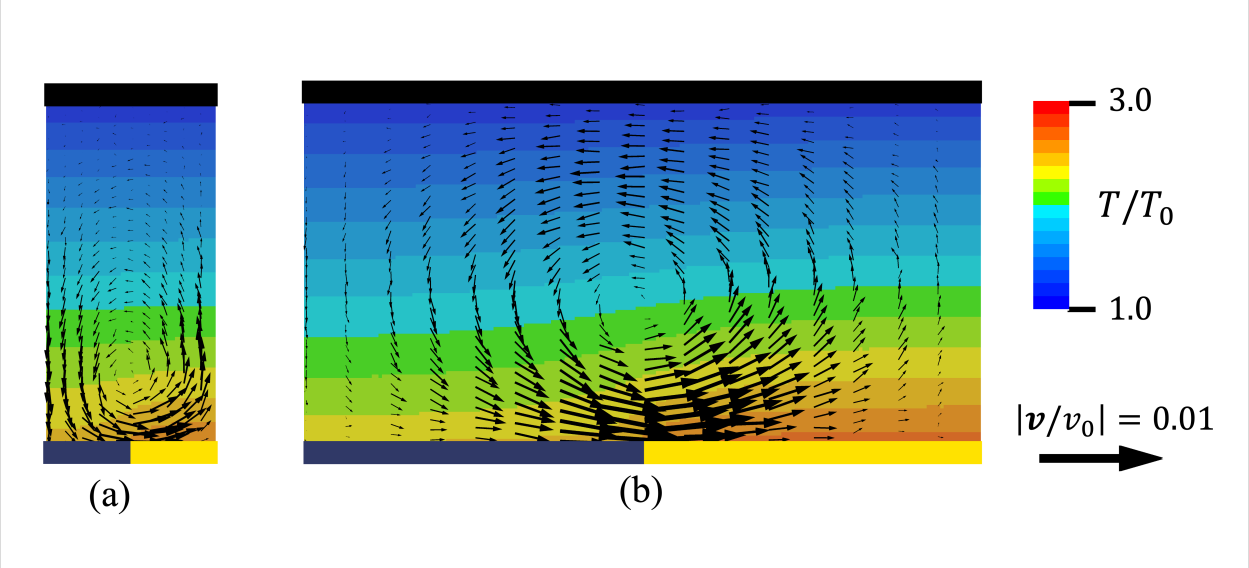

Figure 4.11: Temperature and velocity fields for various aspect ratios. (a) $L/D = 0.5$ and (b) $L/D = 2.0$. The case for Kn $= 0.1$, $\Delta T/T_0 = 2.0$, and $(\alpha_L, \alpha_R) = (0.5, 1.0)$.

for $(\alpha_L, \alpha_R) = (0.75, 1.0)$, $(0.9, 1.0)$, and $(1.0, 1.0)$. Figure 4.10 shows ψ_{ave} for Kn $=$ 0.1 and 1.0 for various $\Delta\alpha$. There is no change in the flow direction, but as the difference in accommodation coefficients becomes small, the flow becomes weak. Also, $(\alpha_L, \alpha_R) =$ $(1.0, 1.0)$ [Fig. 4.9(c)], where $\Delta\alpha = \alpha_R - \alpha_L = 0$, the isothermal lines become parallel to the plates A and B. Therefore, the temperature is uniform along the wall, and no roll flow is induced. This result indicates that the difference in accommodation coefficients is essential for the roll flow.

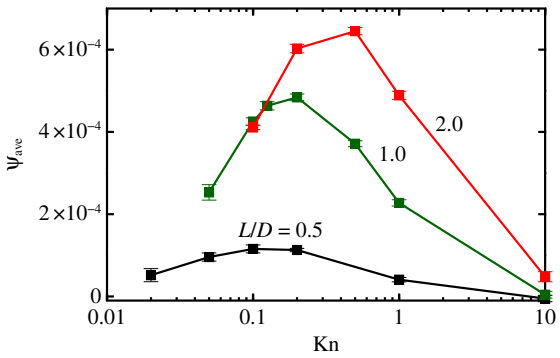

Figure 4.12: The domain average of the stream function vs Knudsen numbers for $L/D =$ 0.5, 1.0, and 2.0. The result of $L/D = 1.0$ is already shown in Fig. 4.6. $\Delta T/T_0 = 2.0$ and $(\alpha_L, \alpha_R) = (0.5, 1.0)$

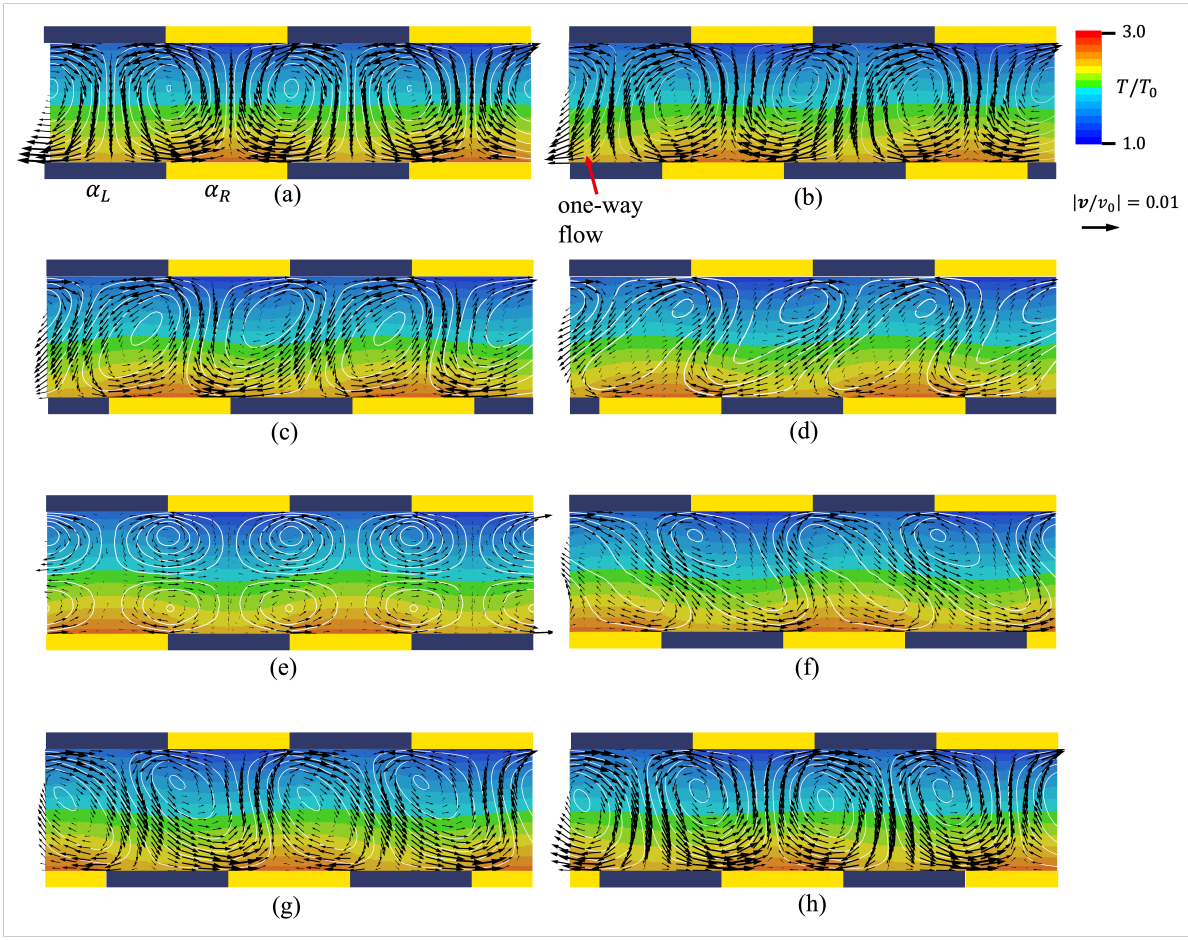

Figure 4.13: Temperature and velocity fields for various phase differences. White lines are the contour of the stream function. $H/L =$ (a) 0 or 2.0, (b) 0.25, (c) 0.5, (d) 0.75, (e) 1.0, (f) 1.25, (g) 1.5, and (h) 1.75. The case for Kn $= 0.1$, $\Delta T/T_0 = 2.0$, $(\alpha_L, \alpha_R) = (0.5, 1.0)$, and $L/D = 1.0$. See Fig. 4.1 for the meaning of the colored rectangles.

4.4.1.4 Effect of the aspect ratio

Figure 4.11 shows steady-state temperature and velocity fields when the aspect ratio $L/D =$ 0.5 and 2, Kn $= 0.1$, $\Delta T/T_0 = 2.0$, and $(\alpha_L, \alpha_R) = (0.5, 1.0)$. Figure 4.12 shows the domain average of the steady-state stream function is calculated for various Knudsen numbers with $L/D = 0.5$, 1, and 2. For comparison, the results for $L/D = 1$ in Fig. 4.6 are also shown. The center of the roll flow is closer to plate B for smaller aspect ratios. The Kn number where the peak of ψ_{ave} is obtained varies depending on the aspect ratio.

4.4.2 Case 2

4.4.2.1 One-way flows meander between array of rolls

The results for the case of non-uniformity of accommodation coefficients on both flat plates are shown here. The phase difference H breaks the symmetry of the domain. We investigate

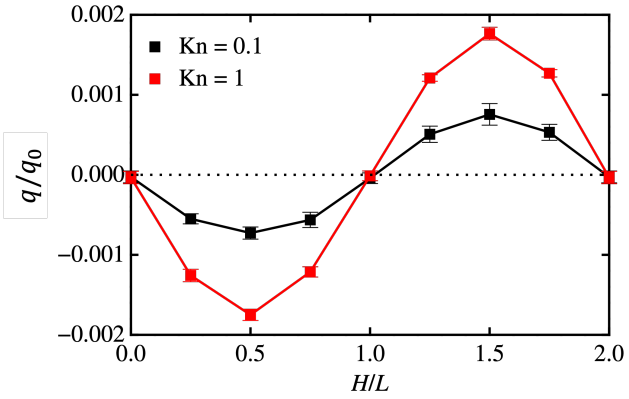

Figure 4.14: Non-dimensional mass flux q/q_0 vs the phase difference H/L. The case for Kn = 0.1 and 1.0, $\Delta T/T_0 = 2.0$, $(\alpha_L, \alpha_R) = (0.5, 1.0)$, and $L/D = 1.0$

the flow that occurs there. For Kn = 0.1, $\Delta T/T_0 = 2.0$, $(\alpha_L, \alpha_R) = (0.5, 1.0)$, and $L/D = 1.0$ [Fig. 4.1(b)], we analyze the flow by varying the phase difference H/L. Figure 4.13 shows the temperature distribution of the gas at steady-state with color-coding and black arrows as the velocity field and white lines as the streamlines for $H/L = 0.25n$ ($n = 0, 1, ..., 7$). In order to show the characteristics of the flow field intuitively and clearly, we present the flow field for two periods ($4L$). The streamlines are contours of the stream function [Eq. (4.1)] drawn at $\Delta\psi = 0.004$ intervals unless otherwise stated. For the phase difference $H/L = 0$ [Fig. 4.13(a)], circular vortices with diameters close to the plate spacing D are generated side by side. The present case differs from case 1 because the vortices are accelerated at the top and bottom. When the phase difference $H/L = 0.25$ [Fig. 4.13(b)], the vortices are slightly tilted. At this stage, the outermost streamline of the vortices meanders between vortices (red arrow in the figure). That is, a one-way flow is generated. As the phase difference increases further [Fig. 4.13(c)], the vortices are tilted further. The number of streamlines connecting the neighboring vortices also increases; this indicates the one-way flow is enhanced. The flow velocity vector at $H/L = 0.5$ shows that the one-way flow is in the $-X_1$ direction. When the phase difference $H/L = 0.75$ [Fig. 4.13(d)], multiple streamlines flowing between the tilted vortices can be observed but the flow speed of one-way flow decreases. When the phase difference $H/L = 1$ [Fig. 4.13(e)], the vortices become independent again, and the one-way flow disappears. Here, the interval between the streamlines is halved ($\Delta\psi = 0.002$) because of the small velocity. At this stage, the vortices form a roll pair distributed vertically that rotates in the opposite direction. At the phase difference $H/L = 1.25$ [Fig. 4.13(f)], the flow field is similar to $H/L = 0.75$ [Fig. 4.13(d)] inverted for the X_2 axis. When we invert and align the phase of Fig. 4.13(d) and Fig. 4.13(f), the flow fields are almost identical within the variability of the DSMC method. We can see that the streamlines also weave between the vortices, and at this time, the one-way flow is in the X_1 direction. $H/L = 1.5$ and 1.75 [Figs. 4.13(g) and (h)] also show the same flow field as the result of $H/L = 0.5$ and 0.25 inverted the X_2 axis, and a one-way flow in the X_1 direction is generated. At $H/L = 2.0$, the flow field is the same as the phase difference $H/L = 0$ [Fig. 4.13(a)].

We analyze the magnitude of the one-way flow. For this purpose, we calculate the steady-state mass flux q in the X_1 direction at each H/L. We calculate q/q_0 over ten dimensionless

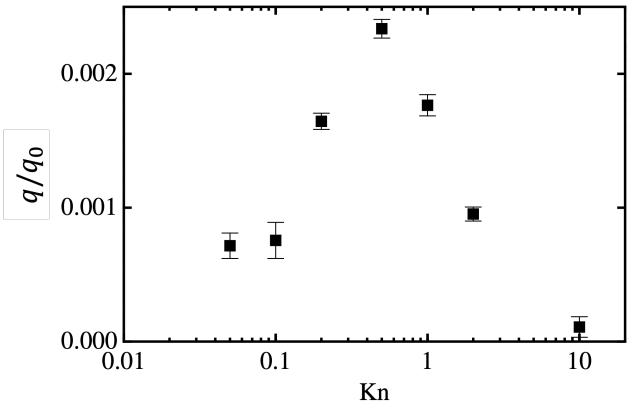

Figure 4.15: Non-dimensional mass flux q/q_0 vs the Knudsen number. The case for $H/L = 1.5$, $\Delta T/T_0 = 2.0$, $(\alpha_L, \alpha_R) = (0.5, 1.0)$, and $L/D = 1.0$.

times after the flow becomes steady and repeat the process ten times to average the data over 100 dimensionless times. Figure 4.14 shows the results. The error bars are the standard error σ multiplied by 3 for the time data. We can see that one-way flow occurs except for $H/L = 0,\ 1.0$, and 2.0. The flow variation is periodic for the phase difference H/L. q/q_0 is maximum in the X_1 negative direction at $H/L = 0.5$ and maximum in the X_1 positive direction at $H/L = 1.5$.

For $H/L = 1.5$, $\Delta T/T_0 = 2.0$, $(\alpha_L, \alpha_R) = (0.5, 1.0)$, and $L/D = 1.0$, the mass flux q is analyzed by varying Knudsen numbers. Here, we take the same approach as in Eqs. (2.20) and (2.21), where $(a_0, b_0) = (10000, 10)$. Figure 4.15 shows the results. When the symmetry of the domain is broken by the phase difference H, we see that one-way flow is indeed occurring. In the case of phase difference $H/L = 1.5$, the flow peak occurs around Kn ~ 0.5. The decay tendency is unclear for the lower Kn sides than the peak Kn. It cannot be determined whether one-way flow disappears in the limit of Kn $\to 0$.

Figure 4.16 shows the temperature distribution of the gas with color-coding, black arrows for the velocity field, and white lines for the streamlines at steady-state for Kn $= 0.5$ and 1.0. The width is shown as two periods ($4L$) similarly Fig. 4.14. The streamlines are the contour of the stream function [Eq. (4.1)]. The contour interval is 0.004. The parameters of Fig. 4.16 are the same as those of Fig. 4.14(f), except for the Knudsen number. Compared to Fig. 4.14(f), Fig. 4.16(a) has a stronger one-way flow as Kn increases. However, comparing Figs. 4.16(a) and 4.16(b), the one-way flow decreases as Knudsen number increases further.

4.4.2.2 Effect of the temperature difference between flat plates

For $H/L = 1.5$, Kn $= 0.1$ and 1.0, $(\alpha_L, \alpha_R) = (0.5, 1.0)$, and $L/D = 1.0$, the flow is analyzed by varying the non-dimensional temperature difference $\Delta T/T_0$. Figure 4.17 shows the profiles of the non-dimensional mass flux q/q_0 in the X_1 direction vs. $\Delta T/T_0$ at the steady-state. q/q_0 appears to change approximately linearly with $\Delta T/T_0$. The direction of the flow reversed when the temperature of plate B became lower than that of plate A. The one-way flow does not occur when the temperature difference vanishes.

The effect of the temperature variation in each flat plate is also analyzed. The part of

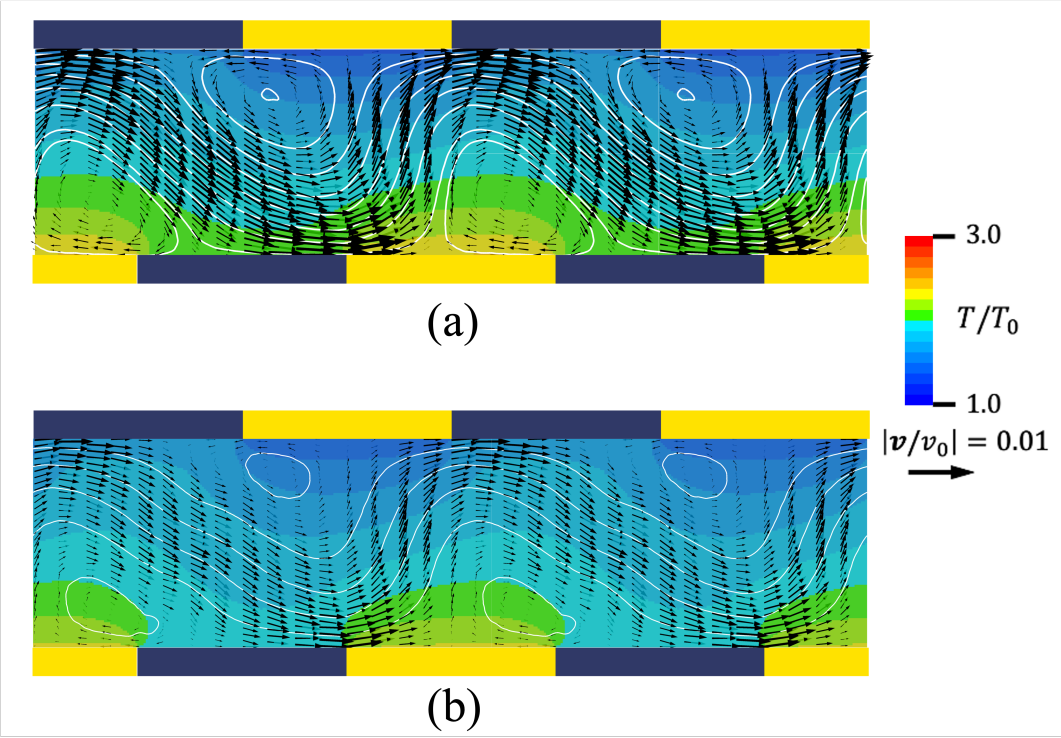

Figure 4.16: Temperature and velocity fields at steady-state for (a) Kn = 0.5 and (b) Kn = 1.0. The case for $H/L = 1.5$, $\Delta T/T_0 = 2.0$, $(\alpha_L, \alpha_R) = (0.5, 1.0)$, and $L/D = 1.0$.

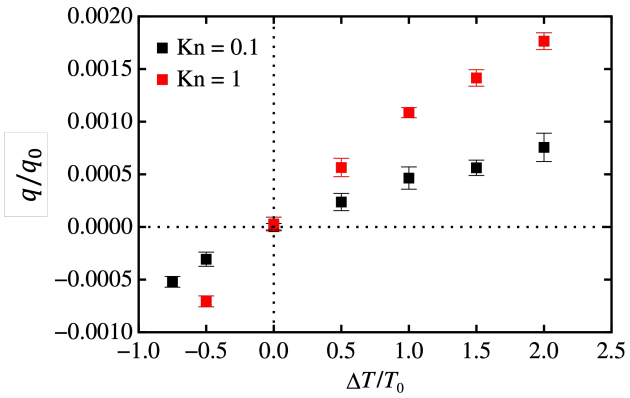

Figure 4.17: Non-dimensional mass flux q/q_0 vs $\Delta T/T_0$. $H/L = 1.5$, Kn = 0.1 and 1.0, $(\alpha_L, \alpha_R) = (0.5, 1.0)$, and $L/D = 1.0$.

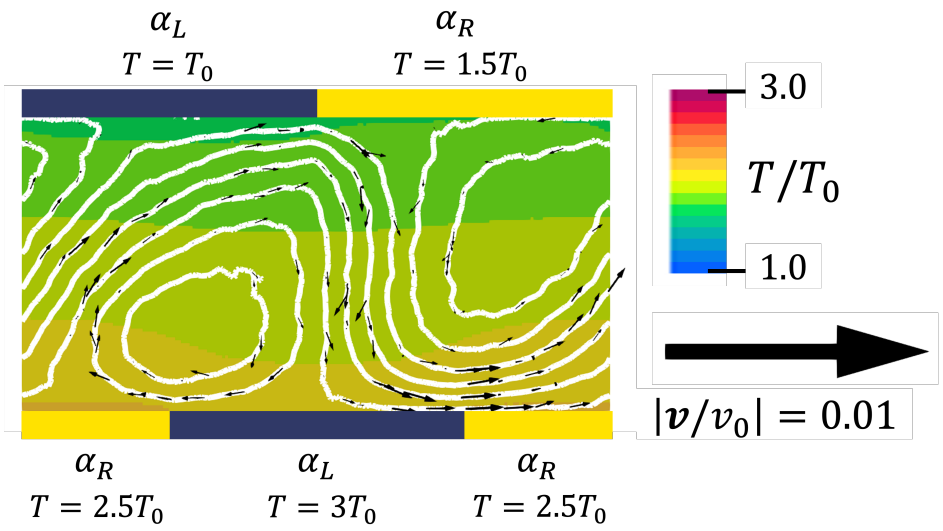

Figure 4.18: Temperature and velocity fields at steady-state for Kn = 1.0. $H/L = 1.5$, $(\alpha_L, \alpha_R) = (0.5, 1.0)$, and $L/D = 1.0$. Here, there is a temperature difference of $0.5T_0$ between the high and low accommodation coefficients area.

high accommodation coefficients on the cold plate receives more heat from the gas, while that on the heated plate emits more heat into the gas. Therefore, one may expect that the plate's temperature may be affected by its accommodation coefficient. On the heated plate, the temperature in the portion with high accommodation coefficients may become smaller than in the low accommodation coefficients. Inversely, the cold plate may have a larger temperature on the high accommodation coefficient part. Numerical analysis shows that even if such a temperature change occurs on the plates, the one-way flow will still occur. As an extreme case, numerical calculations were performed for a temperature difference of $0.5T_0$ in a flat plate with Kn = 1 and phase difference $H/L = 1.5$. The temperature field, streamlines, and velocity vectors of the gas at a steady state are shown in Fig. 4.18. Although the flow rate is decreasing, a meandering unidirectional flow is generated, and the flow direction remains unchanged.

4.4.2.3 Effect of the accommodation coefficient difference

For $H/L = 1.5$, Kn = 0.1 and 1.0, $\Delta T/T_0 = 2.0$, and $L/D = 1.0$, the flow is analyzed by varying accommodation coefficients (α_L, α_R) for the plate A and B. In the present case, $\alpha_R = 1.0$ is fixed and $\alpha_L = \alpha_R - \Delta\alpha$. The steady-state dimensionless mass flux obtained for Kn = 0.1 and 1.0 is plotted in Fig. 4.19. It can be seen that the flow rate varies nonlinearly, close to the second order (blue line in the figure), regarding the accommodation coefficient difference $\Delta\alpha$.

4.4.3 Comparison with Ratchet pump

Here we compare the flow found in this chapter with the results of previous studies that have the idea of inducing flow by keeping the wall surface at a uniform temperature; the

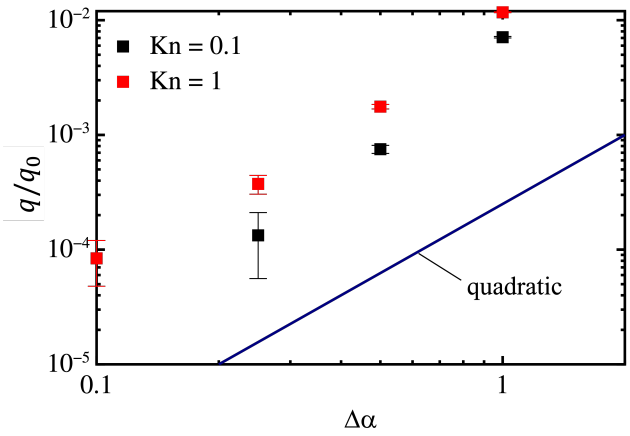

Figure 4.19: The double-logarithmic graph of q/q_0 vs $\Delta\alpha$. $H/L = 1.5$, Kn $= 0.1$ and 1.0, $\Delta T/T_0 = 2.0$, and $L/D = 1.0$. The blue line is an indicator of quadratic change.

ratchet pump [65, 82, 83], already introduced in Sec. 1.2.3. Ratchet pump uses a plate with a zigzag surface structure synchronous to accommodation coefficient distribution. Ratchet pumps have attracted much attention in recent years. In particular, Shahabi et al. analyzed various zigzag geometries combining diffuse and specular reflections and reported the flow rates obtained [65]. These results correspond to the results for $\Delta\alpha = 1.0$. Shahabi et al. performed their analysis for various zigzag geometries, but the maximum flow rates reported are a few times higher than those of our simple flat plates cases. In addition, since it is difficult with current processing technology to realize microchannels with a zigzag structure, our simple flat plates case has an advantage in terms of fabrication feasibility, as it can induce one-way flow simply by facing the planes.

4.5 Concluding remarks

In this chapter, we consider a simple channel structure consisting of two flat parallel plates with different constant temperatures. Through numerical analysis, we discover a new rarefied gas flow induced by non-uniformity of accommodation coefficient. When the geometry of system is symmetry, such as in Case 1, one-way flow is not induced. However, a one-way flow is induced only by the symmetry breaking of the distribution of accommodation coefficients due to the phase difference H, such as in Case 2.

In the present study, we use the Maxwell boundary condition is employed. It is interesting whether one-way flow is induced under other boundary conditions, such as Borman and Krylov boundary condition [84]. This remains as a future subject. The results of this study do not immediately lead to the realization of a MEMS pump; there are issues that need to be resolved before realization. For example, if there are edges at the channel entrance/exit, thermal edge flow, which is several orders of magnitude larger than the flow, will be generated there. To suppress or utilize the thermal edge flow, it is necessary to consider the design of the channel inlet/outlet.

Acknowledgements

First and foremost, I would like to express my deep respect and gratitude to my supervisor, Dr. Hiroshi Sugimoto. He has always been very sincere about my research and has provided me with meaningful ideas and guidance. Because of his serious but entertaining research attitude, I have been able to pursue my research path and enjoy my doctoral program. My doctoral course started with the Corona disaster, but I was helped right up to the end by the depth of knowledge and energy of my supervisor, who is very knowledgeable about communication technology and was the first to set up a remote work system. Once again, thank you very much. I will continue to cherish what he has given me and enjoy my journey. At the same time, I also owe a great debt of gratitude to Dr. Taku Ohwada. During my time in his lab, I heard him talk about various philosophical ideas. This is very stimulating for me to think about how I should be as a researcher. In addition, we had many meaningful discussions, including about doing my doctoral research. I would also like to express my gratitude to Dr. Shigeru Takata. He gave me much helpful advice for my research.

I also feel great appreciation for the members of the Fluid Dynamics Laboratory at Kyoto University. The casual conversations we had in daily life colored my life and made me feel optimistic. I wish you all the best in your future lives.

I would also like to thank my family for their continuous support throughout my life: my grandparents, Sadao and Hideko Sugimoto, Masaru and Nobuko Senda; my parents, Michitoshi and Mayumi Sugimoto; and my sister, Yuki Ito. Without their support, my journey would not have been as rich as it has been. Thank you very much.

I also want to thank the many friends who have accompanied me daily, my hobbies, and my fun. The time to relax and unwind was essential for me.

Finally, I would also like to thank my cats, Mi and Ki, and my dog, Hiragi, for their support and help in concluding the dissertation.

Bibliography

[1] Reynolds, O., "On certain dimensional properties of matter in the gaseous state. Part I. Experimental researches on thermal transpiration of gases through porous plates and on the laws of transpiration and impulsion, including an experimental proof that gas is not a continuous plenum," *Phil. Trans. R. Soc. Lond.*, Vol. 170, 1879, pp. 727–845.

[2] Knudsen, M., "Eine Revision der Gleichgewichtsbedingung der Gase. Thermische Molekularströmung," *Annalen der Physik*, Vol. 336, No. 1, 1909, pp. 205–229.

[3] Vargo, S. E. and Muntz, E. P., "An evaluation of a multiple-stage micromechanical Knudsen compressor and vacuum pump," *Rarefied Gas Dynamics*, edited by C. Shen, Peking University Press, Beijing, 1997, pp. 995–1000.

[4] Vargo, S. E., Muntz, E. P., and Shiflett, G. R., "Knudsen compresor as a micro- and macroscale vacuum pump without moving parts or fluids," *J. Vac. Sci. Tech. A*, Vol. 17, No. 4, 1999, pp. 2308–2313.

[5] Sone, Y., Waniguchi, Y., and Aoki, K., "One-way flow of a rarefied gas induced in a channel with a periodic temperature distribution," *Physics of Fluids*, Vol. 8, No. 8, 1996, pp. 2227–2235.

[6] Aoki, K., Sone, Y., Takata, S., Takahashi, K., and Bird, G. A., "One-way flow of a rarefied gas induced in a circular pipe with a periodic temperature distribution," *AIP Conference Proceedings*, Vol. 585, No. 1, 2001, pp. 940–947.

[7] Aoki, K., Degond, P., Mieussens, L., Takata, S., and Yoshida, H., "A Diffusion Model for Rarefied Flows in Curved Channels," *Multiscale Modeling & Simulation*, Vol. 6, No. 4, 2008, pp. 1281–1316.

[8] Aoki, K., Degond, P., and Mieussens, L., "Numerical Simulations of Rarefied Gases in Curved Channels: Thermal Creep, Circulating Flow, and Pumping Effect," *Communications in Computational Physics*, Vol. 6, No. 5, 2009, pp. 919–954.

[9] Bond, D., Wheatley, V., and Goldsworthy, M., "Numerical investigation of curved channel Knudsen pump performance," *International Journal of Heat and Mass Transfer*, Vol. 76, 2014, pp. 1 – 15.

[10] Bond, D., Wheatley, V., and Goldsworthy, M., "Numerical investigation into the performance of alternative Knudsen pump designs," *International Journal of Heat and Mass Transfer*, Vol. 93, 2016, pp. 1038 – 1058.

[11] Han, Y. L. and Muntz, E. P., "Experimental investigation of micro-mesoscale Knudsen compressor performance at low pressures," *J. Vac. Sci. Tech. B*, Vol. 25, 2007, pp. 703–714.

[12] Leontidis, V., Chen, J., Baldas, L., and Colin, S., "Numerical design of a Knudsen pump with curved channels operating in the slip flow regime," *Heat and Mass Transfer*, Vol. 50, No. 8, 2014, pp. 1065–1080.

[13] Sheng, Q., Tang, G.-H., Gu, X.-J., Emerson, D. R., and Zhang, Y.-H., "Simulation of thermal transpiration flow using a high-order moment method," *International Journal of Modern Physics C*, Vol. 25, No. 11, 2014, pp. 1450061.

[14] Tatsios, G., Lopez Quesada, G., Rojas-Cardenas, M., Baldas, L., Colin, S., and Valougeorgis, D., "Computational investigation and parametrization of the pumping effect in temperature-driven flows through long tapered channels," *Microfluidics and Nanofluidics*, Vol. 21, No. 5, 2017, pp. 99.

[15] López Quesada, G., Tatsios, G., Valougeorgis, D., Rojas-Cárdenas, M., Baldas, L., Barrot, C., and Colin, S., "Design Guidelines for Thermally Driven Micropumps of Different Architectures Based on Target Applications via Kinetic Modeling and Simulations," *Micromachines*, Vol. 10, No. 4, April 2019, pp. 249.

[16] López Quesada, G., Tatsios, G., Valougeorgis, D., Rojas-Cárdenas, M., Baldas, L., Barrot, C., and Colin, S., "Thermally driven pumps and diodes in multistage assemblies consisting of microchannels with converging, diverging and uniform rectangular cross sections," *Microfluidics and Nanofluidics*, Vol. 24, No. 7, 2020, pp. 54.

[17] Aoki, K., Degond, P., Takata, S., and Yoshida, H., "Diffusion models for Knudsen compressors," *Physics of Fluids*, Vol. 19, No. 11, 2007, pp. 117103.

[18] Takata, S., Sugimoto, H., and Kosuge, S., "Gas separation by means of the Knudsen compressor," *Eur. J. Mech. B/Fluids*, Vol. 26, 2007, pp. 155–181.

[19] Vargo, S. E. and Muntz, E. P., "Initial results from the first MEMS fabricated thermal transpiration-driven vacuum pump," *AIP Conference Proceedings*, Vol. 585, No. 1, 2001, pp. 502–509.

[20] Young, M., Han, Y.-L., Muntz, E. P., Shiflett, G., Ketsdever, A., and Green, A., "Thermal transpiration in microsphere membranes," *Rarefied Gas Dynamics*, edited by E. P. Muntz, Vol. 663 of *AIP Conf. Proc.*, AIP, AIP, 2003, pp. 743–751.

[21] Sone, Y. and Sato, K., "Demonstration of a one-way flow of a rarefied gas induced through a pipe without average pressure and temperature gradients," *Phys. Fluids*, Vol. 12, No. 7, 2000, pp. 1864–1868.

[22] Sone, Y., Fukuda, T., Hokazono, T., and Sugimoto, H., "Experiment on a one-way flow of a rarefied gas through a straight circular pipe without average temperature and pressure gradients," *Rarefied Gas Dynamics*, edited by T. J. Bartel and M. A. Gallis, Vol. 585, AIAA Conf. Proc., AIAA, 2001, pp. 948–955.

[23] Sone, Y. and Sugimoto, H., "Vacuum pump without a moving part and its performance," *Rarefied Gas Dynamics*, edited by A. D. Ketsdever and E. P. Muntz, Vol. 663 of *AIP Conf. Proc.*, AIP, 2003, pp. 1041–1048.

[24] An, S., Gupta, N. K., and Gianchandani, Y. B., "A Si-micromachined 162-stage two-part Knudsen pump for on-chip vacuum," *J. Microelectromech. Syst.*, Vol. 23, No. 2, 2014, pp. 406–416.

[25] Yamarthy, C., Pharas, K., Schultz, A., and McNamara, S., "Pneumatic pumping of liquids using thermal transpiration for lab-on-chip applications," *Sensors, 2009 IEEE*, edited by P. French, Vol. 1, IEEE, 2009, pp. 1931–1934.

[26] Gupta, N. K., An, S., and Gianchandani, Y. B., "A Si-micromachined 48-stage Knudsen pump for on-chip vacuum," *J. Micromech. Microeng.*, Vol. 22, 2012, pp. 105026.

[27] Gupta, N. K. and Gianchandani, Y. B., "Thermal transpiration in zeolites: A mechanism for motionless gas pumps," *Applied Physics Letters*, Vol. 93, No. 19, 2008, pp. 193511.

[28] Pharas, K. and McNamara, S., "Knudsen pump driven by a thermoelectric material," *Journal of Micromechanics and Microengineering*, Vol. 20, No. 12, nov 2010, pp. 125032.

[29] Gupta, N. K. and Gianchandani, Y. B., "Thermal transpiration in mixed cellulose ester membranes: Enabling miniature, motionless gas pum," *Microporous Mesoporous Mater.*, Vol. 142, No. 2–3, 2011, pp. 535–541.

[30] Gupta, N. K. and Gianchandani, Y. B., "Porous ceramics for multistage Knudsen micropumps—modeling approach and experimental evaluation," *Journal of Micromechanics and Microengineering*, Vol. 21, No. 9, aug 2011, pp. 095029.

[31] Liu, J., Gupta, N. K., Wise, K. D., and Gianchandani, Y. B., "Demonstration of motionless Knudsen pump based micro-gas chromatography featuring micro-fabricated columns and on-column detectors," *Lab Chip.*, Vol. 11, 2011, pp. 3487–3492.

[32] Qin, Y. and Gianchandani, Y. B., "iGC1: An integrated fluidic system for gas chromatography including Knudsen pump, preconcentrator, column, and detector microfabricated by a three-mask process," *J. Microelectromech. Syst.*, Vol. 23, No. 4, 2014, pp. 980–990.

[33] Faiz, A., McNamara, S., Bell, A. D., and Sumanasekera, G., "Nanoporous Bi2Te3thermoelectric based Knudsen gas pump," *Journal of Micromechanics and Microengineering*, Vol. 24, No. 3, feb 2014, pp. 035002.

[34] Qin, Y., An, S., and Gianchandani, Y. B., "Arrayed architectures for multi-stage Si-micromachined high-flow Knudsen Arrayed architectures for multi-stage Si-micromachined high-flow Knudsen pumps," *J. Micromech. Microeng.*, Vol. 25, No. 11, 2015, pp. 115026.

[35] Cheng, Q., Qin, Y., and Gianchandani, Y. B., "A bidirectional Knudsen pump with superior thermal management for micro-gas chromatography applications," *2017 IEEE 30th International Conference on Micro Electro Mechanical Systems (MEMS)*, 2017, pp. 167–170.

[36] Qu, C., Alphenaar, B., McNamara, S., and Walsh, K., "Fabrication of Nanoporous Membranes for Knudsen Pump Using Glancing Angle Deposition," *2020 IEEE 33rd International Conference on Micro Electro Mechanical Systems (MEMS)*, 2020, pp. 936–939.

[37] Zhao, S., Jiang, B., Maeder, T., Muralt, P., Kim, N., Matam, S. K., Jeong, E., Han, Y.-L., and Koebel, M. M., "Dimensional and Structural Control of Silica Aerogel Membranes for Miniaturized Motionless Gas Pumps," *ACS Applied Materials & Interfaces*, Vol. 7, No. 33, 08 2015, pp. 18803–18814.

[38] Toan, N. V., Inomata, N., Trung, N. H., and Ono, T., "Knudsen pump produced via silicon deep RIE, thermal oxidation, and anodic bonding processes for on-chip vacuum pumping," *Journal of Micromechanics and Microengineering*, Vol. 28, No. 5, feb 2018, pp. 055001.

[39] Nakaye, S., Sugimoto, H., Gupta, N. K., and Gianchandani, Y. B., "Thermally enhanced membrane gas sepration," *Eur. J. Mech. B/Fluids*, Vol. 49, No. 1, 2015, pp. 36–49.

[40] Nakaye, S. and Sugimoto, H., "Demonstration of a gas separator composed of Knudsen pumps," *Vacuum*, Vol. 125, 2016, pp. 154–164.

[41] Tamura, S., Sugimoto, H., and Yashima, M., "Desktop gas isotope separation by Knudsen pump," *AIP Conference Proceedings*, Vol. 2132, No. 1, 2019, pp. 190007.

[42] Kugimoto, K., Hirota, Y., and Kizaki, Y., "Motionless heat pump – A new application of thermal transpiration," *AIP Conference Proceedings*, Vol. 1786, No. 1, 2016, pp. 080004.

[43] Kugimoto, K., Hirota, Y., Kizaki, Y., Yamaguchi, H., and Niimi, T., "Performance prediction method for a multi-stage Knudsen pump," *Physics of Fluids*, Vol. 29, No. 12, 2017, pp. 122002.

[44] Kugimoto, K., Hirota, Y., Yamauchi, T., Yamaguchi, H., and Niimi, T., "Design and demonstration of Knudsen heat pump without moving parts free from electricity," *Applied Energy*, Vol. 250, 2019, pp. 1260 – 1269.

[45] Wang, K., Zeng, P., Ahn, J., and Ronney, P. D., "A self-sustaining thermal transpiration gas pump and SOFC power generation system," *Proceedings of the Combustion Institute*, Vol. 34, 2013, pp. 3327–3334.

[46] Zeng, P., Wang, K., Ahin, J., and Ronney, P. D., "Thermal transpiration based pumping and power generation devices," *J. Therm. Sci. and Tech.*, Vol. 8, No. 2, 2013, pp. 370–379.

[47] Wongwiwat, J., Bhuripanyo, P., Welles, T. S., DeBiase, V. P., Ahn, J., and Ronney, P. D., "Thermally self-sustaining tubular SOFC power generator with no moving parts," *Journal of Physics: Conference Series*, Vol. 1407, nov 2019, pp. 012007.

[48] Wang, X., Su, T., Zhang, W., Zhang, Z., and Zhang, S., "Knudsen pumps: a review," *Microsystems & Nanoengineering*, Vol. 6, No. 1, 2020, pp. 26.

[49] Sone, Y., *Molecular Gas Dynamics*, Birkhäuser, 2007.

[50] Loyalka, S. K., Petrellis, N., and Storvick, T. S., "Some exact numerical results for the BGK model: Couette, Poiseuille and thermal creep flow between parallel plates," *Zeitschrift für angewandte Mathematik und Physik ZAMP*, Vol. 30, No. 3, 1979, pp. 514–521.

[51] Sharipov, F., "Rarefied gas flow through a long tube at any temperature ratio," *Journal of Vacuum Science & Technology A*, Vol. 14, No. 4, 1996, pp. 2627–2635.

[52] Sharipov, F., "Application of the Cercignani–Lampis scattering kernel to calculations of rarefied gas flows. III. Poiseuille flow and thermal creep through a long tube," *European Journal of Mechanics - B/Fluids*, Vol. 22, No. 2, 2003, pp. 145–154.

[53] Ohwada, T., Sone, Y., and Aoki, K., "Numerical analysis of the Poiseuille and thermal transpiration flows between two parallel plates on the basis of the Boltzmann equation for hard-sphere molecules," *Physics of Fluids A: Fluid Dynamics*, Vol. 1, No. 12, 1989, pp. 2042–2049.

[54] Aoki, K., Sone, Y., and Masukawa, N., "A rarefied gas flow induced by a temperature field," *Rarefied Gas Dynamics*, 1995, pp. 35–41.

[55] Sone, Y. and Yoshimoto, M., "Demonstration of a rarefied gas flow induced near the edge of a uniformly heated plate," *Physics of Fluids*, Vol. 9, No. 11, 1997, pp. 3530–3534.

[56] Sone, Y., "Flows Induced by Temperature Fields in a Rarefied Gas and their Ghost Effect on the Behavior of a Gas in the Continuum Limit," *Annual Review of Fluid Mechanics*, Vol. 32, No. 1, 2000, pp. 779–811.

[57] Sugimoto, H. and Sone, Y., "Vacuum Pump without a Moving Part Driven by Thermal Edge Flow," *AIP Conference Proceedings*, Vol. 762, No. 1, 2005, pp. 168–173.

[58] Maxwell, J. C., "On Stresses in Rarified Gases Arising from Inequalities of Temperature," *Phil. Trans. R. Soc. Lond.*, Vol. 170, 1879.

[59] Wilk, S., "The Crookes' radiometer apply light pressure," *Optics and Photonics News*, Vol. 18, 09 2007, pp. 17–19.

[60] DENPOH, K., "Another Possible Origin of Temperature and Pressure Gradients across Vane in the Crookes Radiometer," *Journal of the Vacuum Society of Japan*, Vol. 60, No. 12, 2017, pp. 471–474.

[61] Edmonds, T. and Hobson, J. P., "A study of thermal transpiration using ultrahigh-vacuum techniques," *J. Vac. Sci. Tech.*, Vol. 2, 1965, pp. 182–197.

[62] Hobson, J. P., "Surface smoothness in thermal transpiration at very low pressures," *J. Vac. Sci. Tech.*, Vol. 6, No. 1, 1969, pp. 257.

[63] Hobson, J. P., "Accommodation pumping – A new principle for low pressures," *J. Vac. Sci. Tech.*, Vol. 7, 1970, pp. 351.

[64] Hobson, J. P. and Salzman, D. B., "Review of pumping by thermal molecular pressure," *Journal of Vacuum Science and TechnologyTechnology*, Vol. 18, 2000, pp. 1758.

[65] Shahabi, V., Baier, T., Roohi, E., and Hardt, S., "Thermally induced gas flows in ratchet channels with diffuse and specular boundaries," *Scientific Reports*, Vol. 7, No. 1, 2017, pp. 41412.

[66] Sugimoto, S. and Sugimoto, H., "Driving mechanism of thermal transpiration pump with porous material," *AIP Advances*, Vol. 10, No. 10, 2020, pp. 105007.

[67] Sugimoto, S. and Sugimoto, H., "Quantitative numerical analysis of micro-thermal transpiration pump using kinetic theory of gases," *Microfluidics and Nanofluidics*, Vol. 26, No. 2, 2022, pp. 12.

[68] Sugimoto, S. and Sugimoto, H., "Thermal transpiration flows induced by differences in accommodation coefficients," *Physics of Fluids*, Vol. 34, No. 4, 2022, pp. 042005.

[69] Bird, G., *Molecular gas dynamics and the direct simulation of gas flows*, No. 42 in The Oxford engineering science series, Clarendon Press,Oxford University Press, 1994.

[70] Koura, K., "Improved null-collision technique in the direct simulation Monte Carlo method: Application to vibrational relaxation of nitrogen," *Computers and Mathematics with Applications*, Vol. 35, No. 1, 1998, pp. 139 – 154.

[71] Wagner, W., "A convergence proof for Bird's direct simulation Monte Carlo method for the Boltzmann equation," *Journal of Statistical Physics*, Vol. 66, No. 3, 1992, pp. 1011–1044.

[72] Sharipov, F. and Seleznev, V., "Data on Internal Rarefied Gas Flows," *Journal of Physical and Chemical Reference Data*, Vol. 27, No. 3, 1998, pp. 657–706.

[73] Kosuge, S. and Takata, S., "Database for flows of binary gas mixtures through a plane microchannel," *Eur. J. Mech. B/Fluids*, Vol. 27, No. 4, 2008, pp. 444–465.

[74] Titarev, V. A. and Shakhov, E. M., "Poiseuille flow and thermal creep in a capillary tube on the basis of the kinetic R-model," *Fluid Dynamics*, Vol. 47, No. 5, 2012, pp. 661–672.

[75] HASEGAWA, M. and SONE, Y., "Poiseuille and Thermal Transpiration Flows of a Rarefied Gas for Various Pipes," *Vacuum*, Vol. 31, No. 5, 1988, pp. 416–419.

[76] An, S., Qin, Y., and Gianchandani, Y., "A Monolithic High-Flow Knudsen Pump Using Vertical Al2O3 Channels in SOI," *Journal of Microelectromechanical Systems*, Vol. 24, 2015, pp. 1606–1615.

[77] Sugimoto, H., Takata, S., and Kosuge, S., "Gas separation effect of the pump driven by the thermal edge flow," *Rarefied Gas Dynamics*, edited by M. S. Ivanov and A. K. Revrov, Russian Academy of Sciences, Nobosibirsk, 2007, pp. 1158–1163.

[78] Zhang, Z., Wang, X., Zhao, L., Zhang, S., and Zhao, F., "Study of Flow Characteristics of Gas Mixtures in a Rectangular Knudsen Pump," *Micromachines*, Vol. 10, No. 2, 2019.

[79] Baier, T. and Hardt, S., "Gas separation in a Knudsen pump inspired by a Crookes radiometer," *Microfluidics and Nanofluidics*, Vol. 24, No. 6, 2020, pp. 41.

[80] Lotfian, A. and Roohi, E., "Binary gas mixtures separation using microscale radiometric pumps," *International Communications in Heat and Mass Transfer*, Vol. 121, 2021, pp. 105061.

[81] Kadoya, K., Matsunaga, N., and Nagashima, A., "Viscosity and Thermal Conductivity of Dry Air in the Gaseous Phase," *Journal of Physical and Chemical Reference Data*, Vol. 14, No. 4, 1985, pp. 947–970.

[82] Chen, J., Stefanov, S., Baldas, L., and Colin, S., "Analysis of flow induced by temperature fields in ratchet-like microchannels by Direct Simulation Monte Carlo," *International Journal of Heat and Mass Transfer*, Vol. 99, 08 2016, pp. 672–680.

[83] Donkov, A. A., Tiwari, S., Liang, T., Hardt, S., Klar, A., and Ye, W., "Momentum and mass fluxes in a gas confined between periodically structured surfaces at different temperatures," *Phys. Rev. E*, Vol. 84, Jul 2011, pp. 016304.

[84] Borman, V. D., Krylov, S. Y., and Prosyanov, A. V., "Theory of nonequillibrium phenomena at a gas-solid interface," *Sov. Phys. JETP*, Vol. 67, No. 10, 1988, pp. 2110.